City Research Online

City St George's, University of London

Citation: Saini, D. (1988). Fibre optic pressure using the technique of frustrated total internal reflection. (Unpublished Doctoral thesis, City University)

This is the accepted version of the paper.

This version of the publication may differ from the final published version. To cite this item please consult the publisher's version.

Permanent repository link: https://openaccess.city.ac.uk/id/eprint/35199/

Copyright and Reuse: Copyright and Moral Rights remain with the author(s) and/or copyright holders. Copies of full items can be used for personal research or study, educational, or not-for-profit purposes without prior permission or charge, unless otherwise indicated, provided that the authors, title and full bibliographic details are credited, a hyperlink and/or URL is given for the original metadata page and the content is not changed in any way. For full details of reuse please refer to City Research Online policy.

City Research Online: http://openaccess.city.ac.uk/ publications@citystgeorges.ac.uk

Fibre Optic Pressure Sensing Using the Technique of Frustrated Total Internal Reflection

by

Devinder Pal Singh Saini B.Sc. M.Sc.

A thesis submitted for the degree of Doctor of Philosophy

School of Electrical Engineering and Applied Physics
City University, Northampton Square,
London. EC1 O HB

June, 1988

To my Mother and Father

and

a very special friend Beth

CONTENTS

List of figures 6

List of symbols 11

Acknowledgments 13

Declaration 14

Abstract 15

Chapter 1

Intorduction 16

Abstract 17

1.0 General Introduction 18

1.1 Principles of optical fibres 22

1.2 Fibre optic Sensors 27

.2.1 Intensity sensors 27

1.3 Intrinsic Sensors 29

.3.1 "Fibredyne" sensors 29

.3.2 Microbending Fibre Optic Sensors 30

1.4 Extrinsic Sensors 33

.4.1 Reflection Modulation Sensors 33

.4.2 Transmission Modulation Sensors 37

.4.3 Spectral Sensors 40

.4.4 Light Scattering Sensors 40

.4.5 Evanescent or Coupled Waveguide Sensors 42

.4.6 Frustrated-Total-Internal-Reflection Sensors 45

.4.7 Near-Total-Internal-Reflection Sensors 46

1.5 Conclusions 47

1.6 Aims of this work 48

Chapter 2

Frustrated total internal reflection 50

Abstract 51

2.1 Introduction 52

2.2 Waves at an Interface 52

2.3 Total Internal Reflection 54

2.4 Frustrated Total Internal Reflection (Evanescent Wave Coupling) 57

Chapter 3

Analogue Pressure Transducer 61

Abstract 62

3.1 Introduction 63

3.2 Design of the sensor in this work 67

3.3 Charateristics of the Pressure Sensor 74

3.4 Referencing of the output modulated signal with the input 78

3.5 Range and Sensitivity of the Pressure Sensor 80

3.6 Thermal Effects 82

3.7 Discussion 84

Chapter 4

Hybrid (Optical-Electrical) Digital

Force (pressure) Transducer 87

Abstract 88

4.1 Introduction 89
4.2 The Quartz Resonator 90
.2.1 Crystal Resonator Structure and Mounting 96
.2.2 Fabrication of Quartz Resonator 98
.2.2.1 Photolithographic Fabrication of Masks 102
4.3 Transducer Design 107
4.3.1 Optical Detection of Resonant Frequency 108
.3.2 The Electronic System 110
4.4 Results 112
.4.1 Thermal Effects 117
4.5 Power Requirements 120
4.6 Discussion 121

Chapter 5

Photothermally Driven Quartz Sensor 123
Abstract 124
5.1 Intoduction 125
5.2 Photothermal Effect 126
5.2.1 Optical Drive 129
5.3 Experimental Setup 133
5.4 Results 137
5.5 Conclusions and Future Work 141

Chapter 6

Summary 143

Appendix A 148

Appendix B 169

Appendix C 173

Appendix D 188

References 190

LIST OF FIGURE CAPTIONS

Figure 1.1 Shows a ray of light trapped within in two glass air interfaces due to total internal reflection.

Figure 1.2 Shows rays of light travelling within a cylindrical glass rod in a helical manner.

Figure 1.3 Typical optical fibre construction the core being protected by the cladding.

Figure 1.4 Shows the acceptance angle of the fibre.

Figure 1.5 Shows the optical absorption curves for glass.

Figure 1.6 Shows the classes of intensity sensors.

Figure 1.7 An optical fibre flowmeter based on "fibredyne" intensity modulation.

Figure 1.8 Microbending loss in an optical fibre (a) experimental apparatus (b) response curve.

Figure 1.9 Microbending fibre optic sensor.

Figure 1.10 Liquid level sensor.

Figure 1.11 Fibre optic displacement sensor.

Figure 1.12 Reflective displacement sensor and an acoustic diaphragm.

Figure 1.13 Operation of interuption-type sensor.

Figure 1.14 Photoelastic fibre optic intensity sensor.

Figure 1.15 Fibre optic flow velocity sensor.

Figure 1.16 Evanescent or coupled waveguide sensor.

Figure 1.17 Frustrated total internal reflection mode sensor.

Figure 1.18 Near total internal reflection sensor.

Figure 2.1 Reflection and refraction at a boundary between two media with refractive indices n_1 and n_2.

Figure 2.2 Schmeatic of total internal reflection ($n_i > n_t$).

Figure 2.3 Schmeatic of two layers of dense media seperated by a less dense medium of thickness d.

Figure 2.4 Shows the theoretical transmisson across an air gap between two dielectric media.

Figure 3.1 Schematic of two critically cut fibres.

Figure 3.2 Schematic of hydrophone developed by Spillman and McMahon.

Figure 3.3 The experimental characteristics of the FTIR hydrophone.

Figure 3.4 Schematic of pressure sensor developed by Beasley.

Figure 3.5 Schematic of analouge pressure transducer.

Figure 3.6 Schematic of evanescent wave coupling.

Figure 3.7 Transmission of light at 632.8 nm across a gap as a function of width for different angles of fibre cut.

Figure3.8 Characteristic response of the device at $\lambda = 632.8$nm and $\theta = 55^0$.

Figure 3.9 Shows the calculated in comparison with experimental response of the device (solid line calculated response, dashed line measured response).

Figure 3.10 Showing sensor with a reference fibre attached.

Figure 3.11 Showing the reference output of the sensor.

Figure 3.12 Calculated response of the sensor (A). $\lambda = 850$nm, (B) $\lambda = 1.15$nm $\theta = 55^o$.

Figure 3.13 Characteristic response of the sensor over a range of

temperatures.

Figure 4.1 Showing an AT cut in quartz crystal.

Figure 4.2 Distortion of quartz due to an electric field.

Figure 4.3 Rectangular bar clamped at both ends.

Figure 4.4 Showing a quartz tuning fork structure as used by Litton Systems Inc.

Figure 4.5 The Marconi double tuning fork.

Figure 4.6 Schmatic of a Laue camera.

Figure 4.7 X-ray spectrum used.

Figure 4.8 Schematic of Laue photographs obtained for quartz (a) x-axis (b) y-axis (c) z-axis.

Figure 4.9 Elements of the symmetry class 32m.

Figure 4.10 Schematic of crystals produced using the air abration technique.

Figure 4.11 Photolithographic mask used to produce copper masks for etching.

Figure 4.12 Schematic mask alignment showing bottom mask and spacer, another mask is placed on top and aligned using a light table.

Figure 4.13 Schematic of air abration equipment used.

Figure 4.14 Shows electrode pattern used to drive the crystal.

Figure 4.15 Schematic of transducer design.

Figure 4.16 Showing crystal mounted on cantilever beam with thin film spacer. (not to scale).

Figure 4.17 Schematic of circuit and detection system used.

Figure 4.18 Fundamental frequency of the resonance of quartz crystal

observed on a spectrum analyzer.

Figure 4.19 Calibration graph of resonant frequency of the crystal as a function of pressure measured as weight applied to beam.

Figure 4.20 Theoretical calibration curve of the sensor.

Figure 4.21 Percentage change in resonant frequency of crystal for 5-min cycles of weight applied and weight removed from beam.

Figure 4.22 Change in resonant frequency of crystal with change in ambient temperature over two time periods.

Figure 4.23 Schematic of twin beams for possible tempeature compensation system.

Figure 5.1 Model of photothermal exitation system.

Figure 5.2 Absorption curve of nichrome.

Figure 5.3 Temperature distribution as predicted by Kirman et al [50].

Figure 5.4 Model of flexed quartz beam.

Figure 5.5 Relative composition of nichrome.

Figure 5.6 Quartz crystal with electrode.

Figure 5.7 Schematic of experimental setup.

Figure 5.8 Experimental arrangement for optical drive.

Figure 5.9 Photograph of resonance peak obtained.

Figure 5.10 Photograph of the change in resonance amplitude with changing drive power.

Figure 5.11 Evanescent wave detection system.

Figure A.1 Shows E-M waves at an interface between two dielectric media.

Figure A.2 An incoming wave whose E-field is normal to the plane of incidence.

Figure A.3 An incoming wave whose E-field is in the plane of

incidence.

Figure A.4 Schmeatic of total internal reflection ($n_i > n_t$).

Figure A.5 Propagation of vectors for internal reflection.

Figure A.6 Schmeatic of two layers of dense media seperated by a less dense medium of thickness d.

Figure C.1 Shows the electro mechanical coupling in quartz.

List of symbols

A	deflection
c	heat capacity
C_d	rate of change with pressure of core seperation
C_L	rate of change with pressure of interaction length
C_r	rate of change with pressure of core radius
C_{n1}	rate of change with pressure of core index
C_{n2}	rate of change with pressure of medium index
D_o	ratio of core seperation to core radius
d	seperation
E	Young's modulus
$\mathbf{E}_t$	electric field vector of transmitted wave
E_{ot}	transmitted wave amplitude
f_o	resonant frequency
f_o'	new frequncy of resonance
Δf	bandwidth of resonant frequency at 3db points
F	force
g	thickness of beam
h	Planck's constant
l_q	thickness of quartz
l_n	thickness of nichrome
k_t	transmitted wave vector
k	thermal conductivity
L	Interaction length
l	Beatlength

ℓ	length between clamping points
n	refractive index
Q	Modulation index
Q	quality factor
r	core radius
T	intensity transmitted into third medium
t	thickness of bar
t'	breadth of beam
V & W	Parmeters dependent upon the model propertise of the fibre
α	component of transmitted wave vector in the y direction
α_q	thermal diffusivity of quartz
α_n	thermal diffusivity of nichrome
β	optical absorption of nichrome
γ	strain
λ	wavelength of light
θ_a	half angle of cone of incidence to fibre
θ_i	angle of incedence
θ_t	angle of transmission
θ_c	angle of refraction
Φ	ambient temperature
ϕ	complex temperature
ρ	density
σ	tensile stress
ω	angular frequency of wave

Acknowledgements

I would like to take this opportunity express my sincere thanks to Dr. A.W. Palmer and Dr. K.T.V. Grattan for their kind help and guidance throughout this project.

I would also like to thank the S.E.R.C. for funding my post of research assistant at the university, Dr M. Collier of Marconi for the supply of quartz crystals and useful discussions, along with the Optical Sensors Collaborative Association (OSCA) for partially funding this project.

Thanks are also due to Dr A. Augousti, Mr R Valsler and the technical staff of the City University for their useful contributions.

Declaration

I grant the powers of discretion to the University Librarian to allow this thesis to be copied in whole or in part without further reference to me. This permission covers only single copies made for study purposes, subject to normal conditions of acknowledgement.

ABSTRACT

A number of pressure sensing devices were constructed using the principle of frustrated total internal reflection (FTIR), where light is coupled between a critically cut fibre and a second optical element across an air gap through the evanescent wave created at the critically cut end of an optical fibre.

Initially a simple analogue device was designed and constructed. The characteristics of the sensor were obtained and compared with the predictions of a simple theoretical model. This showed that the use of the FTIR effect for detecting pressure was indeed valid, although certain problems did arise due to thermal effects. These being due to the thermal mismatch between the optical elements and the metallic body of the sensor.

A second sensor based on the FTIR effect was then designed and constructed in order to eliminate the thermal instabilities encountered in the analogue sensor. This sensor was digital in nature, where a quartz crystal cut into a double tuning fork structure, mounted upon a cantilever beam, was driven into resonance via the photovoltaic effect. This being a hybrid device, the power to drive the crystal was delivered via an optical fibre to a photo diode mounted at the sensor head. The voltage generated by the diode was amplified by a small transformer which drove the crystal electrically into resonance. The resonance frequency was optically detected via the FTIR effect. The change in the resonance frequency as function of applied pressure was measured, and graphs for its thermal response and long term stability were obtained.

An optical drive system using the photothermal effect to drive the quartz crystal into resonance was investigated. The results obtained were compared with a simple model. A sensor was constructed to use this effect to measure pressure, however, a number of problems were encountered in optically detecting the resonance frequency of the optically driven crystal. These are discussed in detail along with possible solutions.

Chapter 1

Introduction

Abstract

In this chapter a general introduction is made to the feild of fibre optic sensing, begining with a short over view of the principles of fibre of fibre optics, followed by a short reveiw of fibre optic sensors.

1.0 General Introduction

It is well known that optical techniques can provide nondestructive noncontact measurements of a great variety of physical parameters such as displacement, strain, film thickness, and temperature with high precision and resolution. Also monitoring the transmission path of an optical beam can provide information about the existence of objects and/or their chemical composition. With the advances in fabrication of low loss optical fibres and components for optical fibre communications a new range of highly versatile optical sensors based on fibre technology have been and are being developed.

Although the potential applications of optical fibres as sensors in addition to light transmission for communication purposes is relatively new, a considerable amount of research and development has been conducted during the past few years. These efforts have resulted in a wide variety of fibre optical sensor configurations [1- 5] which are able to receive information from remotely located monitoring centers. The parameters that have been monitored include pressure, acoustic waves, vibration, position, strain, liquid level, flow velocity, acceleration, rotation rate, temperature, electric current, magnetic fields, electromagnetic fields, and chemical processes.

There are many advantages in using optical fibre sensors over conventional sensors. These are listed below:

(a) Good electrical insulation

(b) Immunity to electromagnetic interference

(c) Safety from explosive environments

(d) Potentially High information capacity

(e) Low signal attenuation (thus long distance transmission is possible)

(f) Flexibility and lightness

(g) Free from crosstalk

(h) Low material cost

(i) Simple and integral referencing

(j) Rugged construction

(k) Chemically inert

One of the most important advantages is the elimination of electrical currents at the sensor head. As a result, optical fibre sensor systems provide extremely good electromagnetic interference immunity which is important for all such applications as factory automation, and operation in hazardous environments. These sensors can have fast response times and be miniaturized. Optical fibre sensors can be versatile and can be designed to sense many parameters. They can also be compatible with optical fibre transmission and multiplexing schemes.

Various modulation techniques have been used as sensing mechanisms these include; intensity, phase, frequency, wavelength, and polarization modulation. These techniques give rise to various different forms and types of sensors, they not only differ in construction but also in most other characteristics such as sensitivity, dynamic range, sensor signal transmission and sensor signal detection. Amongst those techniques

discussed, sensors can be categorized in two main ways namely, intensity sensors and phase sensors, and other techniques are becoming important.

Intensity modulation sensors are those sensors that depend for their operation upon a measureand to modulate the intensity of light within an optical fibre, the modulation can be imposed upon the light directly as it travels through the fibre, or it can be imposed upon it when it emerges from one fibre via an external mechanism and then channelled to a detector via the same fibre or a second fibre.

Phase sensors are those that rely upon a mesureand to modulate the phase of the light wave travelling within a fibre with the intensity of the light being unaffected. The most important difference between these categories of sensors lies in the phase and intensity responsivity of guided light in a typical optical fibre. Typical commercial optical fibres are highly effective optical phase modulators, the guided light in an optical fibre can be modulated in phase by environmental variations due to changes in fibre length and refractive index of the fibre, these variations may be large and random typically the phase variation may exceed 10^5 radians in a random manner. Therefore, the transmission of phase modulated signals for sensor purposes is difficult, if not prohibited through environmental noise. Conversely the transmission of intensity in typical optical fibres is stable as the environmental noise in optical intensity transmission is typically less than 1db per kilometer . Sensors which use phase type modulation techniques require special fibres which can be

expensive and ordinary photodiodes do not respond to phase variations in an optical waveform unless an optical reference is provided to establish optical interference. The stability of an optical interferometer depends on the spatial coherence of the optical wavefronts. Therefore fibre optic phase sensors are often constructed from lengths of single mode optical fibre. [6-10]

However, the reliable transmission of a known intensity modulated signals through commercial optical fibre poses no major problems if the fibre not subjected to excessive bending (see section 1.3.2). The fabrication of intensity sensors does require modification of the fibre in order to modulate the intensity. But intensity sensors are often made of multimode fibres with small sensors that can measure parameters at localized points. Therefore intensity sensors can be less complicated and hence easier to produce than any other type of sensor.

In order to gain a fuller understanding of fibre optic sensors, it is necessary to understand the principles of transporting radiation along optical fibres. Therefore for the purposes of this thesis, this chapter will be limited to a brief introduction to light propagation in a fibre followed by a brief review of the basic principles of fibre optic intensity sensors. An examination of the techniques used to implement these principles is presented.

1.1 Principles of optical fibres

If a glass slab is considered with two parallel glass-air interfaces, these interfaces will trap a ray approaching at a suitably shallow angle and transmit it (Fig. 1.1) virtually without loss by a series of total internal reflections.

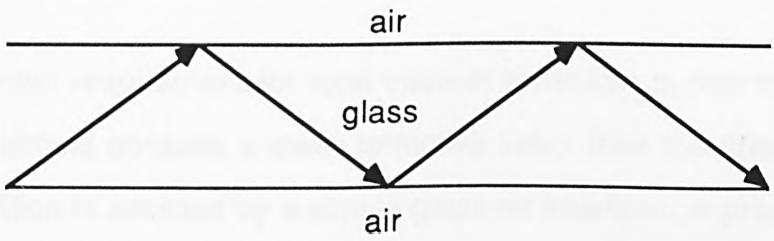

Fig 1.1 Shows a ray of light trapped within two parallel glass air interfaces due to total internal reflection

A cylindrical optical glass fibre, which can be many kilometres in length behaves in a similar manner except that the majority of rays travel in a stepped helical manner by many such reflections at the circumference (Fig. 1.2).

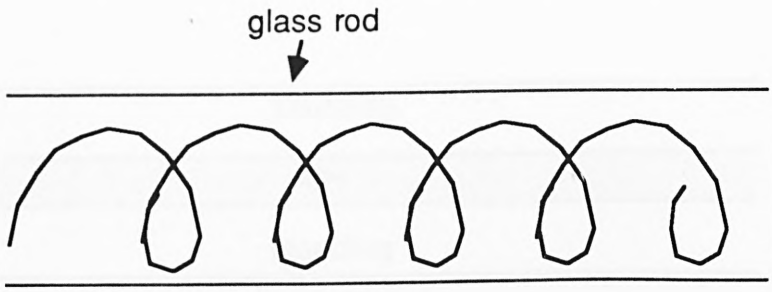

Fig 1.2 Shows rays of light travelling within a cylindrical glass rod in a helical manner

An essential requirement for total internal reflection is that the external medium should possess a lower refractive index than the fibre. Although this condition is satisfied by a simple glass-air interface, in practice this is easily damaged, and light then escapes by two principal mechanisms, both of which alter the effective angle of incidence at the interface:-

(a) inclusions or scratches

(b) surface contamination (e.g. grease)

Grease has a refractive index which is similar to that of glass and hence to the approaching ray appears as an extension of the glass surface.

These defects are avoided by the provision of an optical cladding (Fig.1.3). This is a region of lower refractive index surrounding the central zone (core). Total internal reflection can now take place at the protected cladding interface.

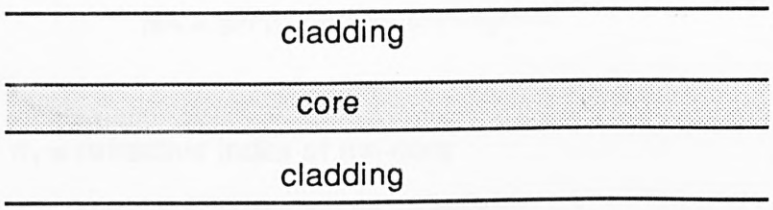

Fig 1.3 Typical optical fibre construction the core being protected by the cladding

Since only those rays with a sufficiently low grazing angle at the core-cladding interface are transmitted by total internal reflection, rays must approach the input surface of the fibre within a limited cone angle (Fig. 1.4). The half angle θ_a of this cone, within which rays will be transmitted, is called the acceptance angle and is related to the refractive indices of the three media - core, cladding and air. The refractive index of air is approximately unity.

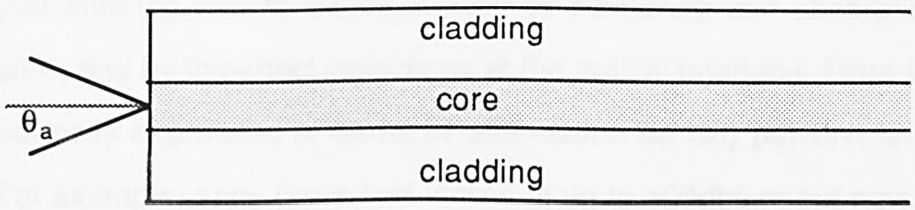

Fig 1.4 Show the acceptance angle of the fibre

The light collecting ability of the fibre is called the numerical aperture (NA)

and is given by

$$NA = \sin \theta_a = 1/n_3 (n_1^2 - n_2^2)^{1/2} \qquad (1.1)$$

where:

n_1 = refractive index of the core

n_2 = refractive index of the cladding

n_3 = refractive index of the surrounding medium

Rays entering at greater angles to the fibre axis than θ_a will not be transmitted by total internal reflection. Since many light sources emit over a wide range of angles, it follows that fibres with large values of NA will collect a greater proportion of this light. Similarly, large diameter fibres are to be preferred if the light source is large compared to the fibre. Typically fibres have diameters ranging from 30μm - 1000μm for 'multimode' transmission and lower diameters for monomode transmission and values of NA vary from 0.15 to 0.50.

The amount of light emerging from the end of a fibre is always less than that entering due to losses caused by scattering and absorption in the core, and by imperfect reflections at the optical interface. Fibre losses are normally expressed in terms of attenuation (in dB) per unit length (km). For example, early fibres had losses of up to 100db/km but now figures of 0.2dB/km are easily achievable [38].

All glasses scatter light due to "frozen-in" thermal fluctuations of constituent atoms. These cause density and hence refractive index

variations within the material. It is believed that this intrinsic Rayleigh scattering represents the fundamental minimum limit to fibre attenuation. Since Rayleigh scattering varies inversely as the fourth power of the wavelength (i.e.λ^{-4}) it follows that lower fibre attenuation occurs if longer wavelengths are used, and ideally light sources should be selected accordingly, consistent with adequate detector response. In practice other considerations often assume greater importance. For example, it is particularly important to avoid attenuation peaks which occur with some types of fibre. One particularly severe peak occurs close to the Gallium Arsenide source wavelength of λ = 1300nm. This is caused by absorption in the core by hydroxyl ions (OH^-) and is referred to as the water peak (Fig. 1.5).

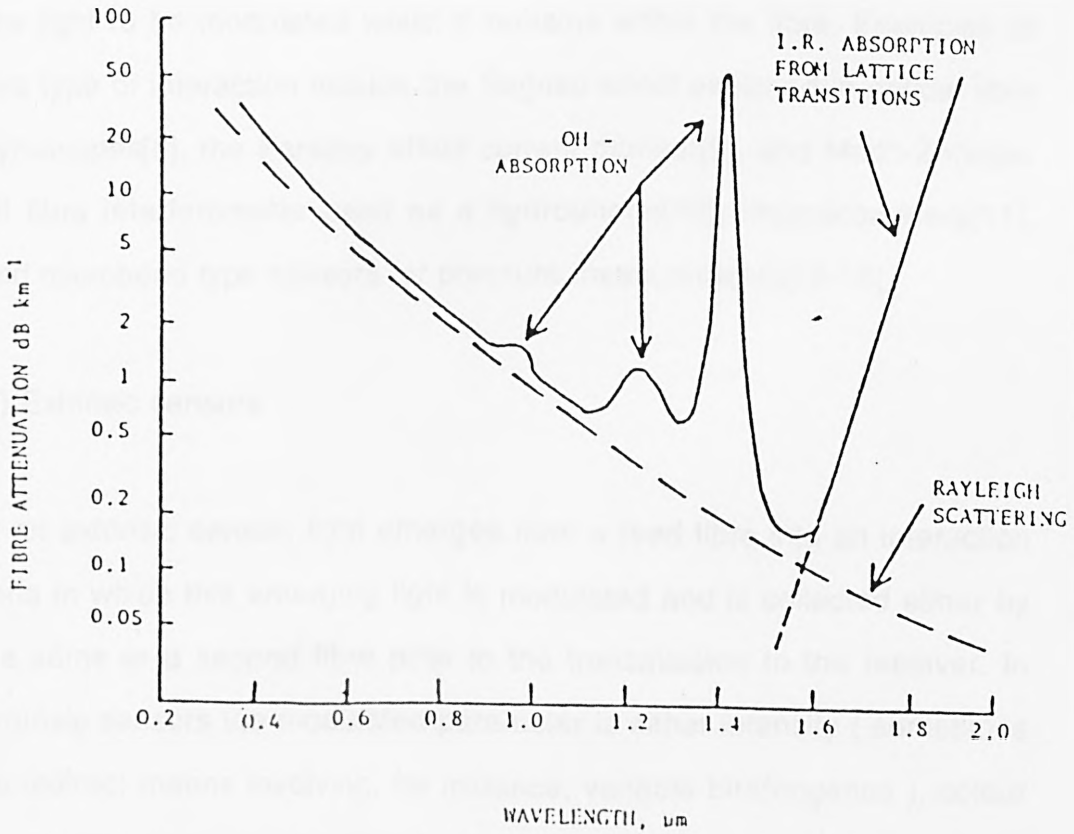

Fig 1.5 Shows the optical absorption curves for glass[38]

1.2 Fibre Optic Sensors

1.2.1 Intensity sensors

Fibre optic intensity sensors may be subdivided into two further categories, the nature of which depends upon whether the interaction takes place within the fibre or in a seperate optical transducer. These may be termed (i) Intrinsic sensors and (ii) Extrinsic sensors.

(i) Intrinsic sensors

With this type of sensor the environmental parameter of interest causes the light to be modulated whilst it remains within the fibre. Examples of this type of interaction include the Sagnac effect exploited in optical fibre gyroscopes[8], the Faraday effect current monitor[9], and Mach-Zehnder all fibre interferometer used as a hydrophone[10], magnetometers[11], and microbend type sensors for pressure measurements[12-15].

(ii) Extrinsic sensors

In an extrinsic sensor, light emerges from a feed fibre into an interaction zone in which this emerging light is modulated and is collected either by the same or a second fibre prior to the transmission to the receiver. In extrinsic sensors the modulated parameter is either intensity (sometimes via indirect means involving, for instance, variable birefringence), colour or modifications to the baseband spectrum of the returned signal.

Included in this category are the so called time resolved sensors in which the decay time, for instance of a phosphor, is measured and is known to change with temperature, and vibrating element devices in which a mechanical resonant frequency is caused to vary the modulation frequency of the return signal.

The two classes of intensity sensors and their subclasses are shown in Fig (1.6). In the following sections, the sensor mechanisms of the subclasses will be briefly defined and described, and examples will be given.

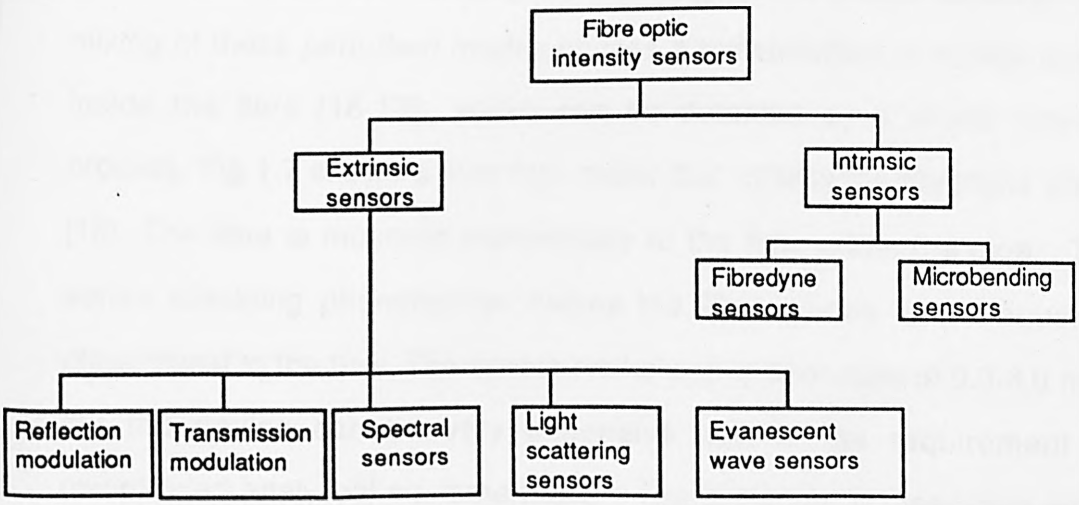

Fig 1.6 This shows schematically a number of classes of intensity sensors

1.3 Intrinsic Sensors

Intensity modulation sensors can be constructed, where the intensity modulation is performed within the optical fibre itself. Generally there are two types of intrinsic modulation phenomenon which are useful , the "fibredyne" effect and the microbending loss effect. These effects when utilized properly can lead to highly versatile fibre optic sensors that use a continuous length of optical fibre.

1.3.1 "Fibredyne" sensors

If a multimode fibre is mechanically twisted or bent, each of the optical modes within the fibre undergoes a change in its phase velocity. The mixing of these perturbed modes causes a redistribution of optical power inside the fibre [16-17] which can be detected by a model filtering process. Fig 1.7 shows a fluid flow meter that utilizes the fibredyne effect [18]. The fibre is mounted transversely to the flow within the pipe. The vortex shedding phenomenon makes the fibre vibrate at a frequency proportional to the flow. The sensor works well at flow rates of 0.3-3.0 m/s, but the device can be very expensive due to the requirement of complicated analytical equipment and it has problems in measuring large flow rates.

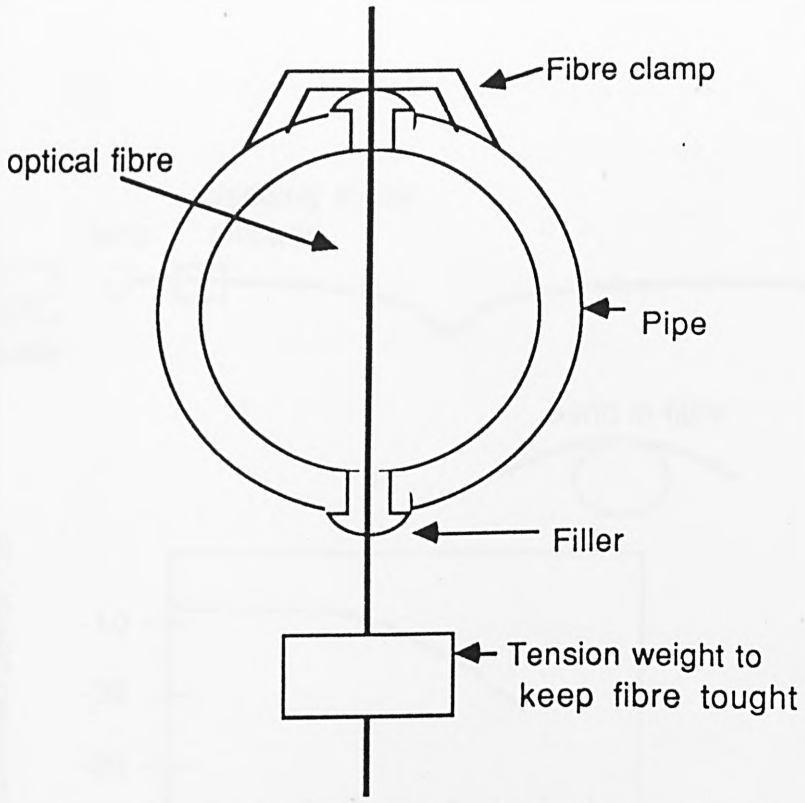

Fig 1.7 An optical fibre flowmeter based on "fibredyne" intensity modulation

1.3.2 Microbending Fibre Optic Sensors

The transmission loss of an optical fibre will increase when the fibre is subjected to microbending [19]. Many theories exist for light transmission through a optical fibre under microbending. Basically guided optical modes in the fibre core are coupled out from the core region in to the cladding region of the fibre as the fibre is bent. This can be viewed as simply due to the changing optical incidence angle at core-cladding

boundary as the fibre is bent.

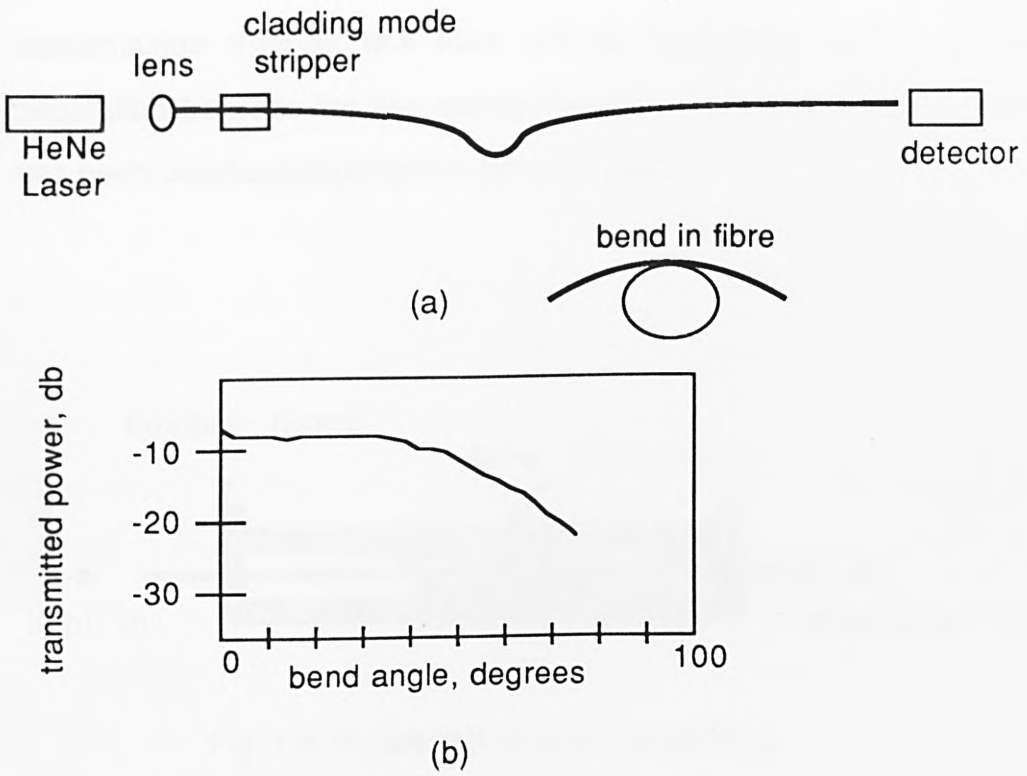

Fig 1.8 Microbending loss in an optical fibre [1]
(a) Experimental apparatus
(b) Response curve

In order to make a good fibre optical intensity sensor, these cladding modes have to be removed in order to prevent light coupling back from the cladding to the core again [20]. Such reversed coupling causes strong oscillations in the core mode power as a function of bending and hence affects the sensor reliability. Fig 1.8 shows the response of an optical fibre

subject to microbending.

A displacement sensor can be constructed by placing an optical fibre between two corrugated plates [21-22] as shown on Figure 1.9. The light transmission through this fibre will be modulated by the physical separation between the two corrugated plates. A structure strain sensor has been constructed using this principle [22].

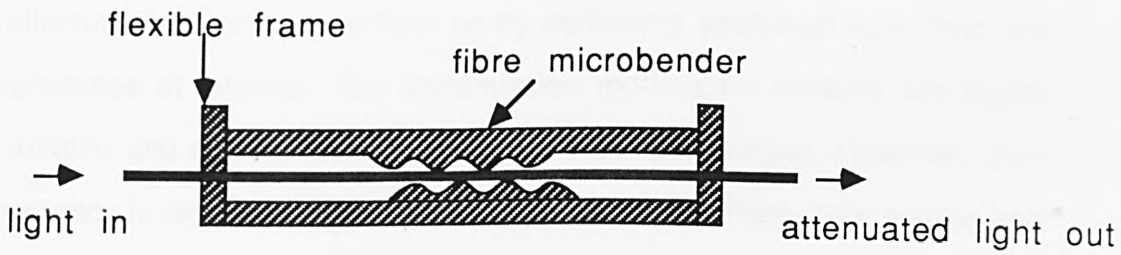

Fig 1.9 Illustration of a microbending fibre optic sensor

Although this sensor showed some promise for sensing pressure, there are however, several problems associated with it, such as long term reliability, thermal response, and the quality of the fibre link stability, amongst others.

1.4 Extrinsic Sensors

This is the largest class of optical fibre intensity sensors due to the large variety of optical processes or light modulation devices that may be attached to an optical fibre as a sensor. Most of these devices work on the interruption of light transmission path with varying degrees of sensing range and linearity. Non-linear sensors are useful as threshold sensors for the detection of the existence or the proximity of objects. Linear systems are useful in giving the quantitative status of the parameter of interest. It is also possible to construct fibre optic intensity sensors by reflecting light from a surface or by collecting scattered light from the substance of interest. The transmission modulation sensors are highly versatile and can be modified to sense most parameters. However, their accuracy is restricted by the fibre transmission variations, light source and photodetector drifts, and the convertion of the return signal from analogue to digital (A/D) in the monitoring device. Reflection modulation sensors are often used as non-linear sensors or on-off switch signal sensors. The scattering sensors often generate a frequency modulated optical intensity or an optical spectral shift, and the sensor accuracy is not much affected by intensity fluctuations due to the transmission.

1.4.1 Reflection Modulation Sensors

In this class of sensors the guided light is allowed to reflect from an optical interface which is modulated by an external driving force. Light can be reflected either from a mirror like surface or from total internal reflection.

Generally this class of sensor tends to have non-linear responses at small range.

One of the simplest optical sensors is the liquid level sensor developed at TRW and at Lewis Engineering in 1982. One of the approaches for sensing of liquid levels is shown in Fig 1.10. It works on the elimination of a glass/air interface i.e. the total internal reflection surface by making contact with the liquid. Thus an "on-off" type signal can be detected as light goes through the reflective surface on the contact of the liquid. This type of sensor can also be constructed by liquid contact to the exposed fibre core. This type of sensor has major wetting problems, i.e. as the sensor tip is withdrawn from the liquid there is a thin film left attached to the tip of the sensor due to surface tension effects, this causes losses indicating a false liquid level or an error in the readings.

Another generic design is based on the light collection efficiency by an optical fibre in a broken optical fibre path [23]. In Fig 1.11, light launched from the end of one fibre reflects from the surface and is collected by the second fibre. The light collection efficiency is very sensitive to the gap between the fibre end surfaces, and the reflecting surface quality. In production of such a sensor, this can lead to quality control problems where the reflecting surfaces have to be maintained throughout the useful life of the sensor.

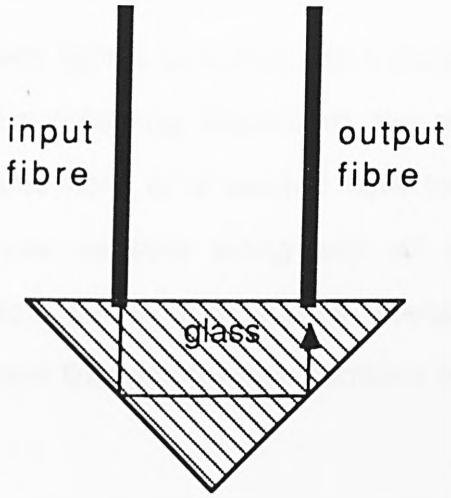

Fig 1.10 Liquid level sensor

Most linear displacement sensors can be employed to convert conventional mechanical sensors to fibre optic intensity sensors such as pressure sensors, acoustic sensors, temperature sensors, flow sensors, etc. Fig 1.12 illustrates the coupling of a reflective displacement sensor

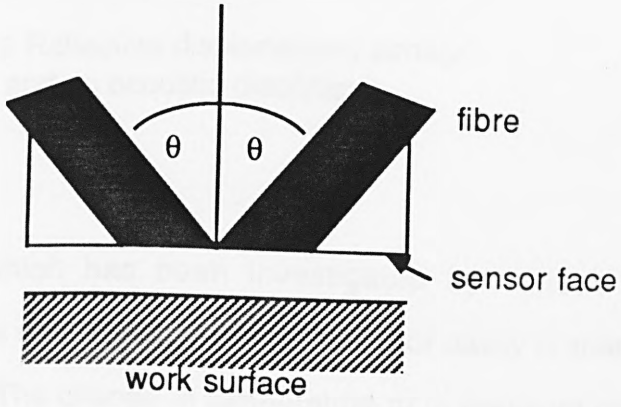

Fig 1.11 Fibre optic displacement sensor

and an acoustic diaphragm to and from a fibre optic reflection microphone

[24]. In these cases light is launched into a multimode fibre and is guided to the vicinity of a reflecting diaphragm, the reflected light is collected either by the same fibre or a second fibre to be guided to a remote detector. This type sensors along with all other types of intensity modulation sensors suffer from source intensity fluctuation problems coupled with thermal fluctuation which combine to reduce the sensitivity of the devices.

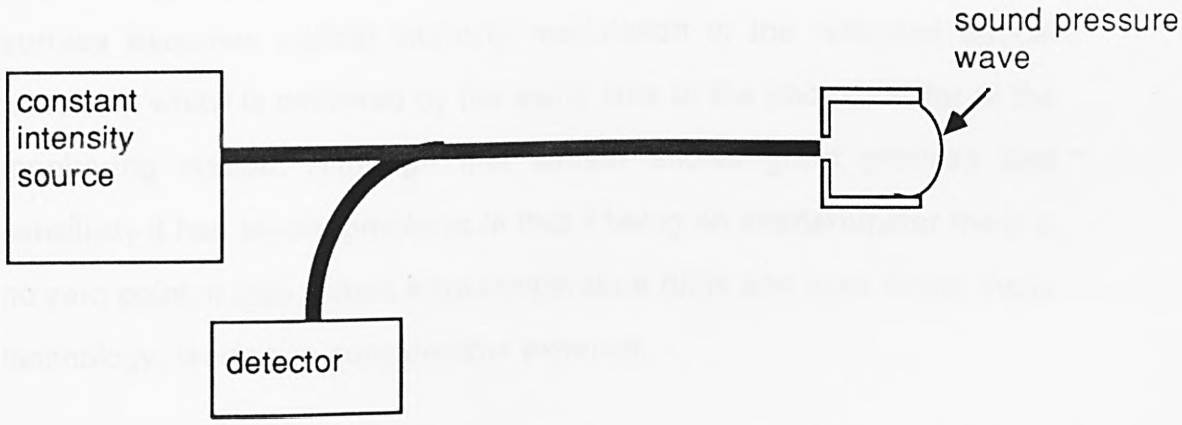

Fig 1.12 Reflective displacement sensor
and an acoustic diaphragm

Another approach which has been investigated by various workers [39,40,41], a miniature optical Fabry-Perot resonator cavity is made at the tip of an optical fibre. The change in temperature or in pressure can cause the Fabry-Perot resonator cavity length to vary, resulting in changes in the fibre and surface reflectivity, thus, a temperature sensor or a pressure

sensor can be made by this approach. Although this type of sensor shows high sensitivity it has a small dynamic range and sophisticated detection systems are necessary.

A vibration sensor has also been constructed to detect minute vibrations using a single mode fibre [25]. The end of a single mode fibre is placed close to a vibrating surface. The minute vibrations of the sample surface modulate the phase of the reflected optical wave form which is collected by the same fibre and interferometrically added to the optical reflection from the fibre end surface. The phase modulation due to the vibrating surface becomes optical intensity modulation in the reflected optical waveform which is delivered by the same fibre to the photodetector at the monitoring station. Although this sensor shows great promise and sensitivity it has severe problems in that it being an interferometer there is no zero point; it also suffers from temperature drifts and uses single mode technology, leading to considerable expense.

1.4.2 Transmission Modulation Sensors

Fibre optic displacement sensors can be constructed using miniaturized mechanical shutters at the end of optical fibres, or where the the intensity of the light transmitted from one fibre to another is reduced or decreased to zero as a result of an interruption, e.g. a shutter passing between an input and an output fibre. Variations on this theme include modulation of the received light due to displacements to one of the fibres, either in an angular, longitudinal or transverse mode, as shown in Fig 1.13. An optical microswitch based on this principle is being marketed by Delta Controls

(UK) [26].

Shutter devices can be actuated from simple spindle rotation or displacement mechanisms leading to an interruption in the beam between the opposed optical fibres. Some devices can be designed for compatibility for available electrical switch technology. It has been found that design tolerances to reduce transmission loss and crosstalk are extremely difficult to meet. The positioning and the alignment of the components is very critical if the switch is to provide consistent and reliable outputs.

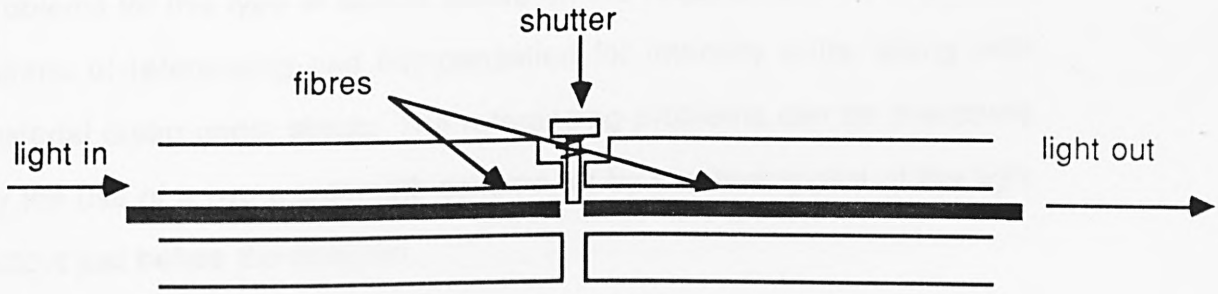

Fig 1.13 Operation of interruption-type sensor

There are also some non-mechanical types of transmission modulation sensors. One design uses the photoelastic effect or the Faraday effect to rotate the optical polarization between a pair of optical polarizers as the modulation technique [27-28]. An example is shown in Fig. 1.14. The light

emerging from a multimode optical fibre of sufficient length contains a large number of spatial and temporal modes that are equally divided in intensity into two orthogonal polarization states. Thus the first polarizer will allow half of the optical power to enter the glass block with a well defined polarization status. The second polarizer located behind the glass block, is aligned in the crossed state relative to the first polarizer so that no light will enter the output optical fibre unless the optical polarization is altered in the block. The light polarization modulation can be achieved by the photoelastic effect when pressure is applied to the glass block, this modulation is sinusoidal in nature leading to a low dynamic range. Other problems for this type of sensor centre on the requirements for a suitable means of referencing and compensation for intensity drifts, along with material creep under stress. The referencing problems can be overcome by the use of a two wavelength scheme, or by monitoring part of the light output just before the analyser.

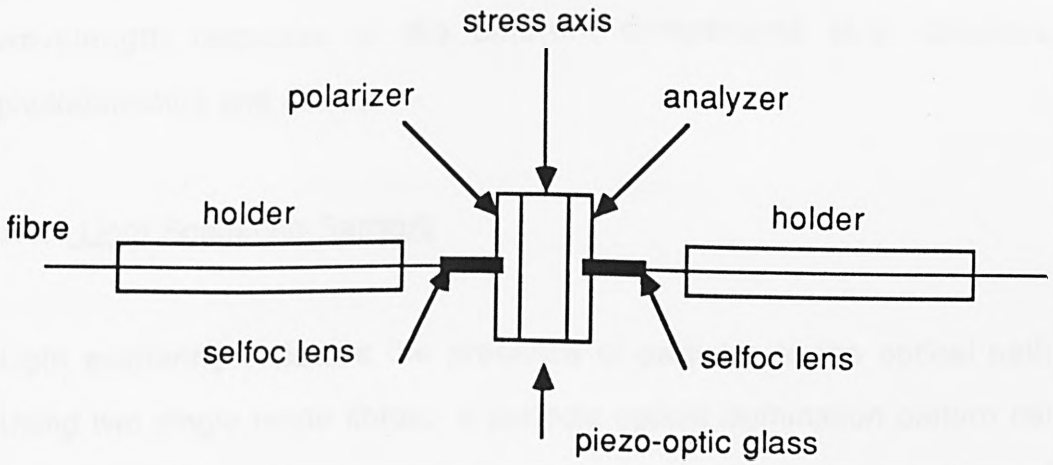

Fig 1.14 Photoelastic fibre optic intensity sensor

1.4.3 Spectral Sensors

In this class of sensor, optical fibres are used to transmit optical emission from the object to be studied, which is monitored at a remotely located optical spectrometer. One of the simplest of this type of sensor is a temperature sensor based on the black body radiation of a heated fibre tip. The temperature is measured by the analysis of the spectral components of the optical power received at the remote photodetector [29]. Resolutions of about 1^0C over the range of 400^0C-1100^0C have been reported [29], this sensor however has limited has limited use at lower temperatures.

Another device uses the multicolour fluorescence of rare earth compounds at high temperature. The relative intensity of spectral lines depends on the temperature of the compound which is optically pumped, numerous variations on this theme are possible[30,42]. However, various problems for such systems arise from the matching, stability and wavelength response of the different components (e.g. couplers, photodetectors and filters).

1.4.4 Light Scattering Sensors

Light scattering indicates the presence of particles in the optical path. Using two single mode fibres, a periodic optical illumination pattern can be generated and the crossing of a particle over this periodic pattern will give rise to an oscillatory scattered light intensity. The oscillatory frequency is directly proportional to the particle velocity. Fig. 1.15

illustrates an optical fibre flow velocity sensor based on this principle [43],

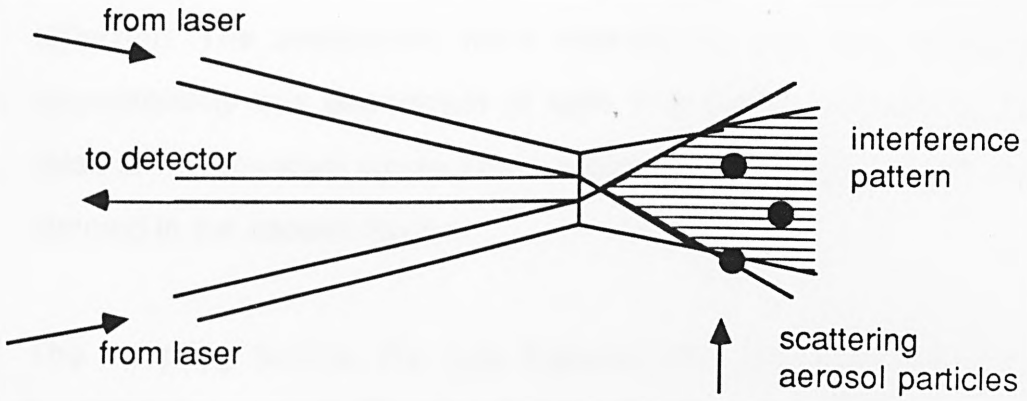

Fig 1.15 Fibre optic flow velocity sensor

Another optical fibre flow velocity sensor uses a Doppler frequency shift in light scattered back from moving particles. The Doppler frequency shift is proportional to the particle velocity component parallel to the light propagation direction. This Doppler shift in the optical carrier frequency is not detectable by photodetectors unless an optical reference frequency is provided in an interferometric arrangement . For instance, a homodyne process uses the reflection from the fibre end surface as optical reference to interfere with the Doppler shifted back scattered light has been demonstrated to monitor blood flow in vivo [31]

1.4.5 Evanescent or Coupled Waveguide Sensors.

An evanescent wave is created at a boundary where there is total internal reflection. The evanescent wave extends into the rarer medium for approximately one wavelength of light. If a second medium is placed close to the boundary where TIR is occuring, some light intensity can be oberved in the second medium

The coupling across the gap between the two media decreases exponentially as the gap size increases. This technique for intensity modulation has the potential for being a very sensitive modulation technique. Evanescent wave coupling lends itself quite easily to the detection of movements which are of the range of a wavelength of light, with a potential accuracy of several nanometers. The sensitivity of any system using this method will depend upon the wavelength of light used, since the evanescent wave only penetrates into the rarer medium of the order of one wavelength. So the maximum movements detected would be approximately one wavelength.

A number of sensors have been developed using this technique. A displacement sensor was developed by Sheem & Cole [32] using two single mode fibres (in 1979).

When the cores of two fibres are newly adjacent over some distance as shown in Fig.1.16, light is coupled from one core to the other. For single mode fibre, Sheem & Cole [32] have calculated the modulation index:

$$Q = \mathrm{Sin}(\pi L/l)\{\pi L/Vl[(WV/\rho)C_d+(3+VD_o)(2\pi\rho/\lambda)$$
$$.(n_1^2-n_2^2)^{-1/2}\ (n_1C_{n1}-n_2C_{n2})+(3+VD_o)(2\pi/\lambda)$$
$$.(n_1^2-n_2^2)^{1/2}\ C_\rho]+2\pi c_L/l\} \qquad \text{--------(1.2)}$$

n_1 = refractive index of fibers

n_2 = refractive index of air

where L is the interaction length, l is the beatlength, V and W are parameters which depend on model properties of the fibre, r is the core radius, D_o is the ratio of the core separation to the core radius, and n is the index of refraction of the medium between the two cores. The transduction coefficients C_d, C_{n1}, C_{n2}, C_r, and C_L are the rate of change with pressure of the core separation, core index, medium index, core radius, and interaction length, respectively. As can be seen, several physical effects take place to yield the resultant sensitivity.

Although single-mode technology was used to demonstrate this principle, one of the main advantages of intensity sensors is that they may be fabricated with multimode fibres. Evanescent type sensors have been demonstrated in multimode fibres with excellent results[33-35].

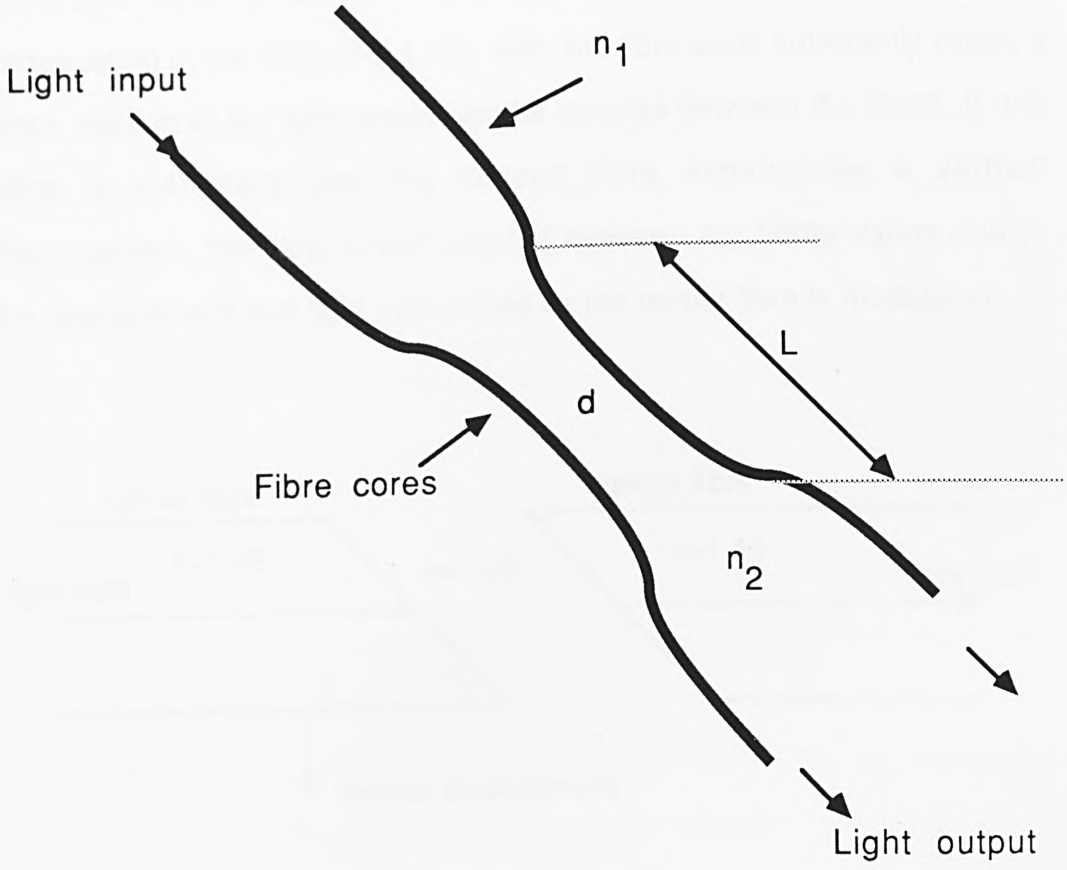

Fig 1.16 Evanescent or coupled waveguide sensor

1.4.6 Frustrated-Total-Internal-Reflection Sensors

A sensor using the frustrated-total-internal-reflection (FTIR) effect [36] usually consists of two fibres with their ends polished at an angle to the fibre axis which produces total internal reflection (TIR) for all modes propagating in the fibre (Fig 1.17). With the fibre ends sufficiently close, a large fraction of the light power can be coupled between the fibres. If one fibre is stationary and the second fibre experiences a vertical displacement, the light power coupled between the fibres varies due to the displacement and light transmitted by the output fibre is modulated.

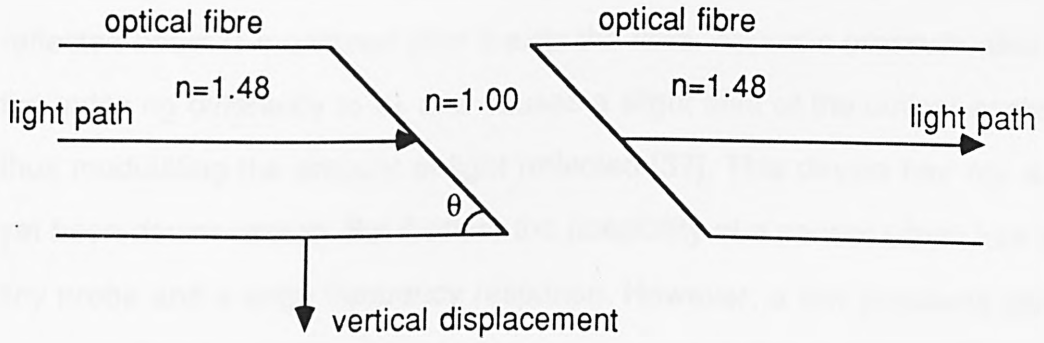

Fig 1.17 Frustrated-Total-Internal-reflection mode sensor.

A sensor using this principle has been demonstrated by Spillman and McMahon [36], in which two fibres cut at the critical angle, were aligned one stationary and the other attached to a diaphragm to make a hydrophone (a more detailed description of this sensor along with that

produced by Beasley [34-35] can be found in chapter 3). This sensor demonstrated great sensitivity and response but unfortunately it required critical alignment and therefore required extremely tight mechanical tolerances.

1.4.7 Near-Total-Internal-Reflection Sensor

The near-total-internal-reflection (NTIR) sensor or the critical angle sensor (Fig 1.18) is very similar to the FTIR sensor. The NTIR sensor employs a single mode fibre cut at an angle just below the critical angle. If the critical angle (given by $\theta_c=\sin^{-1}(n_2/n_1)$) is not near 45^o (45^o requires medium 2 to be a gas) then an additional angular cut is needed to allow the reflected beam to travel back through the fibre (Fig 1.18). This back reflected beam is monitored after it exits the fibre. Acoustic pressure alters the index n_2 differently to n_1 and causes a slight shift of the critical angle, thus modulating the amount of light reflected [37]. This device has not as yet been demonstrated. But it offers the possibility of a sensor which has a tiny probe and a large frequency response. However, a few problems can be envisaged, including dynamic range and nonlinearity due to the shape of the reflectivity curve near θ_c.

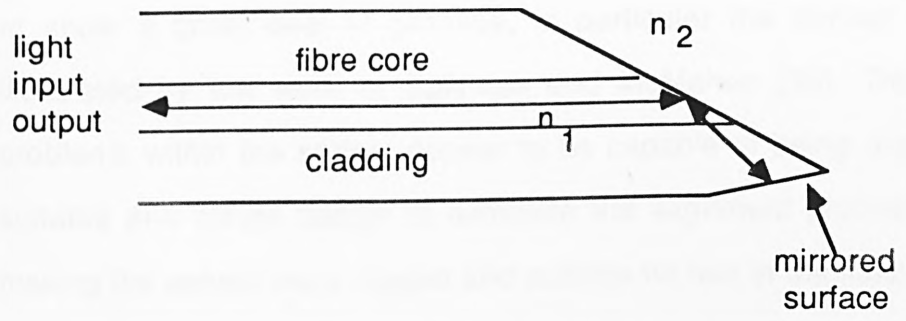

Fig 1.18 Near-total-internal-reflection sensor

1.5 Conclusions

As a result of several years of research, a well developed technology in the area of fibre optic sensors has been produced. Substantial progress has been made and has manifested in the form of new classes of sensors with sensitivity and versatility; complete optical systems appear to be feasible.

In this chapter an outline of the advantages of optical fibre sensors has been discussed as well as a number of existing problems. Amplitude sensors have been demonstrated for sensing magnetic fields, acoustic levels, acceleration, temperature, liquid levels, displacement, strain, and pressure and offer cheap, easy to fabricate sensors suitable for harsh environmental deployment.

Of the sensors discussed above, those utilizing the evanescent field

created at the end of a critically cut fibre (FTIR, NTIR type sensors) appear to show a great deal of promise, in particular the sensor technique illustrated by the work of Spillman and McMahon [36]. The inherent problems within the sensor appear to be capable of being overcome by suitable and clever design to eliminate the alignment problems, hence making the sensor more rugged and suitable for use in the field.

1.6 Aims of this work

A great deal of work has been done recently in producing viable fibre optic sensors for a varity of applications. Of these applications pressure sensing seems to be very important, there is therfore a need for good reliable optical pressure sensors which can be cheaply produced, and have very high accuracies.

In this work the FTIR effect is used to produce an amplitude modulated pressure sensor in the first instance; this idea was then expanded to produce a digital pressure sensing device. In chapter 2 there is a theoretical analysis of the equations showing the coupling of light between two optical elements via the evanescent field or the FTIR effect. A computer program was generated to model this coupling and predict the transmission across an air gap between the two optical elements. In chapter 3 the experimental arrangement for an analogue device is described along with the results obtained in a laboratory test.

A hybrid optical-electrical digital pressure sensing device was constructed

by driving photovoltaically a quartz crystal into resonance. The amplitude of vibration was monitored by directly monitoring the intensity of light present within the quartz crystal as it moved closer to and further away from a critically cut fibre. Thus the resonance frequency was sensed with an optical technique. When a force was applied to this resonant system, there was a change in the resonance frequency which was found to be proportional to the applied force, hence giving an amplitude modulated digital force/pressure sensor (chapter 4).

In chapter 5 a photothermal drive system for the quartz resonator is evaluated, and its suitability for use in an all-optical digital force transducer is discussed.

The work is discussed at length and compared and contrasted with other published information.

Chapter 2

Frustrated total internal reflection (F.T.I.R)

Abstract

The theory of evanescent wave coupling (FTIR) between two optical elements is presented, begining with simple rays at an interface, leading to TIR and FTIR. The chapter concludes with the effect of the change in the gap size between two optical elements to the coupling of light across the gap.

2.1 Introduction

In chapter 1 it was noted that pressure sensors using the principle of F.T.I.R. (or Evanescent wave coupling) showed a great deal of promise for high sensitivity sensor systems. In order to gain an understanding of F.T.I.R. it is necessary to understand the interaction of a plane light wave with an interface between two dielectric media. In this chapter the nature of the interaction will be investigated starting with a plane wave interacting with a boundary and leading to the phenomenom of Total Internal Reflection (T.I.R.) and Frustrated Total Internal Reflection (F.T.I.R.).

2.2 Rays at an Interface.

Whenever a ray of light is incident on a boundary separating two different dielectric media, part of the ray is reflected back into the first medium and the reminder is refracted as it enters the second medium (Fig 2.1). The directions taken by these rays can best described by the laws of reflection and refraction.

According to the simplest of these laws, the angle at which the incident ray strikes the interface is exactly equal to the angle the angle the reflected ray makes with the interface. The second law is concerned with the incident and refracted rays of light, and states that the sine of the angle of incidence and the sine of the angle of refraction bear a constant ratio to one another, for angles of incidence:

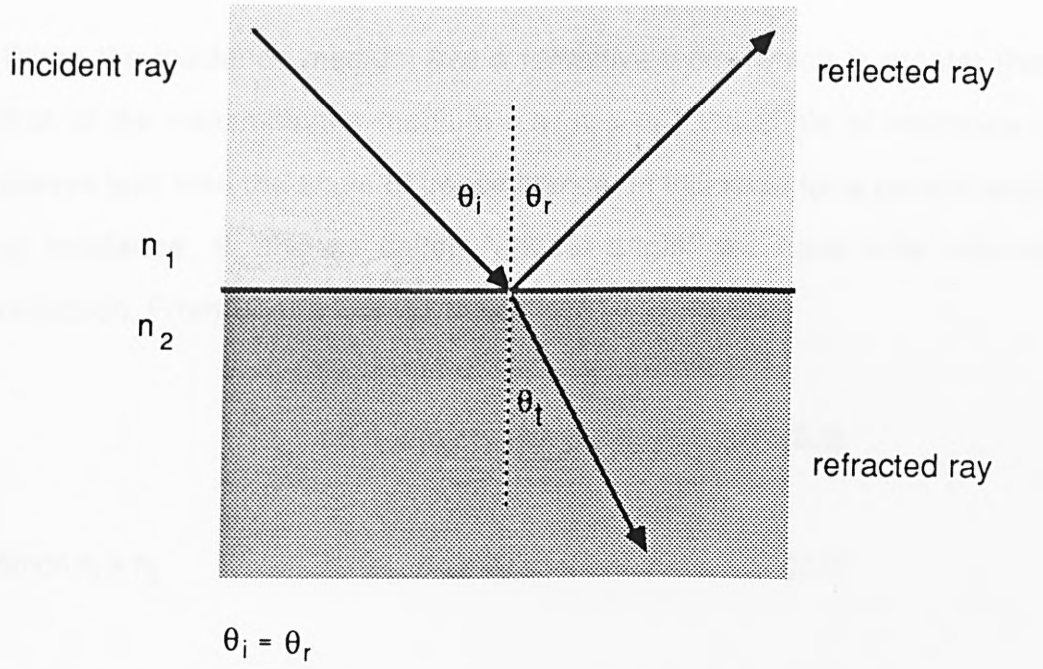

Fig 2.1 Refelection and refraction at a boundary between two media with refractive indices n_1 and n_2

$$\sin \theta_i / \sin \theta_t = \text{constant} \qquad (2.1)$$

The constant is the ratio of the refractive indices of the two media n_i and n_t. Hence equation (2.1) can be writen in the form:

$$\sin \theta_i / \sin \theta_t = n_t/n_i \qquad (2.2)$$

(For a comlete dervation of these laws see Appendix A)

2.3 Total Internal Reflection

When the incidence medium has a refractive index which is greater than that of the transmittance medium (i.e. $n_i > n_t$) the angle of incidence is always less than the angle of transmittance. In this case for a certain angle of incidence, θ_c the so called "critical angle" we have total internal reflection. From Snell's law we have:

$$\sin \theta_i = (n_t / n_i) \sin \theta_t \qquad (2.3)$$

Since $n_i > n_t$ $\qquad (n_t / n_i) = n_{ti} < 1 \qquad (2.4)$

therefore as θ_i becomes larger, the transmitted ray gradually approches tangency. And more and more of the available energy appears in the reflected beam. When $\theta_t = 90$, $\sin \theta_t = 1$.

Therefore $\qquad \sin \theta_c = n_{ti}$

The critical angle is that special value of θ_i for which $\theta_t = 90^o$. For incident angles greater than θ_c all of the incident energy is reflected back into the incident medium, giving total internal reflection. This is shown in Figure 2.2.

If the asumption is made that there is no transmitted wave when the angle of incidence increases beyond the critical angle, the boundary conditions are not satisfied with the use of the reflected and the incident waves only.

In order to satisfy the boundary conditions there must exist a transmitted wave which does not on average take any energy across the boundary, this wave is complex in nature and has the form:

$$\mathbf{E}_t = E_{ot}\ e^{\pm\alpha y}\ \ ei[\ (\ k_t x\ \sin\theta_i\ )/\ n_{ti}\ -\ \omega t\ ] \qquad (2.5)$$

Where;

$\mathbf{E}_t$ = electric field vector of the transmitted wave

E_{ot} = transmitted wave amplitude

k_t = transmitted wave vector

ω = angular frequency of the wave

α = component of the transmitted wave vector in the y direction

The positive exponential can be neglected which is physically unattainable, we have a wave whose amplitude decreases exponentially as it penetrates the less dense medium. This wave travels along the x-direction and is called the evanscent wave. Where the x-direction is along the boundary, and the y-direction is perpendicular to it.

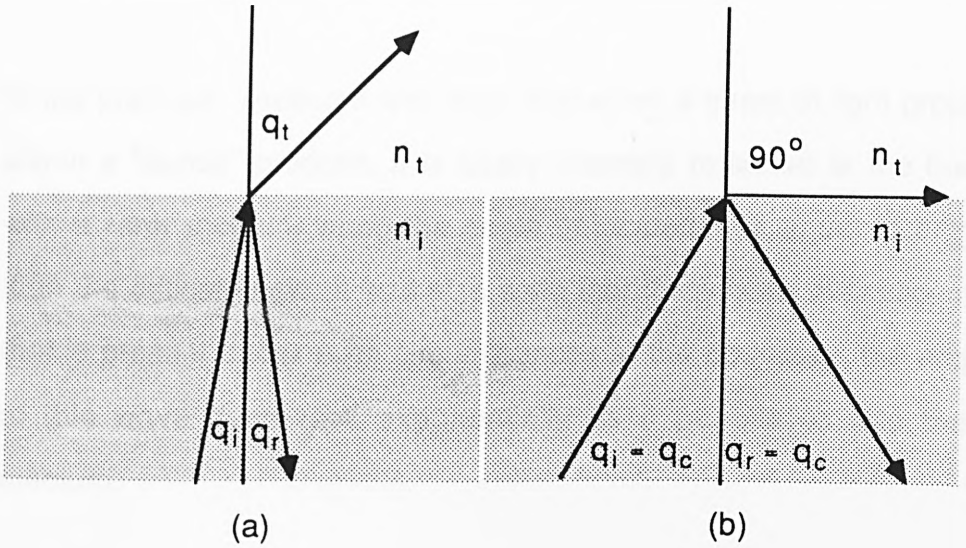

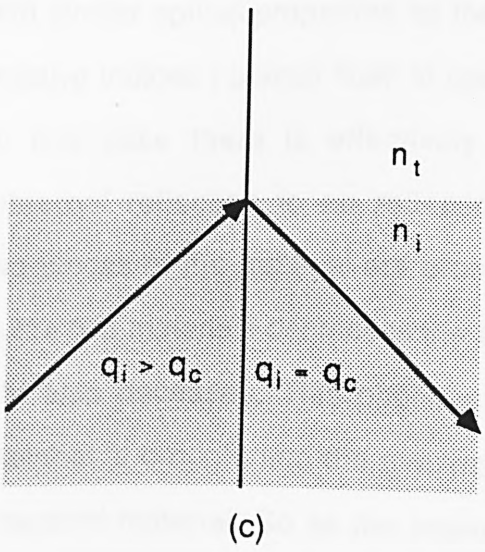

Fig 2.2 Schematic of total internal reflection conditions ($n_i > n_t$)

2.4 Frustrated Total Internal Reflection (Evanescent Wave coupling)

In the previous section it was seen that when a beam of light propagates within a "dense" medium, it is totally internaly reflected at the boundary with a rarer medium when the angle of incidence is equal to or greater than the critical angle. It was also seen that there is an evanescent wave that is present under such circumstances at the boundary, the amplitude of this wave decreases exponentially as it penetrates into the rarer medium.

The total internal reflection at the boundary can be eliminated by placing a piece of material with similar optical properties as the dense medium (i.e similar or equal refractive indices) placed flush in contact with the original dense medium. In this case there is effectively no boundary. This condition of total internal reflection to no reflection can be achieved gradually, as the two pieces of the material are brought together. That is as the gap between the two materials decreases the amplitude or intensity of the reflected light also deceases. This phenonena occurs because, when the second material is brought into the evanescent field some light is coupled into the second material. So as the intensity of reflected light decreases, the coupled intensity in the second material increases.

An expression for the transmission (T) of the light across the air gap between the two materials is shown below both for light propagating with its plane of polarisation perpendicular to the plane of incidence (figure

2.3):

$$T_{\perp} = 1 - (Z^2 + \delta^2)^2 [(Z^2 - \delta^2) + 4Z^2 \delta^2 \coth^2 \beta]^{-1} \qquad (2.6)$$

$$\beta = (2\pi d/\lambda) [n_i^2 \sin^2\theta_i - 1]^{1/2} \qquad (2.7)$$

$$Z = 1/(n \cos\theta) \qquad (2.8)$$

$$\delta = - (n^2 \sin^2 \theta - 1)^{-1/2} \qquad (2.9)$$

and, for light polarized in the plane of incidence $T_{\parallel}$ is given by:

$$Z = (\cos\theta)/n \qquad (2.10)$$

$$\delta = (n^2 \sin^2 \theta - 1)^{1/2} \qquad (2.11)$$

A complete derivation of these equations can be found in appendix A.
The theoretical transmission into the third medium is shown in Figure 2.4, where the average transmission over both planes of polarisation has been calculated using FORTRAN program (a complete listing of which can be found in appendix B).

As the transmission into the third medium can now be predicted, a sensor using this principle can be designed for optimum performance since the computer programme can show the optimum angle to be used for the

critically cut fibre so that light from all the modes of the multimode fibre to be used.

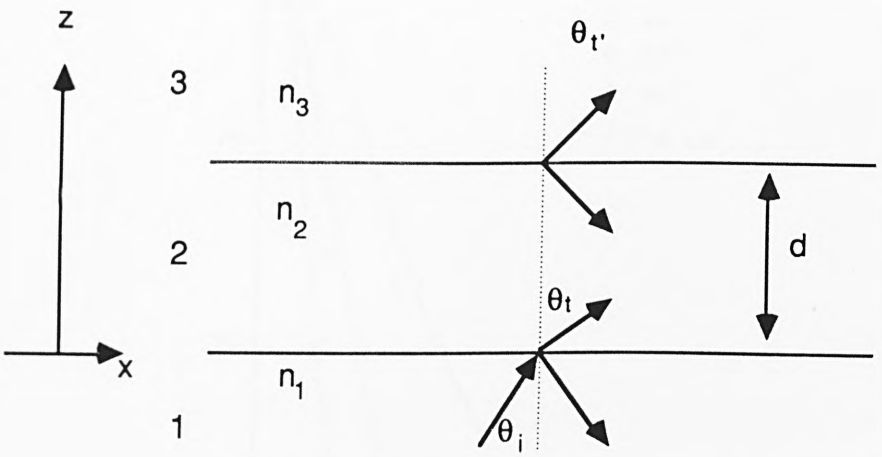

Fig 2.3 Schematic of two layers of dense media seperated by a less dense medium of thicness d

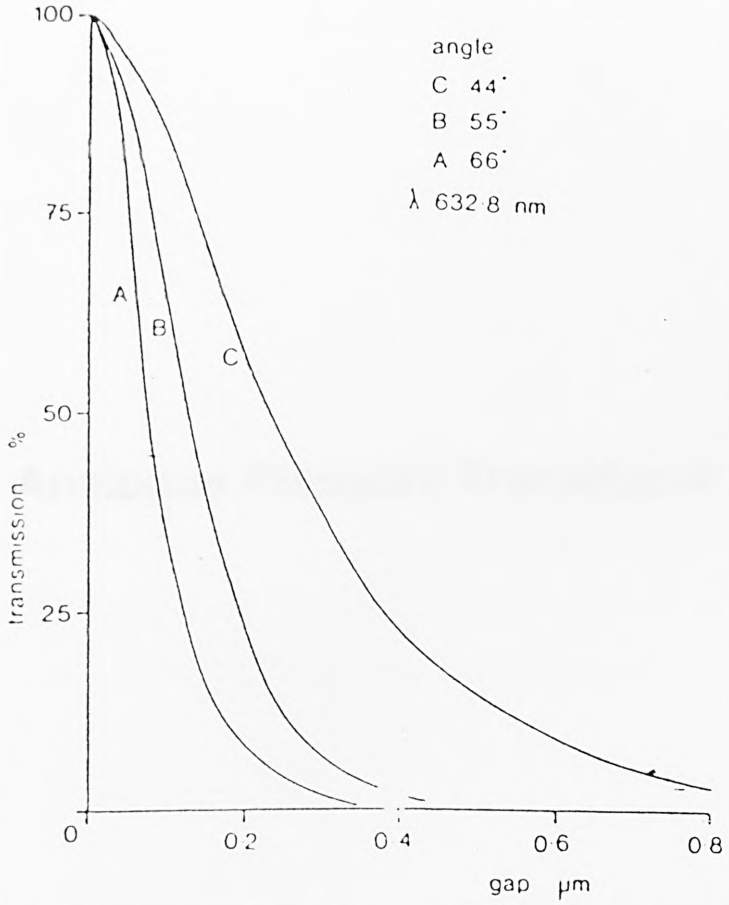

Fig 2.4 Shows the theoretical transmission across an air gap between two dielectric media

Chapter 3

Analogue Pressure Transducer

Abstract

In this chapter the design and construction of a simple fibre optic pressure sensor based on the principle of frustrated total internal reflection in fibre cut beyond the crtical angle are described. The characteristic of the device are obtained and compared with the prediction of a simple theory.

3.1 Introduction

A considerable effort in recent years has gone into the development of optical techniques using fibre optics for the measurement of a number of physical parameters (chapter 1). One of the most important parameters to sense in the industrial and laboratory environment is pressure.

A number of techniques have been researched by various workers in the field. Pressure sensors using various effects such as pressure induced phase changes in fibres & reflection changes caused by pressure induced refractive index changes have been constructed. However, the approach of evanescent wave coupling between adjacent optical elements and pressure induced gap changes in the frustrated - total -internal - reflection (F.T.I.R) technique has shown considerable promise.

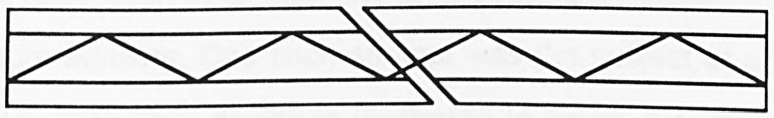

Fig 3.1 Schematic of two critically cut fibres

The work of Spillman & McMahon [36] resulted in the development of an F.T.I.R hydrophone using the light coupling between two adjacent fibres. In this device the F.T.I.R mechanism was exploited to induce modulation of light travelling from an optical fibre to another, through air, as shown in

figure 3.1. The two fibre ends were polished at an angle to the fibre axis large enough to cause total internal reflection for all the modes propagating in the fibre. By bringing the two fibre ends sufficiently close to one another (~ 1μm), a large fraction of the optical power was coupled between the two fibres. Modulating the gap thickness by means of relative vertical displacement between the two fibres caused the amount of the light power coupled between the fibres to be modulated.

Figure 3.2 shows the schematic of an apparatus used. The relative movement between the two fibres was activated by holding one fibre rigidly and the second fibre was attached to a diaphragm and spring. The experimental results achieved by this device are shown in Figure 3.3. As can be seen the experimental results differed from the theoretical predictions to a large degree.

There have been other attempts at producing Evanescent Wave Coupling pressure sensors. One such attempt was the subject of a U.S. Patent by Beasley [34]. This device is illustrated in figure 3.4. It consisted of two parallel fibres lying on top of each other. The top fibre was connected to a pressure plate and the lower fibre to a solid base. As the two fibres are squeezed together with application of pressure, light is coupled between the two fibres through the Evanescent Wave, and hence there is modulation of a signal passing through one of the fibres. Other attempts include a proposed F.T.I.R acoustic sensing method by Hull [44]. This involved the use of acoustic signals to modulate light coupled through the evanescent wave between two optical elements.

The devices discussed above all showed some considerable difficulties in their engineering. There were also some severe temperature stability problems which led to a loss of sensitivity and accuracy. However, they demonstrated the potential of evanescent wave coupling for use in optical sensors if a design could be found that eliminated these problems from the outset.

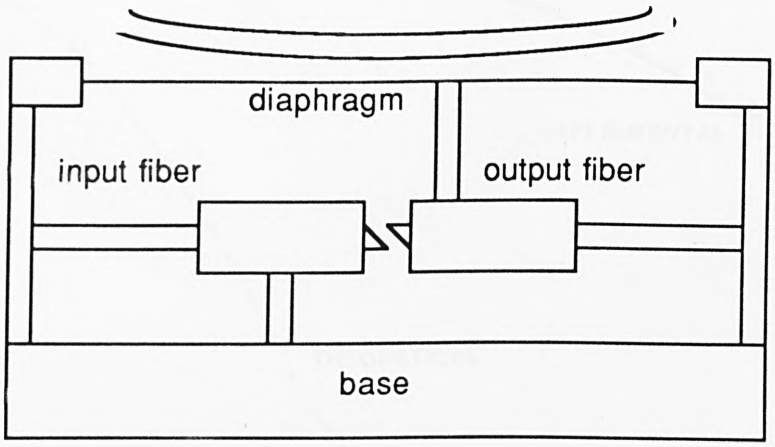

Fig 3.2 Schematic of hydrophone developed by Spillman and McMahon

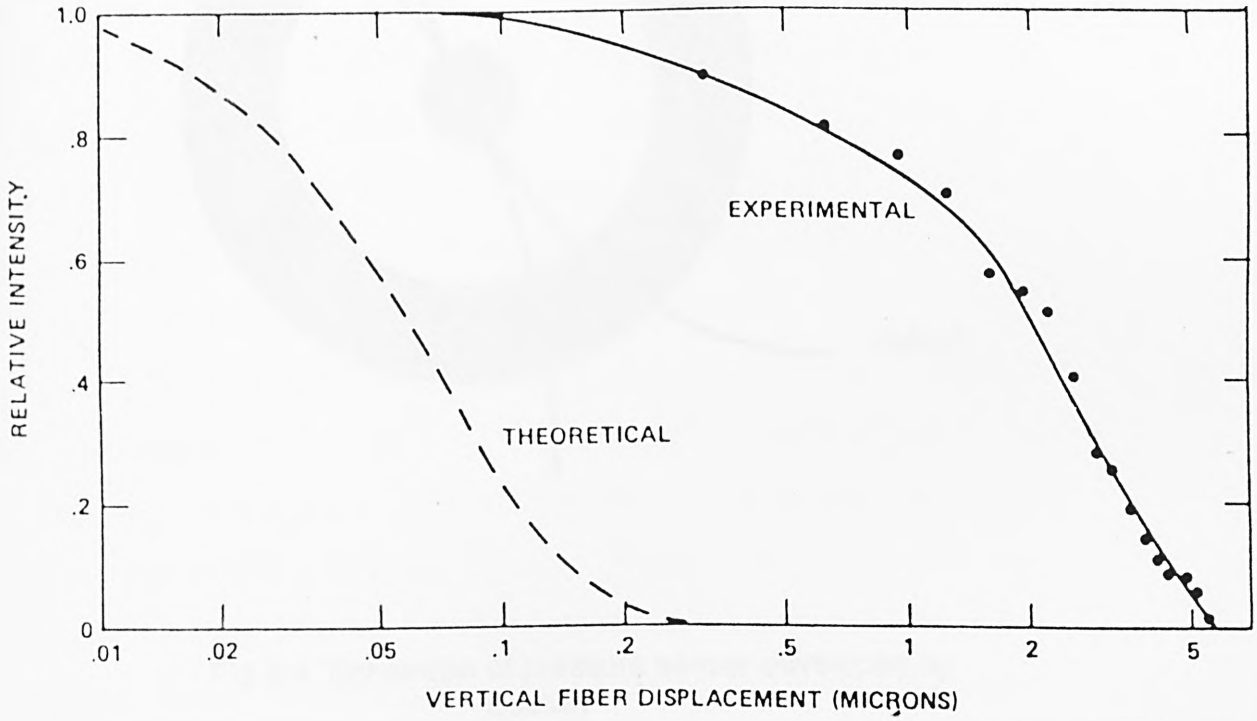

Fig 3.3 The experimental characteristics of the FTIR hydrophone

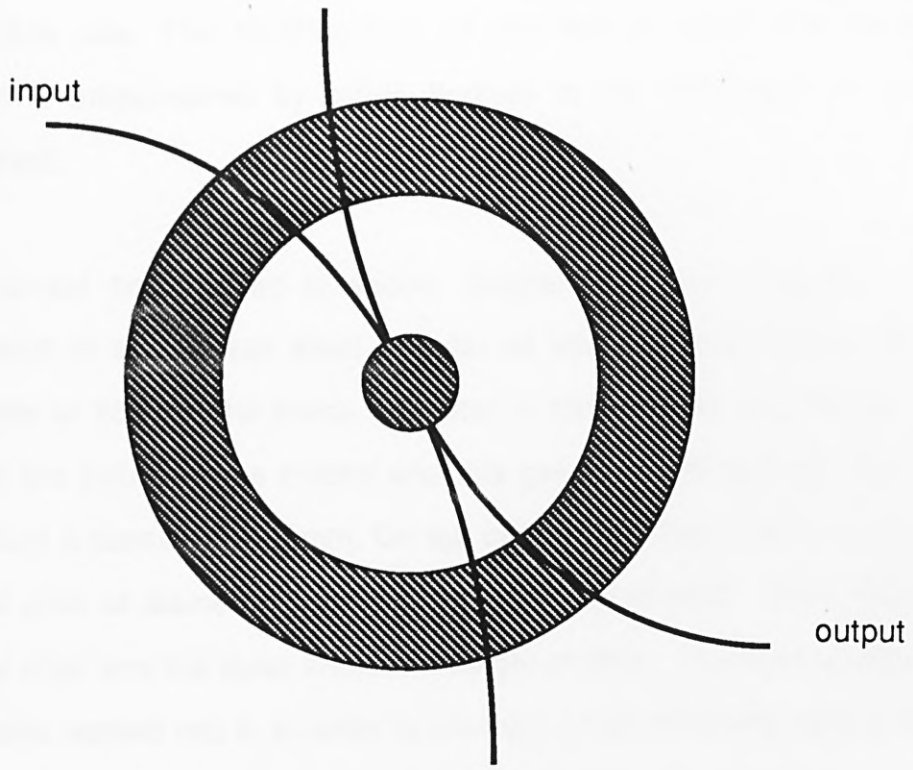

Fig 3.4 Schematic of pressure sensor developed by Beasley

3.2 Design of the sensor in this work

In overcoming the problem of designing and building an F.T.I.R pressure sensor, it was decided that there was a need for the development of a relatively simple device using a laser source of moderate power (a few milliwatts output from a He-Ne laser) which was nevertheless robust and

comparatively easy to construct, the input and output optical elements not requiring critical alignment before use and not likely to go out of alignment in routine use. The development of this device could overcome the problems encountered by other workers in the field such as critical alignment.

The sensor constructed is shown diagrammatically in figure 3.5. It consisted of a stainless steel cylinder of length 25mm and an overall diameter of 25mm. The inside diameter of this cylinder was 15mm. One end of the cylinder was closed and this gave a diaphragm of thickness 1mm and a diameter of 15mm. On top of this diaphragm was machined a central pillar of diameter 3mm and an outer rim of width 5mm. Both the central pillar and the outer rim had a height of 2mm. The central pillar had two holes tapped into it, in order to connect a light receiving optical flat to the diaphragm and the output optical fibre to the flat. A hole was drilled through the outer rim at an angle of 35° to the axis, into which a steel tube containing the input fibre was inserted . The top of the device (without the optical flat) was polished so that the input fibre had its end polished at 35° and the both of the surfaces of the central pillar and outer rim were left with a mirror finish with a flatness of the order $\lambda/10$. This arrangement enabled a minimization of the coupling differences which can occur between the fibre and plate with a straight surface.

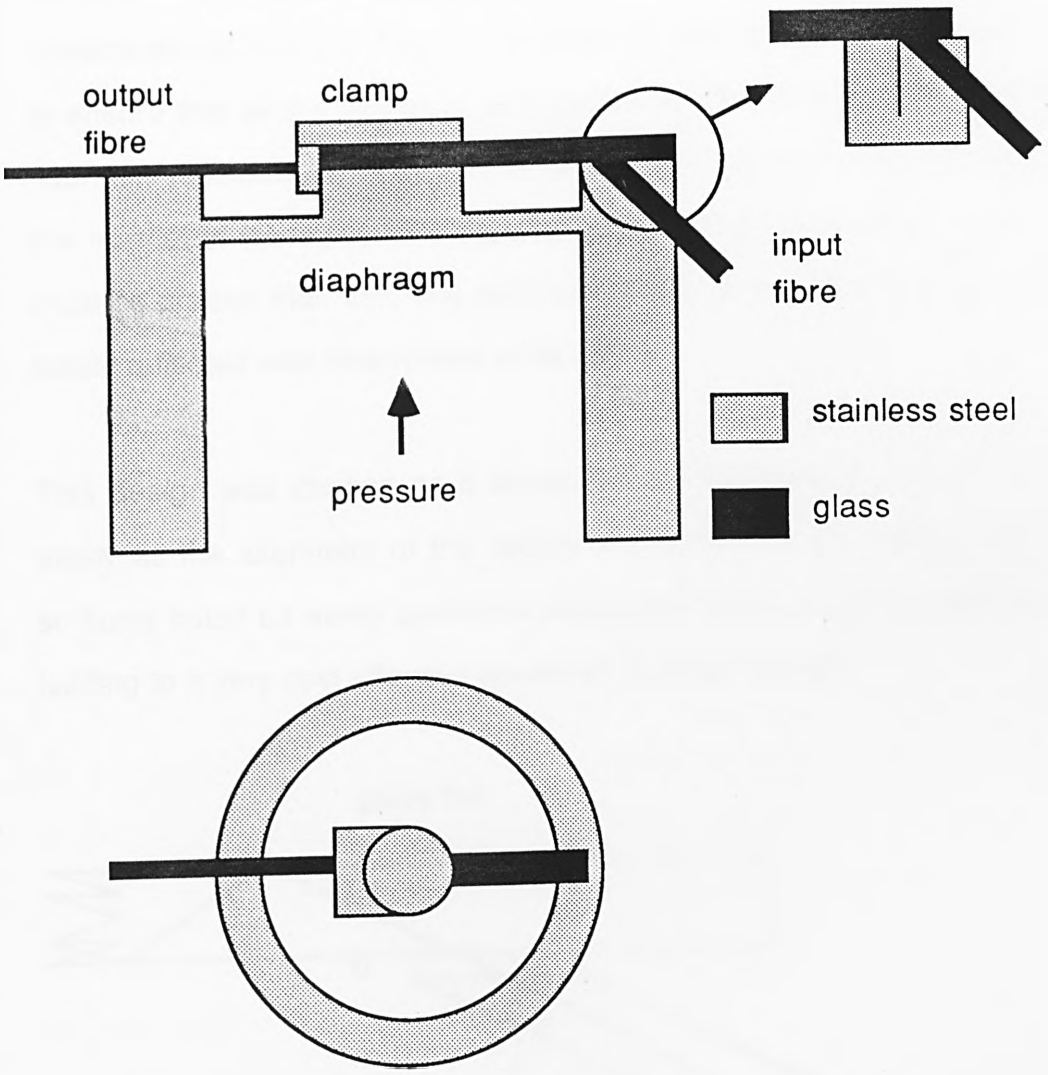

Fig 3.5 Schematic of analogue pressure transducer

The fibre used for both input and output fibres, was manufactured by B.I.C.C, of 400μm diameter, numerical aperture 0.27 and core refractive index of 1.46 [45]. The angle at which the input fibre was placed into the

device, to give T.I.R at its surface, was chosen with the following considerations in mind. The critical angle for the fibre used was ~43°, but to ensure that all the modes of propagation within the fibre are also totally internally reflected, i.e. to allow for the extreme "off axis" rays the angle to the normal of the input fibre must be greater than the critical angle, i.e. must be greater than 43°. The minimum angle for which all the modes are totally reflected was determined to be 55°.

This design was chosen as it alows the manufacture of such a sensor easily as the alignment of the optical elements was not critical. The flat surfaces could be easily produced using well known polishing techniques leading to a very cost effective sensor of a simple design.

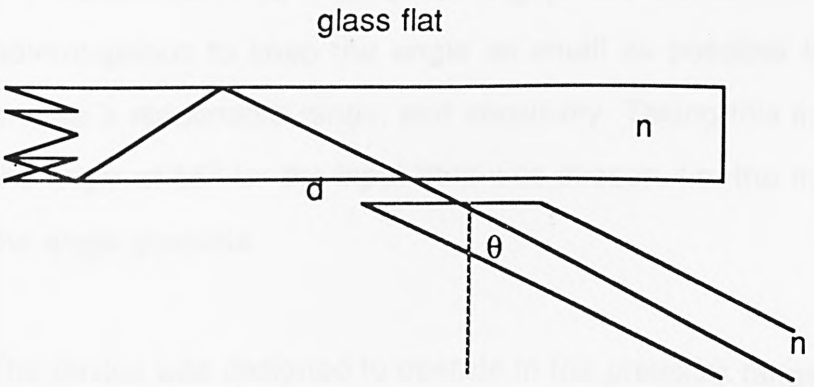

Fig 3.6 Schematic of evanescent wave coupling

A schematic of evanescent wave coupling is shown in Figure 3.6. It consists of two optical elements, an input fibre with its end polished at

angle θ to the axis to produce T.I.R. for all the modes which propagate in the fibre, and a polished glass flat which is rigidly connected to a diaphragm to allow the displacement of the two elements to be varied in response to the pressure applied to the diaphragm. With the elements sufficiently close, a substantial proportion of the input light energy can be coupled to the glass flat and second fibre connected to it, the light intensity decreasing as the separation of the element increases.

In section 2.4 it was shown that the transmission of light across the gap, T, through the Evanescent Wave is given in equations 2.6 - 2.11. These equations show that the transmission is not only a function of gap but also a function of the angle θ . Figure 3.7 shows the transmission with respect to the angle θ and the gap size. As can be seen, as the angle increases the transmission as a function of gap size decreases. Therefore it is advantageous to keep the angle as small as possible for the device to ensure a reasonable range, and sensitivity. Taking this into consideration the angle of 55° for the input fibre was chosen. i.e. the minimum value of the angle possible.

The device was designed to operate in the pressure range of atmospheric pressure to several bar above. A simple analysis of the displacement of a circular plate clamped at it's circumference and under uniform pressure [46] gives the following relationship for the maximum (central) displacement V :

$$V = 3\,(m^2 - 1)\,P\,r^4/16Em^2t^3 \qquad (3.1)$$

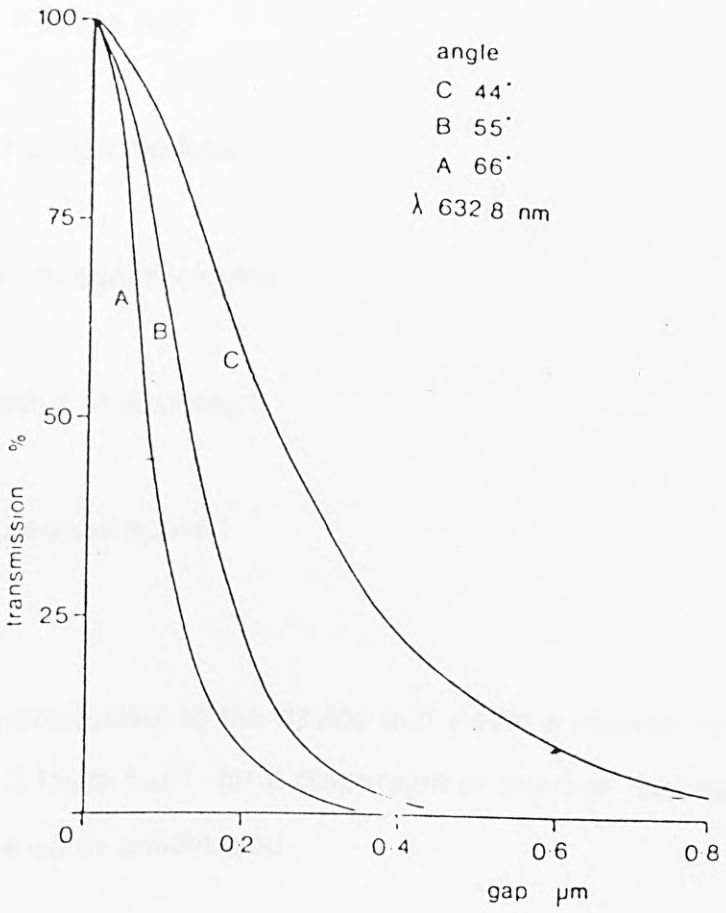

Fig 3.7 Transmission of light at 632.8 nm across a gap as a function of width for different angles of fibre cut

where

m = Poisson ratio

E = Young's modulus

t = diaphragm thickness

r = radius of diaphragm

P = pressure applied

This is a close approximation to the device and yields a displacement of the diaphragm of 0.15μm bar^{-1} for a diaphragm of average thickness of 1mm, which can be easily constructed.

The light source used in these experiments was a Spectra Physics stabilite laser type 124 giving ≤1mW output at 632.8 nm in a stable output mode and intensity. the amplitude stability of this was better than 1%. Light was launched into the input fibre using a 10x microscope objective with numerical apperture of 3.0. the output fibre was coupled directly into an optical power meter. The length of the input and the output fibres was 5

meters, with the first meter of the input fibre being tigtly wound to remove cladding modes.

3.3 Characteristics of Pressure Sensor

The characteristic response of the device in shown in Figure 3.8. This shows the normalized transmission (light received by the second optical element) as a function of pressure (above atmospheric pressure) applied to the diaphragm. A smooth curve is observed with negligible hysteresis over the pressure range studied with a total accuracy of measurement ~ +/- 5 per cent. A finite element analysis [47] was performed on a simple model of the device to determine the amplitude of deflection of the diaphragm as a function of pressure, the analysis was performed by computer programme package called FINEL. The device was modelled as a series of small elements upon which a pressure was acting. This indicated that the change in amplitude is linear as a function of pressure. Therefore the change in the gap between the input and output optical elements is also linear. The gap (in micrometers) for a value of pressure is also shown in Figure 3.8. This characteristic is compared with the calculated normalized transmission of a fibre cut at 55°, averaged over twelve angles in equal intervals from 44° to 66° . The averaging was carried out in order to try and simulate the experimental conditions, where due to the numerical aperture of the fibre, light leaves the transmitting fibre at a range of angles beyond the critical angle, and is also coupled to the receiving optical element.

A calculated transmission function of the device is shown in Figure 3.9.

This shows the calculated normalized transmission for a 55° cut fibre, averaging over twelve angles in equal intervals to allow for the experimental situation where, because of the actual numerical aperture of the fibre, light may leave the transmitting fibre at such a range of angles to the normal and yet be received by the other optical element. Along with the measured response of the device as a function of gap size between the end of the transmitting fibre and the glass flat, the size of the gap has been calculated from equation 3.1. The theoretical transmission over a range of gap sizes gives a smooth curve same as the experimental results.

Broad agreement is observed as shown in Figure 3.9 e.g. 75 per cent transmission occurs at a gap width of 0.09μm (0.125μ m calculated) and 50 per cent transmission occurs at a gap width of 0.13μm (0.19μm calculated).

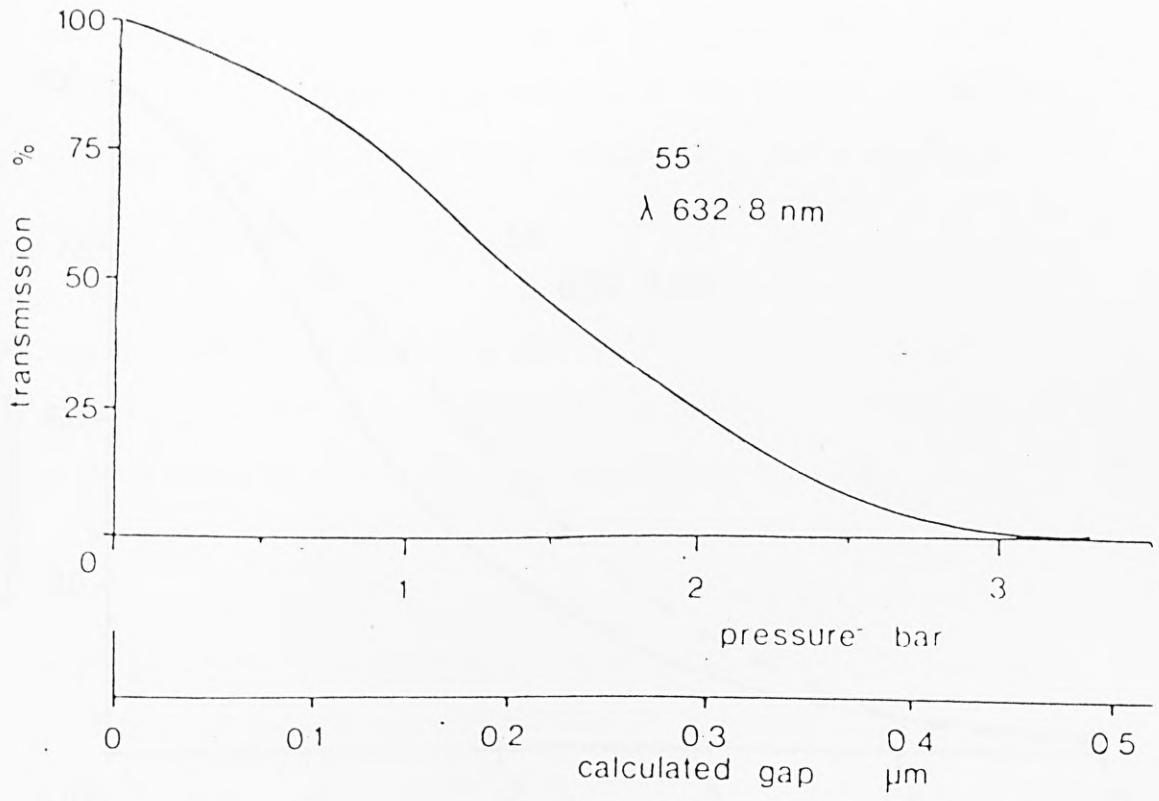

Fig 3.8 Characteristic response of the device at λ = 632.8nm and $\theta = 55^{o}$

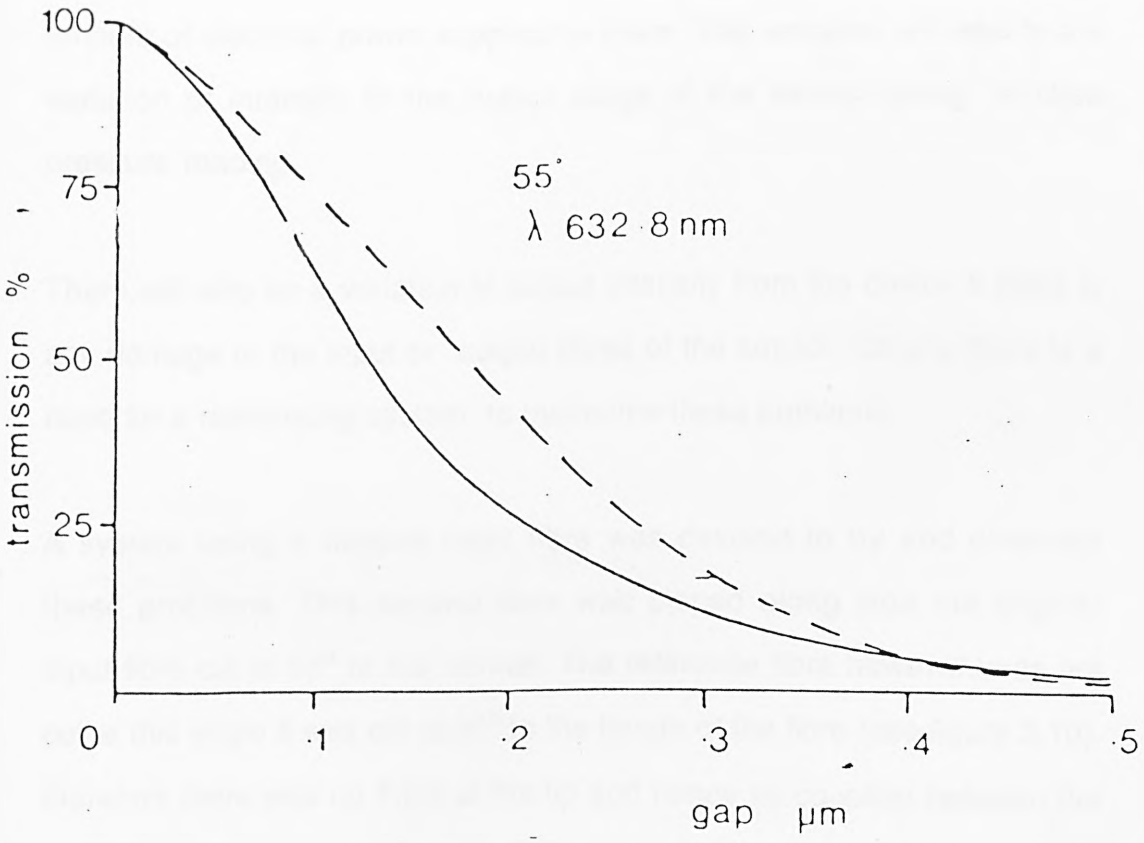

Fig 3.9 Shows the calculated in comparison with experimental response of the device (solid line calculated response, dashed line measured response)

3.4 Referencing of the output modulated signal with the input

As this is an analogue pressure sensor there is a need for referencing of the output to the input light intensity. This is because all light sources have a variation in their output with time and in many cases vary with the amount of electrical power supplied to them. This variation will lead to the variation of intensity in the output stage of the sensor giving a false pressure reading.

There will also be a variation in output intensity from the device if there is any damage to the input or output fibres of the sensor. Clearly there is a need for a referencing system to overcome these problems.

A system using a second input fibre was devised to try and eliminate these problems. This second fibre was placed along side the original input fibre cut at 55° to the normal. The reference fibre however, was not cut at this angle it was cut at 90° to the length of the fibre (see figure 3.10), therefore there was no T.I.R at the tip and hence no coupling between the reference fibre and second optical element through the evanescent wave.

There will, however, be some light coupled into the second optical element from this fibre but its intensity does not vary as a function of the gap between the input fibre and the output optical element (as the gap will only change by ~1μm) at a constant temperature. The light intensity and its variations observed in the output optical element with a varying temperatures are shown in figure 3.11, which shows the inensity to be

constant over a small temperature range but there is a variation over large temperature changes. In this way any changes to the optical input due to damage to the output elements can be monitored at a constant temperature. Since changes to the light source can be monitored at source, this system can lead to a reduction in the referencing problems.

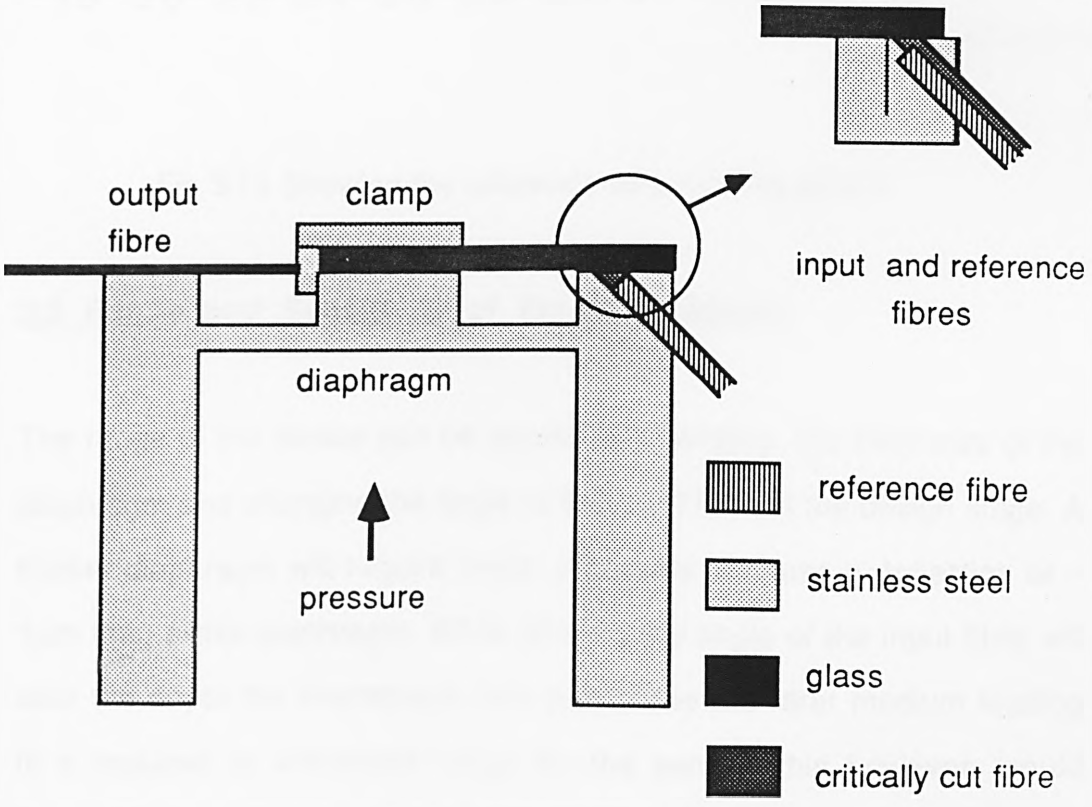

Fig 3.10 Showing the sensor with a reference fibre attached

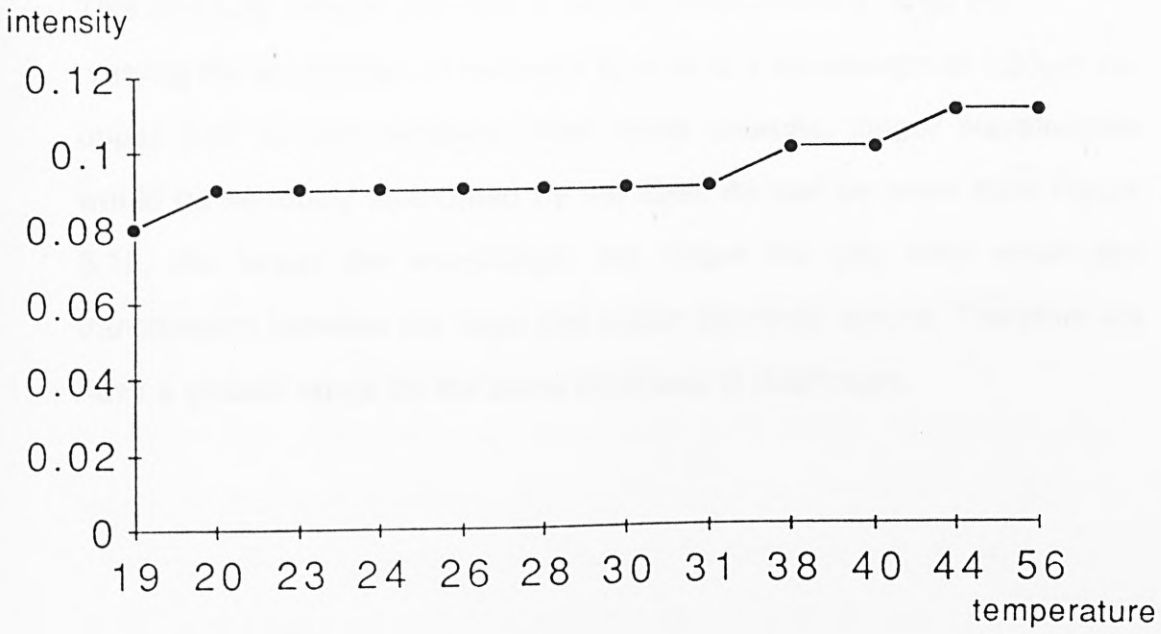

Fig 3.11 Showing the reference output of the sensor

3.5 Range and Sensitivity of Pressure Sensor

The range of the device can be altered by changing the thickness of the diaphragm and changing the angle of the input fibre at the design stage. A thicker diaphragm will require larger pressures to cause a deflection of ~ 1μm than a thin diaphragm. While altering the angle of the input fibre will alter the depth the evanescent field penetrates the rarer medium leading to a reduced or enhanced range for the sensor, this however, would limited as the angles that can be used for the input fibre are also limited. Although these methods of changing the range can work satisfactorily, they are not convenient to use while the sensor is in operation.

This pressure sensor can have a varying measurement range by varying the wavelength of the input light up to a wavelength of 1.55μm the upper limit for conveinenent laser diode sources, longer wavelengths would be seriously attenuated by the fibre. As can be seen from Figure 3.12, the larger the wavelength the larger the gap over which the transmission between the input and output elements occurs. Therefore we have a greater range for the same thickness of diaphragm.

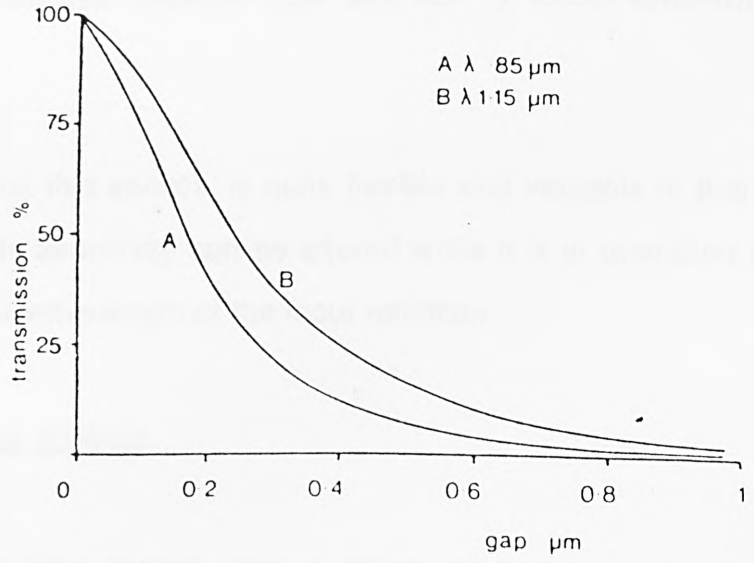

Fig 3.12 Calculated response of the sensor (A) λ = 850nm, (B) λ = 1.15nm

$\theta = 55^{o}$

The sensitivity of the sensor can also be enhanced or reduced by altering

the wavelength of the input light. In this case the shorter the wavelength the greater the sensitivity. From Figure 3.12 it can be seen that the shorter the wavelength, the bigger the percentage change in transmission for a small change in gap width.

An improved sensitivity of the device can also be achieved by altering the angle of the input fibre. It can be seen in Figure 3.7 that as the angle of the input fibre increases, the percentage change in the transmission across the gap also increases sharply. Figure 3.12 illustrates this effect for a sensor which has an input wavelength d = 850 nm and an input angle of 75° (averaged between 65° and 85°). Good sensitivity can be achieved.

It is clear that this sensor is quite flexible and versatile in that both it's range and its sensitivity can be altered while it is in operation by simply changing the wavelength of the input radiation.

3.6 Thermal Effects

This sensor was tested over a range of temperatures from room temperature to a maximum of 70° C. At this maximum temperature it was found that the basic characteristic shape (Figure 3.7) was virtually unchanged, however, the maximum transmitted light intensity was greatly reduced. Figure 3.13 shows the response of the device over a range of temperatures, as can be seen the overall transmission of light across the gap decreases with increasing temperature.

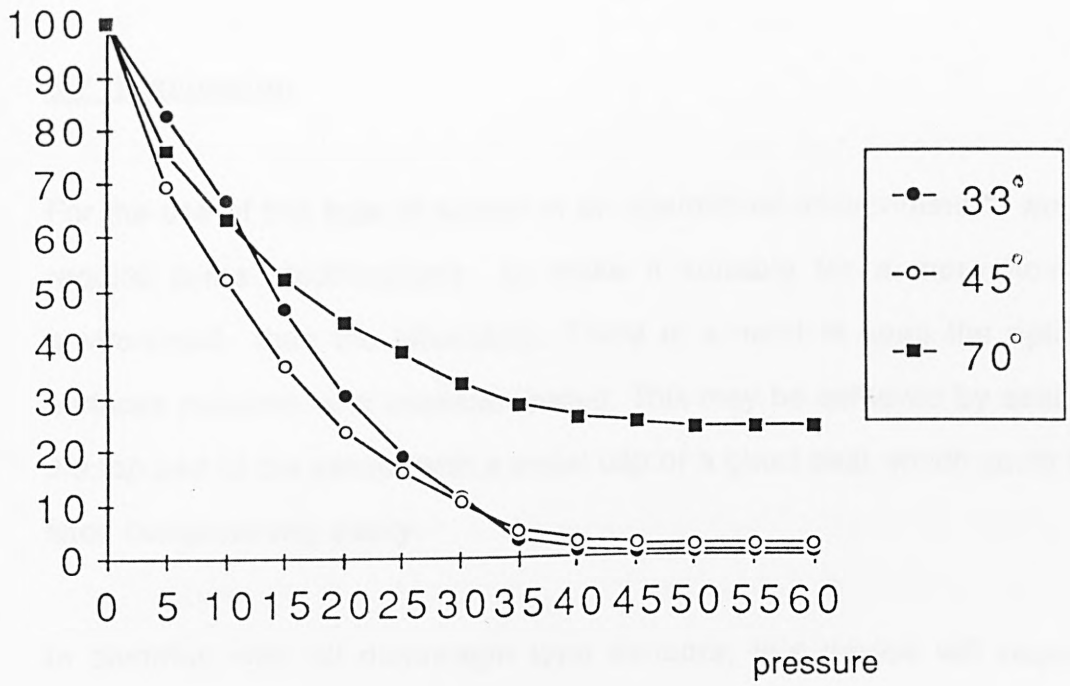

Fig 3.13 Characteristic response of the sensor over a range of temperatures

The decrease in transmission was partially due to the misalignment of the light input to the transmitting fibre in the hot environment and partially due to slight distortion of the device. There was also a change in the coupling between the input fibre and the second optical element due to the differential expansion between the input fibre and the stainless steel

body.

The device again showed negligible hysteresis while the temperature remained constant, but had a large thermal hysteresis.

3.7 Discussion

For the use of this type of sensor in an operational environment, it would require some modifications to make it suitable for a more hostile environment than the laboratory. There is a need to keep the optical surfaces polished and uncontaminated. This may be achieved by sealing the top part of the sensor with a metal cap or a glass seal, which could be fitted comparatively easily.

In common with all diaphragm type sensors, this device will require precalibration stress relief treatment to prevent any problems arising from the change in the gap width of the optical element with time.

The effects of environmental temperature changes upon the readings obtained from this device (section 3.6) means that this device is more suitable as an optical hydrophone, where temperature changes are minimal. This sensor could be used in other environments as long as the environmental temperature is known. If this were the case the sensor could be used with confidence, since the calibration curves for various temperatures can easily be stored in the memory of a microprocessor.
The thermal effects could be reduced by the use of more thermally

matched materials, as stainless steel has a large thermal expansion coefficient. The steel could be replaced by materials of lower expansion coefficients such as Invar which has an expansion coefficient similar to that of glass. steel was used as it is easily avilable and is relatively simpler to use and above all its of much lower cost than Invar.

In its present use, as described, the sensor is addressed by light from a He-Ne laser. This provides an intense light source and the geometrical coupling losses from the glass flat to the receiving fibre, although quite large (due to a small overlap area) do so far prove a limitation in use. In practice, however, to increase the recorded signal level for higher sensitivity, the end of the glass plate can be tapered gradually to an aperture comparable with the diameter of the receiving fibre. No problems were encountered due to modal noise generated in the multimode fibre by the laser and the overall signal to noise levels were more than adequate for sensing to the accuracy indicated.

For industrial use the laser source could easily be replaced by a bright incoherent source such as a GaAlAS light emitting diode, now available at low cost.

It is quite clear that the use of F.T.I.R can lead to a highly sensitive and versatile pressure sensor. It has some limitations, which for the most part can be eliminated. But this makes the device more complicated and hence more expensive to manufacture and run. There still remains the problem of intensity referencing (although it may be soluble in the

manner described). It would be more desirable if a device could be designed that was free from this problem, i.e. it would be more convenient to make a device that was digital in nature rather than analogue.

Chapter 4

Hybrid (Optical - Electrical) Digital Force (Pressure) Transducer

Abstract

An optically driven, through phtovoltaic conversion, pressure sensor is described which uses frustrated total internal reflection between a critically cut fibre and quartz crystal, mounted on a cantilever beam to sense the device resonant frequecy. The change in this frequency as a function of applied pressure is measured in this sensor which relies on an all optical link to the control electronics.

4.1 Introduction

The development of digital sensors has resulted from the widespread use and continuing progress in digital techniques in control systems and information processing and transmission. With the availability of digital electronic techniques at reasonable prices, the acceptability of optical sensors will be enhanced and their other advantages more appreciated if a digital output from the transducer can be obtained. In addition, the other standard criteria of acceptability in terms of reliability, simplicity, size and weight must be met. A conventional sensor e.g. a Bourdon tube or even a simple optical device [48] can have digital outputs , where an analogue signal produced can be digitised but in many cases this degrades the performance and decreases reliability.

By contrast, elements which are inherently digital are preferable e.g. strings or tapes, cylinders, diaphragms or electronic oscillator devices. Conventional resonant circuit devices which suffer from poor repeatability and hysteresis due to the large deflections induced and vibrating strings etc are usually able to measure only absolute pressures since one side of the instrument needs to be evacuated and sealed for reference. As strings cannot be compressed, they must be held in tension in use and high loads can cause creep with a resultant instability.

An important parameter in the assessment of these devices is the "Q factor" (quality factor). This is proportional to the ratio of energy stored to energy lost per cycle in a vibrating system, where losses from all sources,

internal or external are considered. A high Q will reflect itself in the accuracy of the device and its susceptibility to external influence as the higher the Q factor, the lower the energy required to make up for the energy dissipated in each cycle. Q is also defined as

$$Q = f_o/\Delta f \qquad \text{.....(4.1)}$$

where f_o = resonant frequency

Δf = bandwidth of resonance at 3db points.

This implies that the sharpness of the resonance and immunity to external vibration near resonance are proportional to Q. Therefore it can be seen that analogue to digital conversion devices are of inherently low Q and low frequency stability. In this work a quartz resonant element is used to provide both a high Q device and good optical properties.

4.2 The Quartz Resonator

The piezoelectric quartz resonator has been used as a frequency standard for many years and the resonant frequency selectivity to strain in quartz oscillators has been widely utilized in the development of face sensors [49]. These sensors work on the principle that a beam in flexural vibration will change its resonant frequency as stress is applied to it, in the same way that the resonant frequency of a vibrating string is a function of

the applied tension. As these sensors are made from a piezoelectric material they can be used as a circuit element, simply by attaching appropriate connections, and maintained in oscillation electrically. Quartz is one of several extremely stable crystals which exhibit such piezoelectric properties and is advantageous to use not only because of its stability, but because of the predictability of the changes in frequency with loading, and the large background of information available from the use of such devices in the electronics industry.

Quartz is an anisotropic crystalline material which allows its characteristics to be varied as a function of its cut. (A full description of the piezoelectric properties of quartz can be found in appendix C). An 'AT' cut quartz crystal was chosen for this transducer.

An AT cut is a Y cut that has been rotated about the x axis by 35° (Figure 4.1). As with a Y cut the AT cut exhibits a body shear deformation when a field is set up across its thickness (Figure 4.2a). With an electric field impressed across the crystal, the rectangular beam assumes the shape of a parallelogram, distorting as shown (Figure 4.2b). This distortion depends upon the polarity of the field. Therefore if there are two sets of electrodes on a rectangular quartz beam with opposing polarities, the section of the beam within the electrodes will distort in opposing directions, hence causing a flexture (Figure 4.2c). If the polarities of the voltages upon the electrodes are alternated at the resonance frequency of the beam, the beam will resonate in the flexural mode.

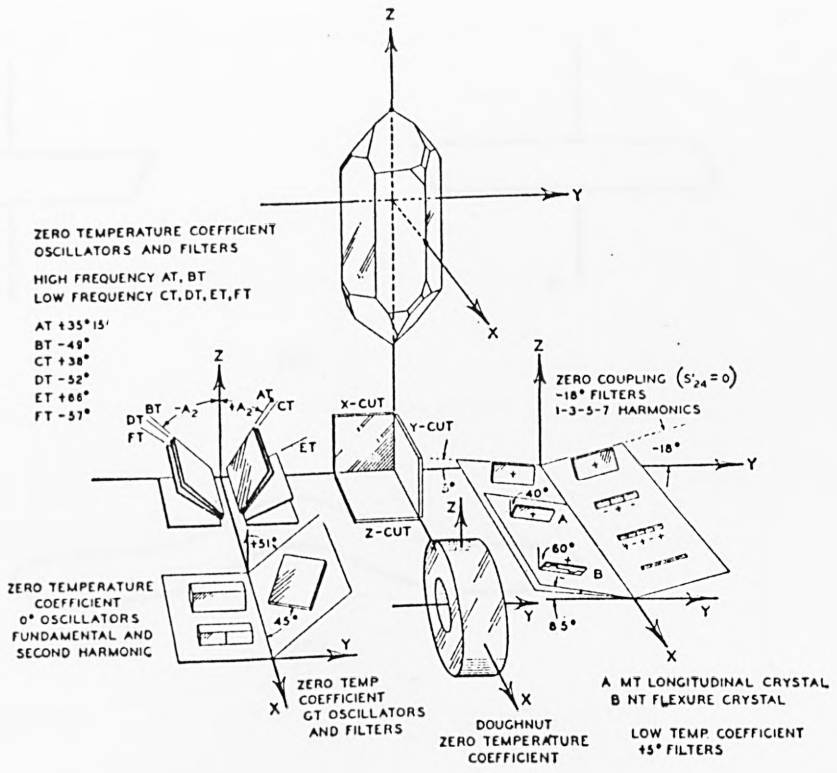

Fig 4.1 Showing an AT cut in quartz crystal [61]

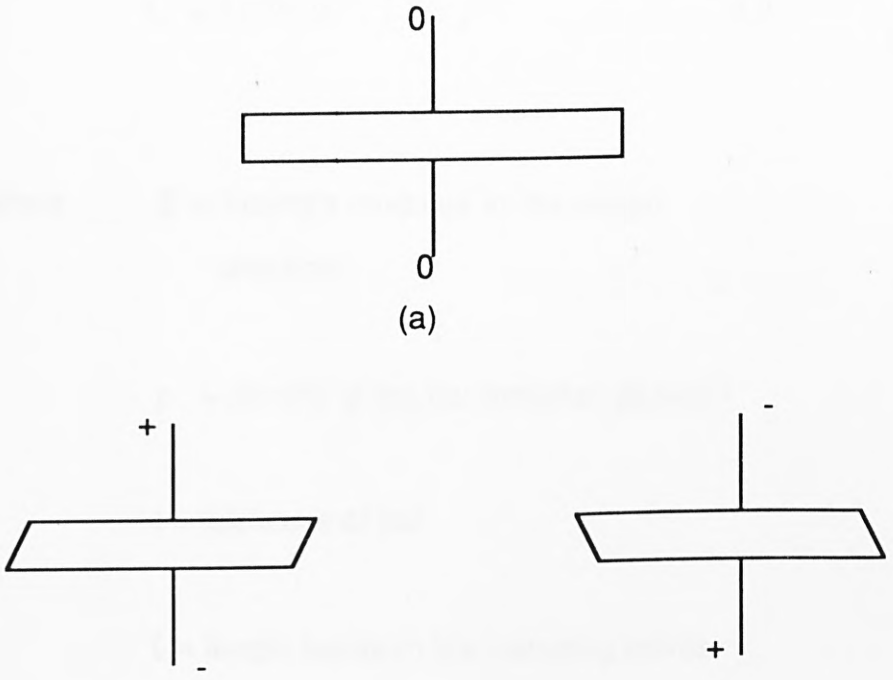

Fig 4.2 Distortion of Quartz due to an electric field

The fundamental flexural resonance frequency of a rectangular bar clamped at both ends (Figure 4.3) is given by [50]

$$f_o = 1.028\,(t/\ell^2)\,(E/\rho)^{1/2} \quad \text{.....4.2}$$

where E = Young's modulus in the length direction

ρ = density of the bar material (quartz)

t = thickness of bar

ℓ = length between the clamping points.

A beam in flexural vibration will change its resonant frequency if a stress is applied to it, in the same manner as the resonant frequency of a vibrating string is a function of the applied tension.

Fig 4.3 Rectangular bar clamped at both ends.

So when a tensile stress, σ, is applied along the length of the beam, there is a shift in the fundamental frequency. This shift is given by [50]

$$(f_o')^2 = (f_o)^2 + \sigma / r L^2 \quad \text{.....(4.3)}$$

where:

f_o' = the new frequency of the crystal.

$L = (4/3)\,l$

substituting for L gives

$$(f_o')^2 = (f_o)^2 + (9/16)\,(f_o/1.028)[\sigma/t\,(E/\rho)^{1/2}] \quad \text{.....(4.4)}$$

If the first terms only are considered this gives small load sensitivity, defined as the fractional change in frequency per unit stress

$$(1/f_o)\,(df_o'/d\sigma) = 0.266\, l^2/Et^2 \quad \text{.....(4.5)}$$

The sensitivity is therefore mainly dependent on the square of the aspect ratio of the beam l^2/t^2 . This factor is chosen to give a reasonably large frequency change when maximum load is applied. The maximum is limited by the breaking strain of the quartz and by the clamping arrangements.

4.2.1 Crystal Resonator Structure & Mounting

A vibrating beam in axial tension and compression provides a simple and a direct technique for force to frequency conversion. A rigid beam conventionally mounted however, has serious drawbacks in sensitivity to end moments and mounting point energy losses. This sensitivity can be greatly reduced by the use of a pair of beams in a symmetrical tuning fork configuration (Figure 4.4).

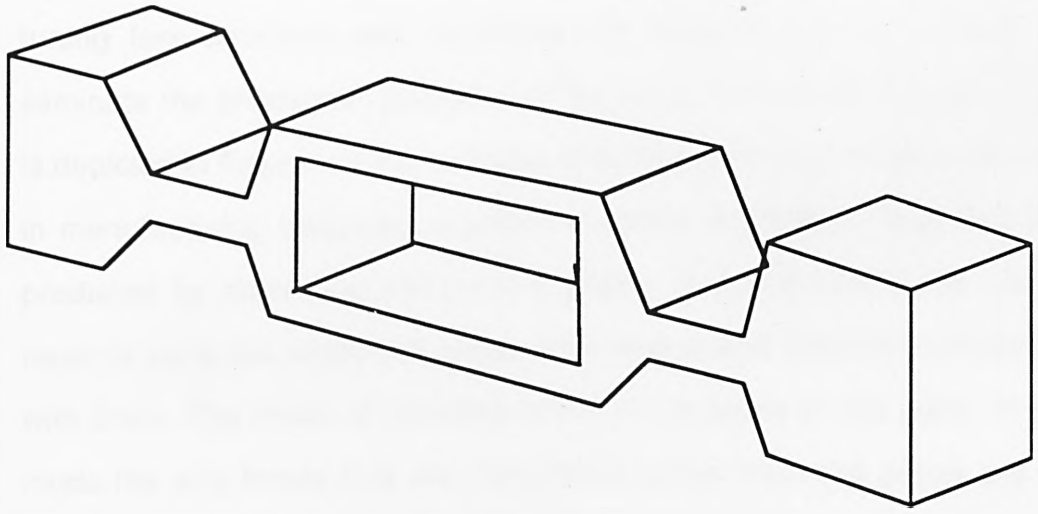

Fig 4.4 Showing a quartz tuning fork structure as used by Litton Systems Inc

This virtually eliminates the transmission of kinetic energy to the mounting points. The symmetrical structure and construction allows the parallel beams to vibrate in symmetry, so that the moments due to bending at the

dual beam junctions are cancelled out. A high degree of mechanical isolation between the active portion of the resonator and the mounting points is provided by the integral end supports.

This type of resonator structure has been successfully used by Litton Systems Inc.[51] in the all electrical force transducer. Although the structure works well, it is very difficult to produce in large quantities, and is difficult to miniaturize. The complex nature of this structure would inevitably make the production of the crystals expensive. Another type of tuning fork structure was developed by Marconi [50] in an effort to eliminate the production problems of the Litton tuning fork. This structure is depicted in Figure 4.5 and consists of a flat quartz plate of the type used in manufacturing frequency standard crystals. A double tuning fork was produced by machining slots into a plate . In this structure the central beam is twice the width with of the outer beams and vibrates in antiphase with them. The mode of vibration is out of the plane of the plate. In this mode the only forces that are transmitted to the mounting points are the bending moments about the central axis of the structure. Therefore the vibration is only marginally affected by the position of the mounting through which force is applied.

The fundamental flexural resonance frequency of this double tuning fork structure, in which the central beam vibrates in opposition to the two outside beams, is lower than that predicted by equation 4.2. This is because the beams are not clamped at the points where they are joined. Therefore there is bending beyond the length of the beam within the

actual body of the quartz plate. This implies that the length of the active beam is greater than it otherwise could be and hence a lower fundamental frequency results.

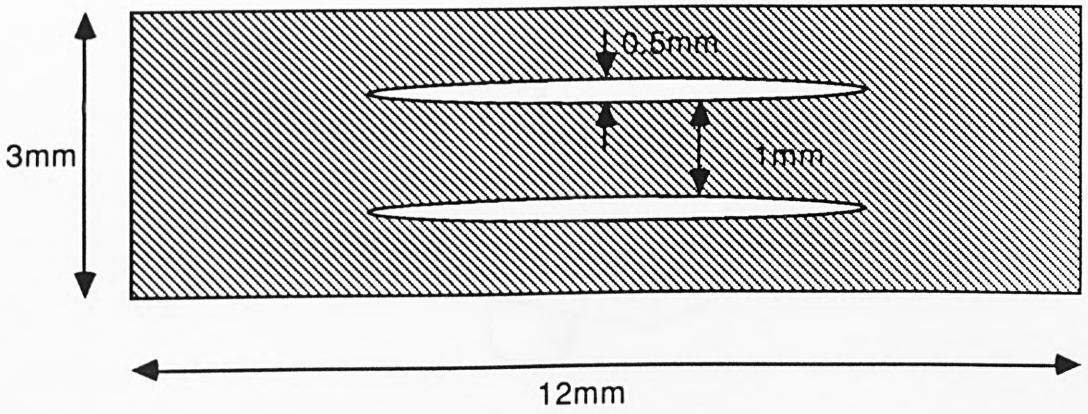

Fig 4.5 The Marconi double tuning fork

4.2.2 Fabrication of Quartz Resonator

The quartz resonators were produced from AT cut blanks, cut from a single large quartz crystal. To produce AT cut blanks, the crystallographic axes of the crystal have to be identified. The orientations of the quartz crystal axes were determined by the use of X-ray diffraction, in particular the use of the Back Reflection Laue camera. As shown in Figure 4.6, the X-ray beam passes through a hole in the photographic plate before striking the crystal. The beam of X-rays is collimated by the use of a series of pin holes on either side of the photographic plate. Spot reflection from the various planes within the quartz fall on the film and leaves a series of spots upon it. These spots correspond to a different value of, λ, from the

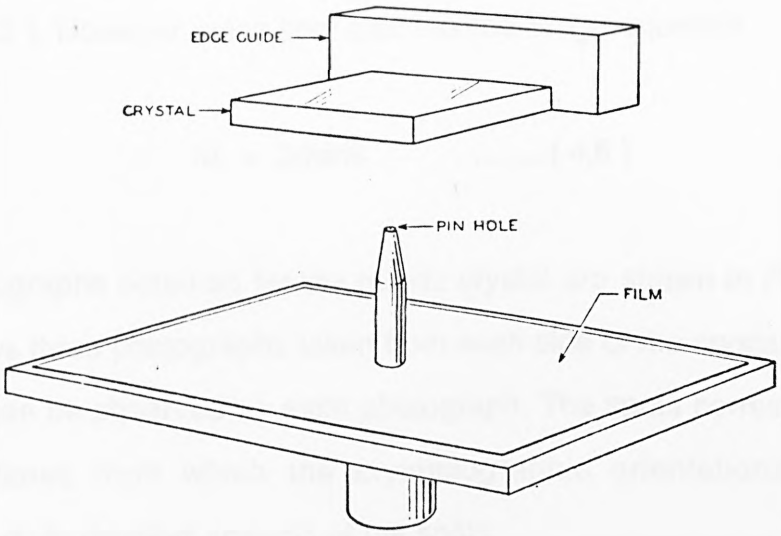

Fig 4.6 Schematic of a Laue camera

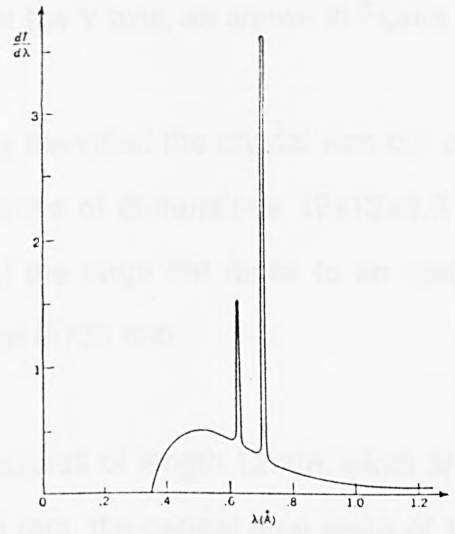

Fig 4.7 X-ray spectrum used

continuous background as opposed to the peaks in the X-ray spectrum (Figure 4.7). However, each spot satisfies the Bragg equation

$$n\lambda = 2d\sin\theta \qquad \text{.....(4.6)}$$

The photographs obtained for the quartz crystal are shown in Figure 4.8. This shows three photographs taken from each side of the crystal. A series of spots can be observed on each photograph. The spots correspond to a set of planes from which the crystallographic orientations can be determined via detailed analysis of the spots.

However, since quartz has a symmetry class of 32m (figure 4.9), the X,Y,Z direction of the quartz were easily determined by identifying two fold symmetry corresponding to the X axis, three fold symmetry for the Z axis and no symmetry for the Y axis, as shown in Figure 4.8.

Once the axes were identified the crystal was cut using a diamond saw to produce AT cut blanks of dimensions 12x12x0.3 mm, which were then polished on both of the large flat faces to an optical finish and had an eventual thickness of 0.125 mm.

The tuning fork structures of length 12mm, width 3mm, with slots of length 6mm, and width 0.5 mm, the central tyne width of 1mm and outer tynes of width 0.5mm, as shown in Figure 4.10 were produced by the technique of air abrasion. A jet of air containing Aluminum oxide particles of diameter $\approx 28\mu m$ is brought to bear upon the crystal. The oxide particles erode the

crystal to produce the necessary slots.

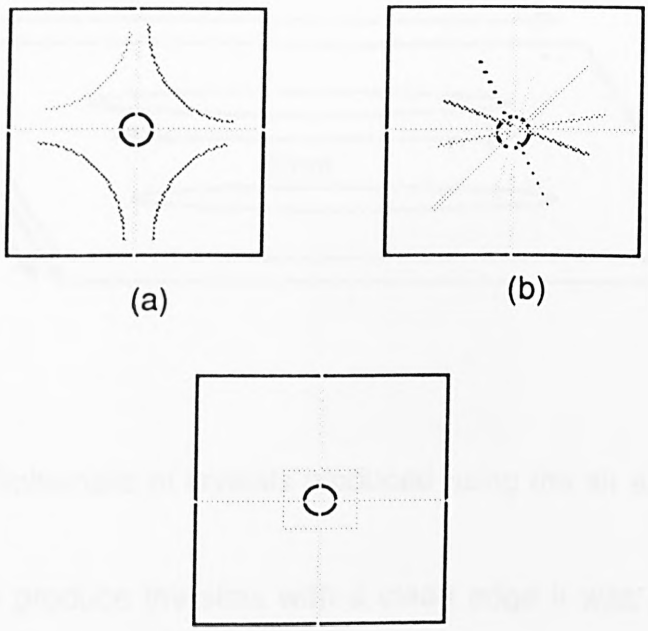

Fig 4.8 Schematic of the Laue photographs obtained for quartz
(a) x-axis (b) y-axis (c) z-axis

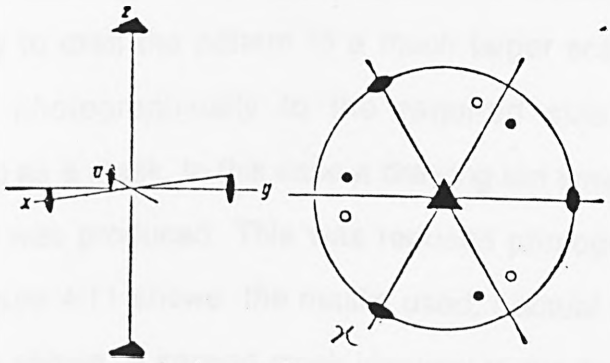

Fig 4.9 Elements of the symmetry class 32m

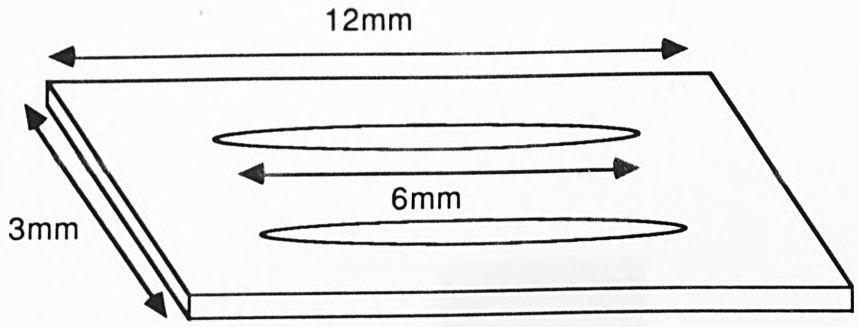

Fig 4.10 Schematic of crystals produced using the air abration technique

In order to produce the slots with a clean edge it was necessary to use metal masks, which were photolithographically produced.

4.2.2.1 Photolithographic Fabrication of Masks

In order to produce a mask with the required dimensions and pattern, it was necessary to draft the pattern to a much larger scale. The drawing was reduced photographically to the required size. The negative produced acted as a mask. In this case a drawing ten times the size of the mask required was produced. This was reduced photographically to the actual size. Figure 4.11 shows the masks used, (actual size) where the dimensions are shown. A second mask identical to the first was produced so that a copper mask could be etched from both sides. Using this mask the crystal could be produced from a quartz "blank" of dimensions 12mm x 17mm x 0.125mm.

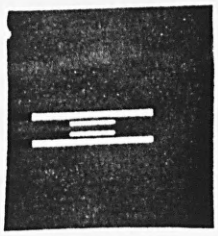

Fig 4.11 Photolithographic mask used to produce copper masks for etching

Beryllium Copper was used as the metal mask, with pieces of Beryllium Copper of dimensions 17mm x 17mm x 0.125mm being used. These pieces were coated with microposit TF-20 photoresist using a spinner. The spinner was rotated at 4000 R.P.M for 40 seconds to give an even coating on the Copper. Both sides of the copper were coated. The coated piece was then soft baked at 90°C for 30 minutes. The photographic masks were aligned (Figure 4.12) and the Copper coated with photoresist was inserted between the photomasks.

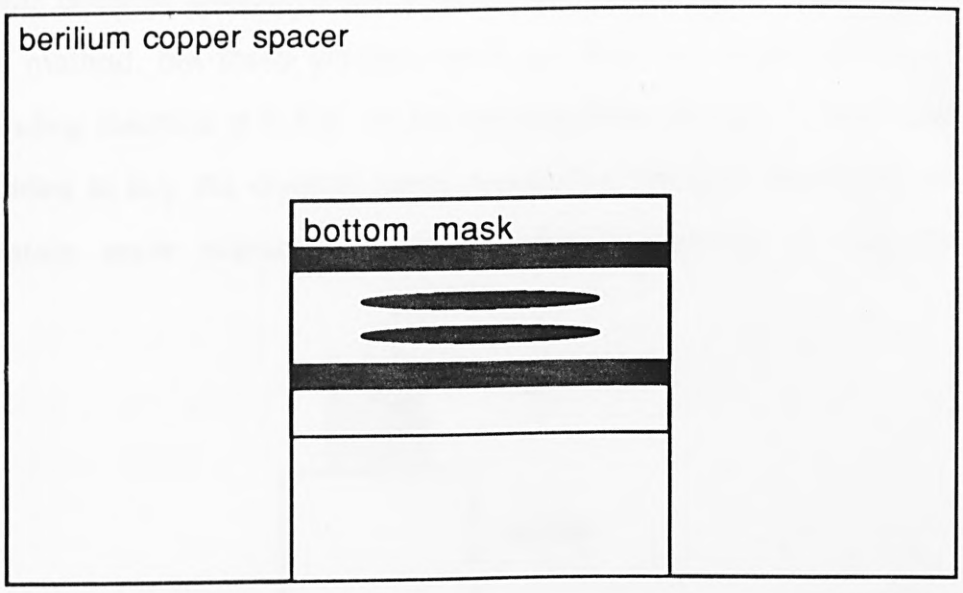

Fig 4.12 Schematic mask alignment showing bottom mask and spacer, another mask is placed on top and aligned using a light table.

A piece of glass was used to press the photomasks on to the copper to give a close contact. The masks were then exposed on both sides by a mercury vapour light source (λ = 365 - 405nm) for 20 minutes. The copper was then removed and developed using microposit 450 developer for 5 minutes, and was then hard baked at 120°C for 30 minutes. Once this process was completed, the copper was dipped into Ferric Chloride for 30 minutes, which attacked and dissolved the uncoated Copper leaving the metal mask. This mask was then attached to the optically polished quartz blanks using a thermosetting resin (lakeside 70). The prepared quartz blanks were then taken to G.E.C. Mechanical Handling where an air abrading machine was used to cut slots into the quartz (Figure 4.13).

It was possible produce a few crystals with the tuning fork structure using this method, but these crystals were not of a very high quality, the air abrading machine of G.E.C not being suitable for this job. Therefore it was decided to buy the crystals ready made from Marconi Research. These crystals were manufactured in a similar manner to the above.

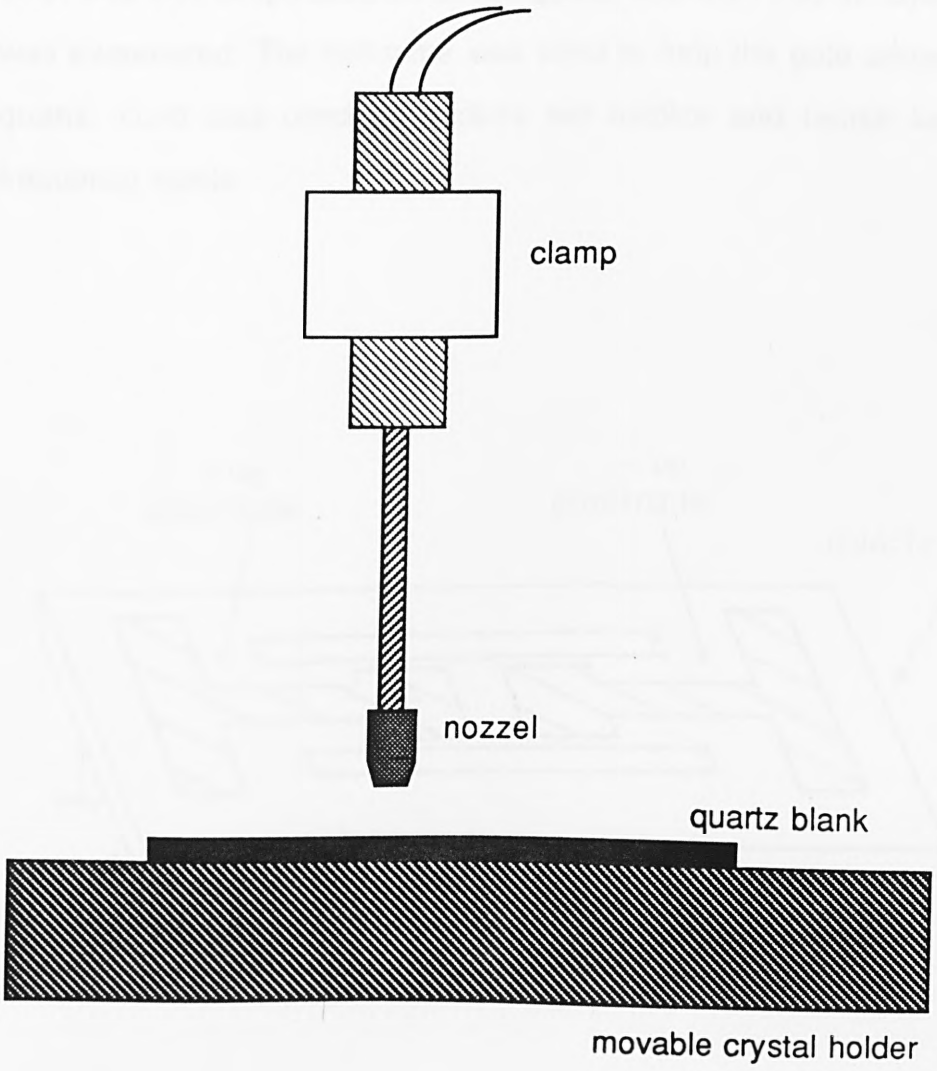

Fig 4.13 Schematic of air abration equipment used.

Once the correct crystals were obtained a set of electrodes were evaporated upon them. The electrical pattern used is shown in Figure 4.14. This pattern was produced using a copper mask which was manufactured using the above photolithographic technique. The electrodes were a gold nichrome sandwich. A layer of nichrome 10nm thick was first evaporated on to the quartz and then 100nm layer of gold was evaporated. The nichrome was used to help the gold adhere to the quartz. Gold was used as it does not oxidize and hence keeps the frequency stable.

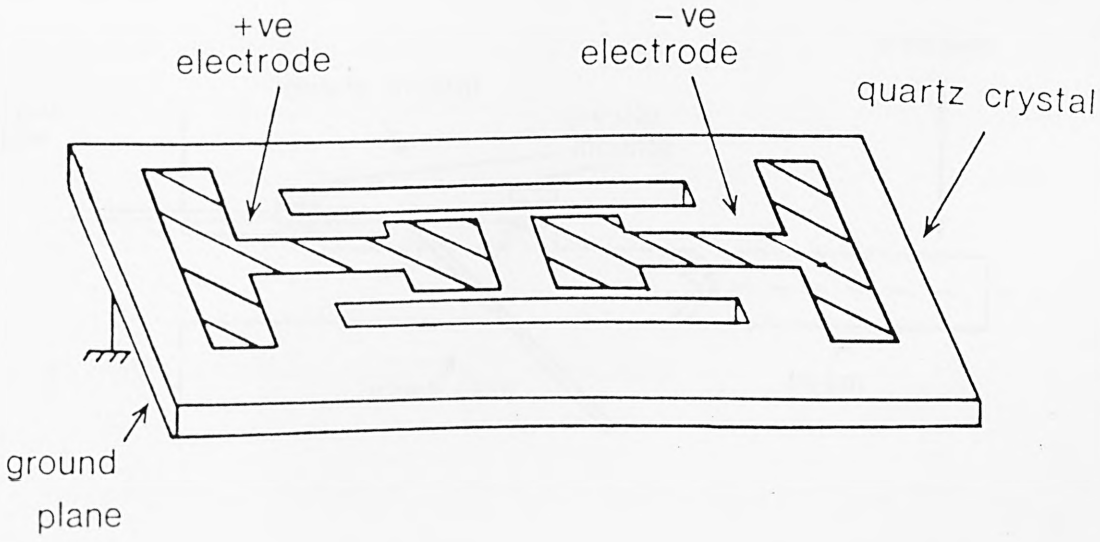

Fig 4.14 Shows electrode pattern used to drive the crystal

4.3 Transducer Design

The system used to provide a stain across the crystal was a simple cantilever beam. The crystal was mounted on one end of the cantilever beam, and held via mounting clamps. These clamps were placed on the ends of the crystal corresponding to the stationary points upon the crystal. The force to be measured could easily be applied to the beam to produce a resultant stress in the crystal, hence shifting its resonant frequency. This is illustrated schematically in Figure 4.15.

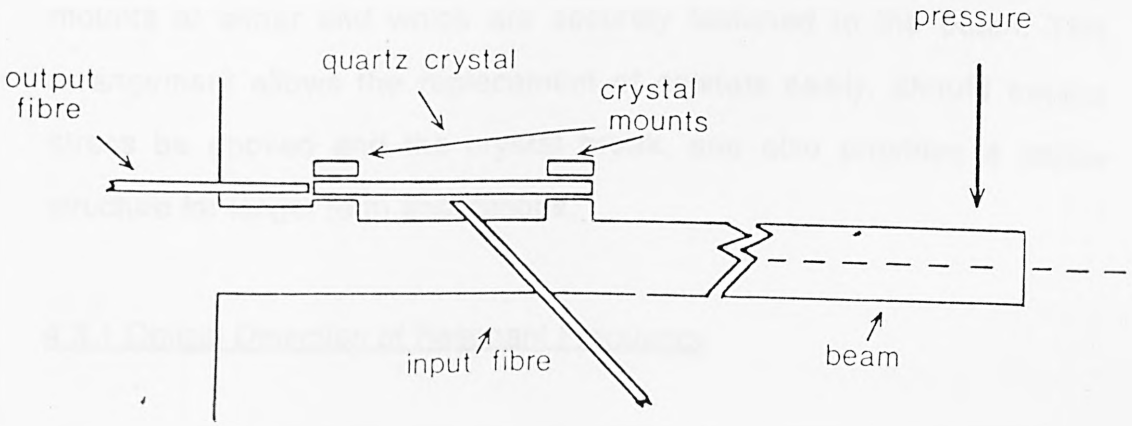

Fig 4.15 Schematic of transducer design

When a force F is applied to the rectangular cantilever beam, the strain, γ, produced on the surface is given by [50] :

$$\gamma = 12bFa/E'gt'^3 \quad \text{.....(4.7)}$$

where E' is the Young's modulus for the beam along its length, a is the distance from the point where the force is applied to the crystal, g and t', are the breadth and thickness of the beam respectively and b is the displacement in the Y direction. The average strain is assumed to be midway between the points of attachment.

The crystal is held in contact with the cantilever beam with two detachable mounts at either end which are securely fastened to the beam. This arrangement allows the replacement of crystals easily, should excess stress be applied and the crystal break, and also provides a stable structure for longer term applications.

4.3.1 Optical Detection of Resonant Frequency

The resonance frequency of the crystal is determined using the F.T.I.R or evanescent wave coupling between a critically cut optical fibre placed underneath the crystal and a second fibre in contact with the stationary part of the crystal, as shown in Figure 4.15. The fibres used were 600μm diameter plastic clad silica type of numerical aperture (NA) equal to 0.4.

The critically cut fibre was brought up to the crystal, through a mounting hole drilled into the cantilever at 55° to the normal. The fibre was housed in a stainless steel tube and the whole assembly was held via epoxy resin. The protruding surfaces of the beam and fibre were polished to give an optically flat mirror finish. This ensured that the mounting posts and the fibre were at the same height above the beam.

Since the crystal vibrates flexurally, it is necessary to create a gap between the fibre and the crystal to allow the central tyne to move more freely. This gap was created by evaporating a thin film of around 200nm on the underside of the crystal. A small gap was left in the film to allow optical coupling between the fibre and the crystal. As can be seen from Figure 4.16, the coupling between the film and crystal varies with distance. So when the crystal vibrates the coupling varies i.e. when the crystal moves down the coupling increases and when it moves up it decreases, hence producing a modulation of the C.W. (continus wave) input equal to that of the frequency of the crystal.

A small channel was cut into the cantilever beam to accommodate the output fibre, of similar type to the input fibre. This fibre was polished at right angles to the fibre axis and was held in contact with the end of the crystal. Hence any light coupled into the crystal was channelled back to the detector.

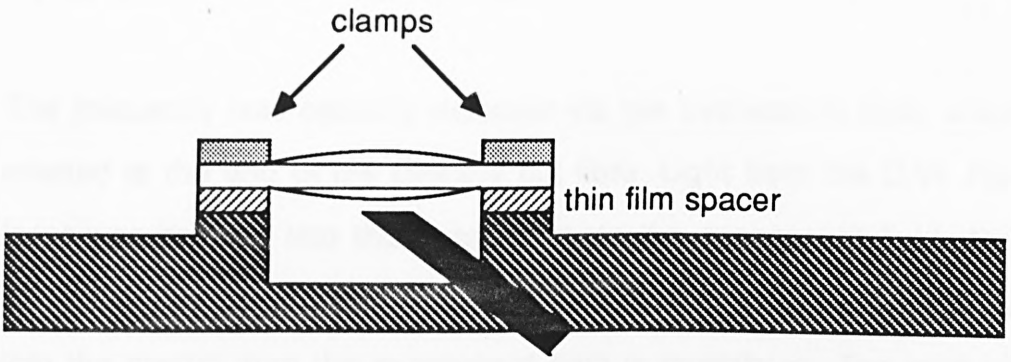

Fig 4.16 Showing crystal mounted on cantileaver beam with thin film spacer (not to scale)

4.3.2. The Electronic System

The electronic control and drive system is illustrated in Figure 4.17. At the heart of the system is a phase locked loop (PLL). The voltage controlled oscillator within the PLL was set to oscillate at the crystal resonant frequency. The output from the PLL drove a GaAlAs LED (Honeywell type SE 3352 - 004) which has an optical output at a wavelength of 820nm. The LED was modulated at the resonance frequency of the crystal which launched ~ 1mW of optical power into the fibre. Light from this LED was coupled to the sensor head via a length of 600µm diameter PCS optical fibre where it was detected by a silicon photodiode where the photovoltaic conversion of the optical signal occurred. The voltage produced (0.60V) is transformed via a miniature transformer (winding ratio 1 : 6.45) to a

voltage of ~ 4 volts. The a.c. signal is applied to the electrodes upon the crystal to drive it at its resonant frequency.

The frequency was optically detected via the evanescent field, which is created at the end of the critically cut fibre. Light from the C.W. He-Ne laser was coupled into this fibre to create the evanescent field. As the crystal moved up and down at the resonant frequency the coupled light into the crystal from the evanescent field is modulated. The modulated signal was coupled into the output fibre and channelled to a silicon detector. The signal from this was fed into a band pass filter of centre frequency at approximately 13 kHz (3db point at +/- 2kHz) to remove the high and low frequency noise. The signal was then fed to a phase locked loop type 565. The signal was compared with the VCO (voltage controlled oscillator) within the PLL. If there was a discrepancy between the two signals the PLL altered the frequency of the VCO to match that of the input to the PLL. Therefore when a force was applied to the cantilever the frequency of the crystal will change. The change was detected and the PLL changed the frequency of the VCO to match, hence the oscillations were maintained. (For full circuit diagram see Appendix D).

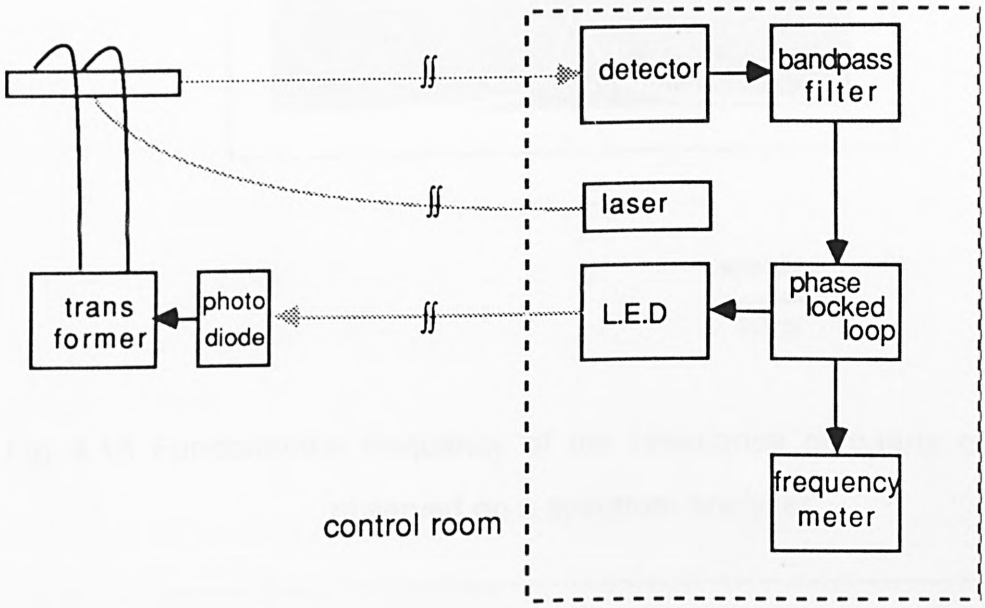

Fig 4.17 Schematic of circuit and detection system used

4.4 Results

The system was tested at a fixed room temperature of 20° C by applying a series of weights to the cantilever and noting the resonant frequency of the crystal,which way read out on a a standard laboratory frequency meter and spectrum analyser. A trace of the resonant frequency is illustrated in Figure 4.18, as was seen upon the spectrum analyser. The maximum test weight used was 200g (to ensure that crystal fracture did not occur). The calibration graph thus obtained, is shown in Figure 4.19, and as predicted by theory [50] a straight line was observed, with a 4% increase in resonant frequency from zero loading to 200g.

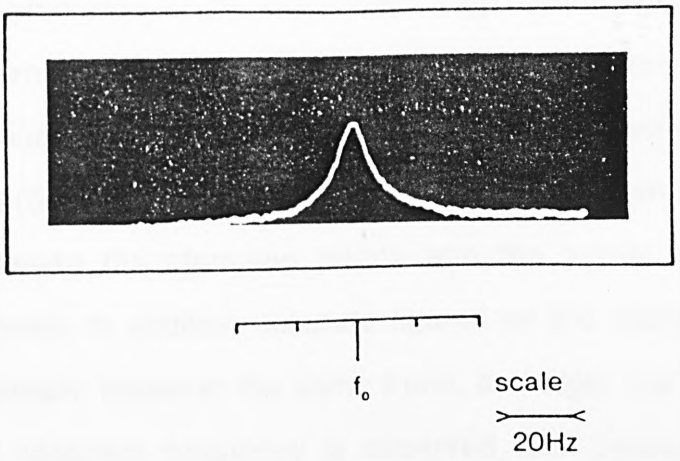

Fig 4.18 Fundamental frequency of the resonance of quartz crystal observed on a spectrum analyzer

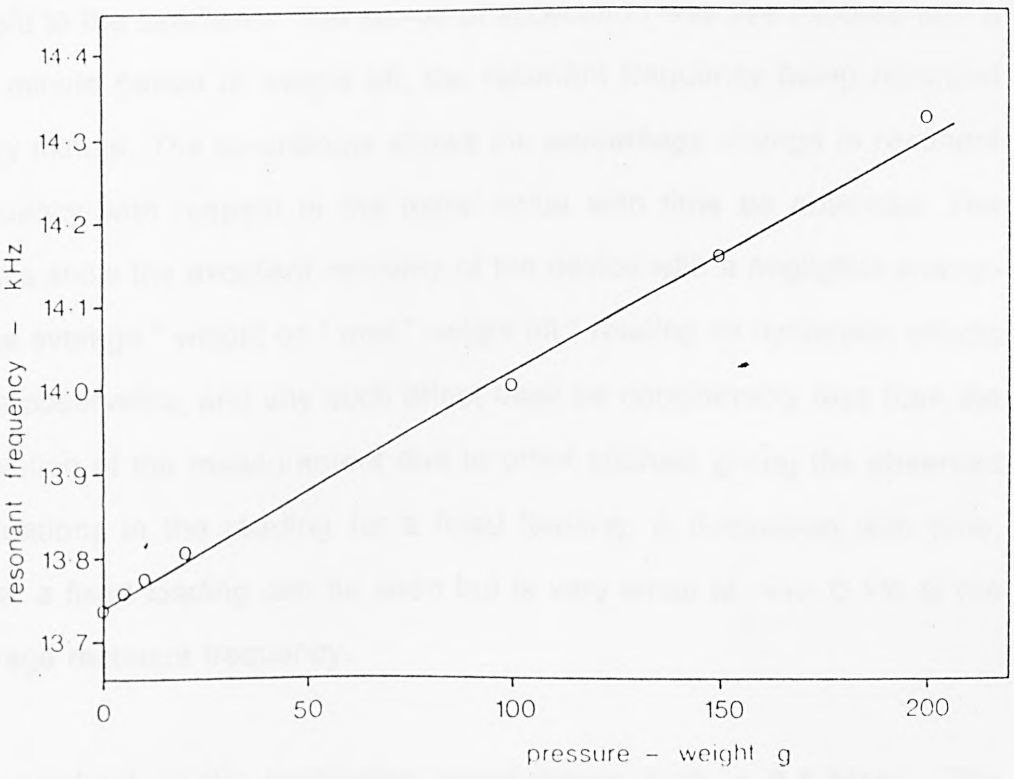

Fig 4.19 Calibration graph of resonant frequency of the crystal as a function of pressure measured as weight applied to beam

The theoretical prediction for the same load range from equations 4.3, 4.4 and 4.7 is shown in Figure 4.20. The observation that there is a deficit between the theoretical and experimental values is in agreement with the work of Kirman (50). This most likely results from the difference between the length between the clamping points and the actual size of the resonating element. In addition accurate figures for the clamping stress are difficult to obtain. However the same trend, a straight line profile with an increase in resonant frequency is observed both theoretically and experimentally.

Figure 4.21 illustrates the effect of the cycle of application and removal of weight to the cantilever. The period of application was five minutes with a five minute period of weight off, the resonant frequency being recorded every minute. The co-ordinate shows the percentage change in resonant frequency with respect to the initial value with time as abscissa. The results show the excellent recovery of the device with a negligible change in the average " weight on " and " weight off " reading no hysteresis effects were observable, and any such effect must be considerably less than the resolution of the measurement due to other sources giving the observed fluctuations in the reading for a fixed loading. A fluctuation with time, under a fixed loading can be seen but is very small at ≈+/- 0.1% of the average resonant frequency.

The gradient of the calibration graph figure 4.19 is 2.8 Hzg^{-1} .The resolution of the device with a 200g weight can be determined to be +/-5g in this work. This is derived from the fluctuations in the frequency recorded

for the weight applied (+ /-0.1% of the frequency i.e. ≈ +/-14 Hz), which from the calibration graph corresponds to +/- 5g.

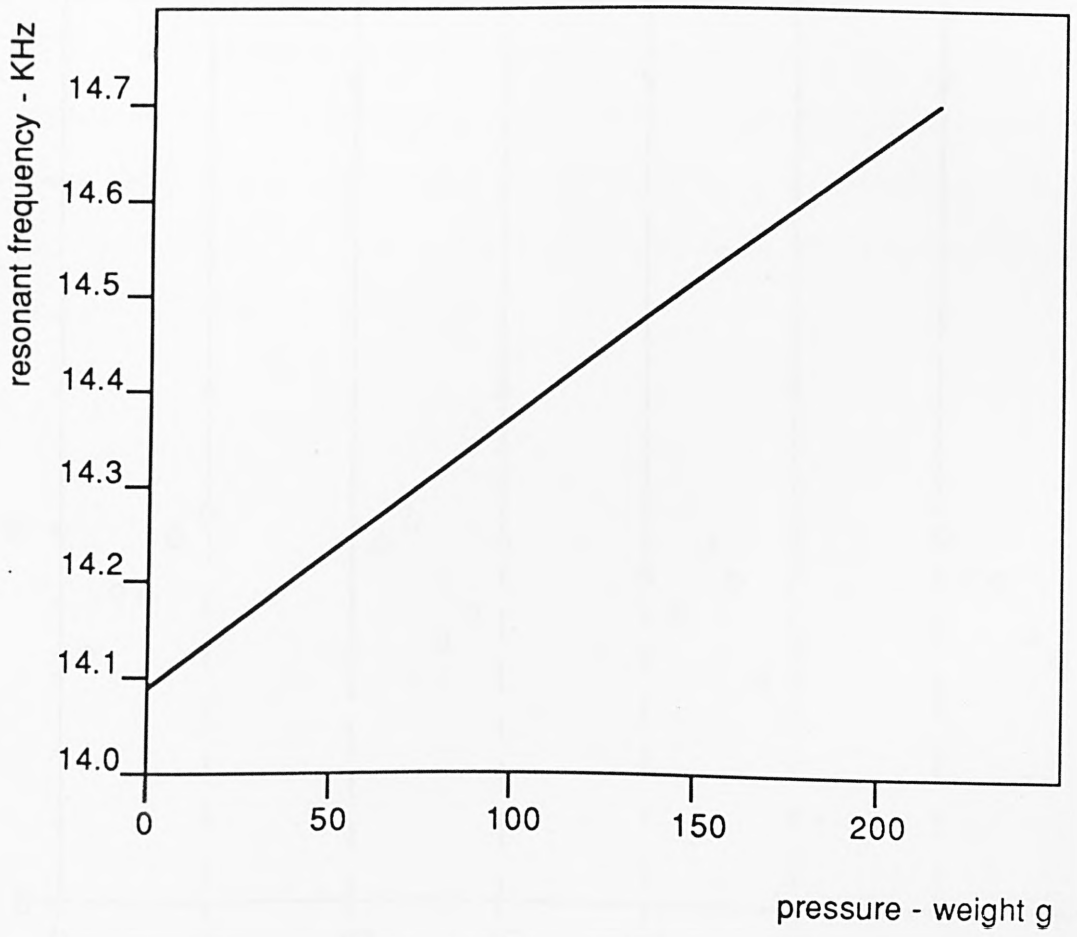

Fig 4.20 Theoretical calibration curve of the sensor

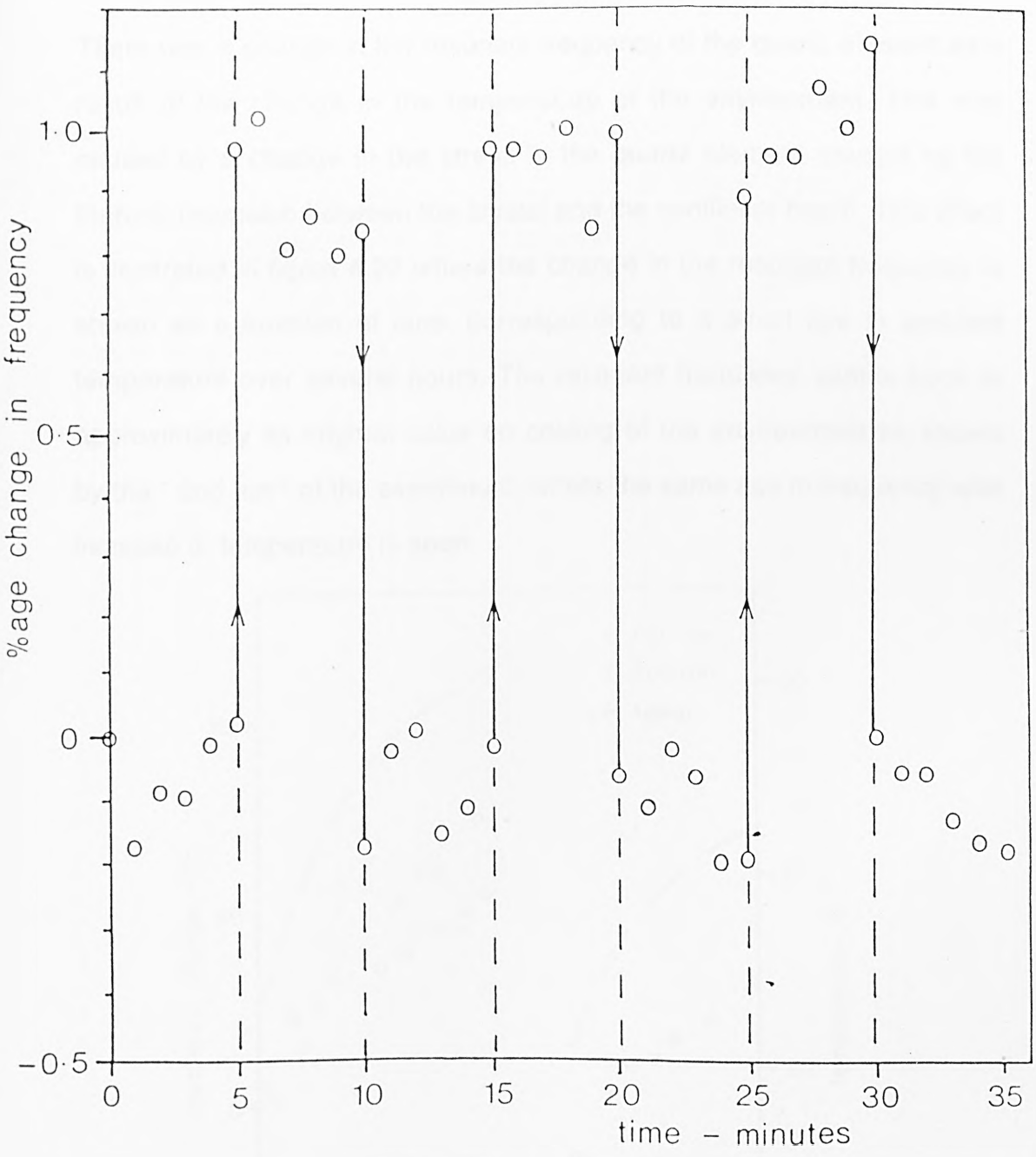

Fig 4.21 Percentage change in resonant frequency of crystal for 5-min cycles of weight applied and weight removed from beam

4.4.1 Thermal Effects

There was a change in the resonant frequency of the quartz element as a result of the change in the temperature of the environment. This was caused by a change in the stress in the quartz element caused by the thermal mismatch between the crystal and the cantilever beam. This effect is illustrated in figure 4.22 where the change in the resonant frequency is shown as a function of time, corresponding to a small rise in ambient temperature over several hours. The resonant frequency settles back to approximately its original value on cooling of the environment as shown by the " 2nd run " of the experiment, where the same rise in frequency with increase in temperature is seen.

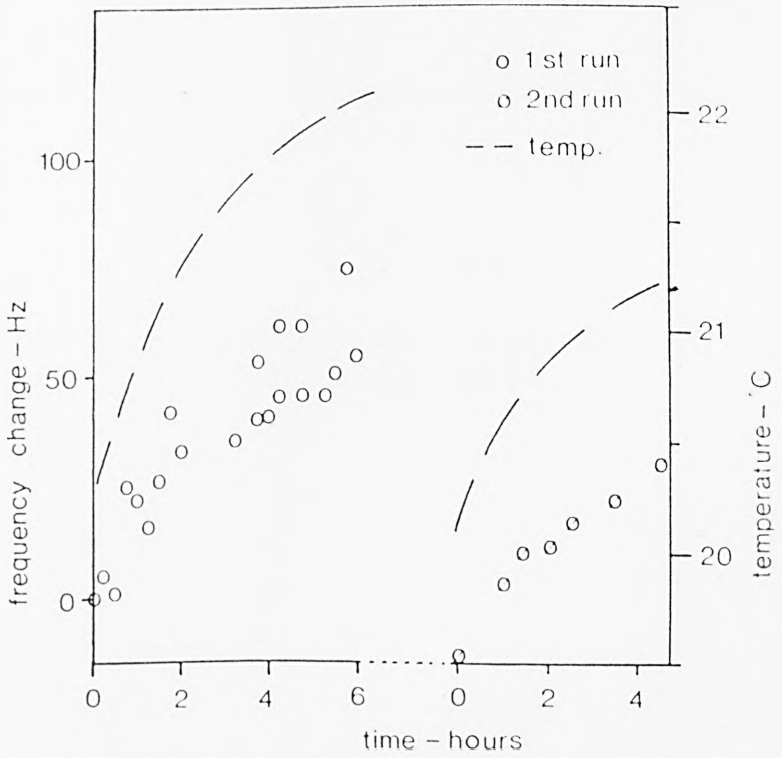

Fig 4.22 Change in resonant frequency of crystal with change in ambient temperature over two time periods.

Temperature compensation can be achieved by matching the thermal expansion of the quartz crystal and cantilever, e.g. the use of a quartz cantilever is possible. Alternatively or additionally thermal effects can be minimised in the scheme proposed by Kirman [50], where two sensors are subjected to the same environmental influences by arranging to have them subjected to opposite stresses when a load is applied, i.e by mounting one crystal beneath the other on the same beam (figure 4.23). The difference in the frequencies of the two sensors then provides a measure of the force as the temperature effects would be cancelled.

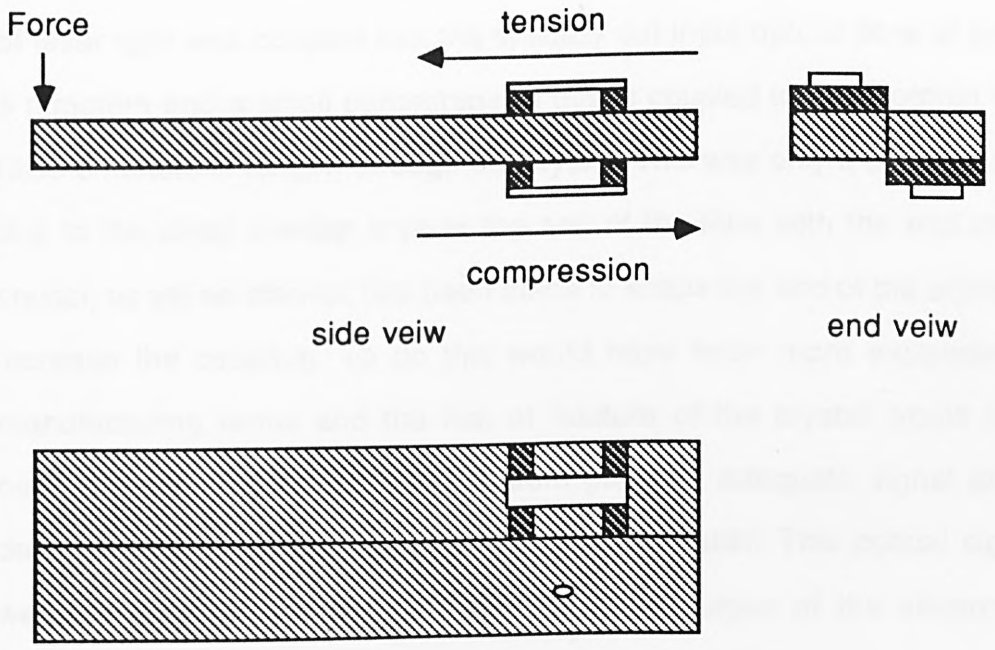

Fig 4.23 Schematic of twin beams for possible temperature compenstion system

4.5 Power Requirements

The power required to drive the system with regard to the electrical/optical configuration, as shown in figure 4.17 was very low. Approximately 1 mW of laser light was coupled into the critically cut input optical fibre of length 5 mmeters and a small percentage of this is coupled into the output fibre (also 5 meters in length) through the crystal. This was only a small fraction due to the small overlap area at the end of the fibre with the end of the crystal; as yet no attempt has been made to shape the end of the crystal to increase the coupling. To do this would have been more expensive in manufacturing terms and the risk of fracture of the crystal would have been greater. The unoptimised system gave an adequate signal at the detector with moderate output power from the laser. This optical signal, was converted in the detector and the other stages of the electronics drove an LED which launched ~1 mW of power at 820 nm into an optical fibre coupled to the PIN diode. This diode was convenient in terms of its size and almost optimum sensitivity at 810nm. The photovoltaic conversion efficiency at this PIN diode was approximately 20%. The 0.4V output was transformed up to ≈ 4V and this voltage was applied to the electrodes. The optical power required to drive the transformer, diode and circuitry was approximately 1mW compared with that of the work of McGlade et al [52] who reported a launch power of 2.2 mW. The power recorded by the diode detector was ~12μW. This figure is small because of the small area overlap between the end of the fibre and the crystal.

4.6 Discussion

A pressure/force sensor using a vibrating quartz crystal was constructed and tested, where the resonance frequency of the crystal was detected via the evanescent field emanating from a critically cut fibre. The crystal was driven into resonance by the photovoltaic conversion of light from an LED via a diode detector and transformer. The system showed good reliability and low hysteresis and a resolution of +/- 5g of the weight applied to the cantilever was obtained. The system relied upon the modulation of light by very small movements of the resonating element (as compared to reflection readout systems - Mallalieu et al [53], Jones et al [54])

Various parameters are not critical in the experimental arrangement, e.g. as shown in Figure 4.12, the width of the gap between the critically cut fibre and the crystal does not have to be set accurately (as long as the crystal moves into the evanescent field) which eases the manufacturing constraints, (particularly if longer wavelengths are used). The condition required is that only a detectable modulation is observed. The transmittance drops to $\approx$ 5% of the peak value as the gap is increased from zero to 0.5μm. The function governing this limits the maximum gap width and although the depth of the modulation is greater when the crystal vibrates with its minimum displacement from the fibre $\leq$ 0.5μm, when the gap exceeds $\approx$1μm it is difficult to observe the modulated signal in the presence of noise. This can be improved by the use of larger wavelengths. The power consumption at the sensor head can be lowered even further by increased optimisation of the system.

The crystal structure is one that can be relatively easily produced and may be produced in large quantities using photolithographic techniques. The other mechanical parts do not require complex production and the circuitry is inexpensive. The He-Ne laser can be replaced by an inexpensive laser diode of modest power, in view of cost reductions seen in very recent years in these devices.

Chapter 5

Photothermally Driven Quartz Sensor

Abstract

In this chapter the feasability of photothermally driving a quartz crystal into resonance and hence using it for a force sensor is studied. It was found that the quartz can indeed be driven into resonance using this method. Some problems were encountered in using this as a force sensor, these are described.

5.1 Introduction

In the previous chapter a hybrid optical force transducer was discussed, where the resonant frequency sensitivity of a quartz oscillator to strain was utilised and the high Q of the crystal, and its piezoelectric properties made it an attractive proposition for use as a force sensor. The power to drive the crystal was delivered optically through a fibre to a photodiode, which converted the optical signal to an electrical signal. This signal was magnified via a transformer, and then used to drive the quartz crystal into resonance. The resonance frequency was detected optically through evanescent wave coupling between a critically cut fibre and the quartz crystal in flexural motion. This frequency was fed back into a phase locked loop which drove an L.E.D. to power the crystal flexural vibrations and hence resonance was maintained.

Clearly this system does not satisfy the requirement that the force/pressure transducer be a totally optical system, even though the electrical power required to drive the crystal was very small of the order of a few microwatts. The system as a whole proved to be very versatile in nature, being as it was fundamentally a frequency modulation technique. Therefore, an all optical pressure transducer would ideally also be a frequency modulation transducer.

The design of the previous (hybrid) system was such that it could easily lend itself to being converted into an all optical system, if a suitable method could be used to drive the crystal into resonance optically.

In this chapter an optical drive system using the photothermal effect (in which absorbed modulated optical power is converted into heat within the device which then causes periodic mechanical expansion) is studied, and it's suitability for use with the hybrid system is discussed. The photothermal drive studied was similar to the method used by Mallalieu [53] and Dieulesaint [55] to drive optically a quartz crystal into resonance, where the optical energy was converted into mechanical energy through the thermal expansion of a thin metallic film deposited upon the crystal.

5.2 Photothermal Effect

A quartz crystal can be excited optically into resonance, by the use of the photothermal effect, where the (modulated) optical power is absorbed by the resonator and is then converted to heat within the device. This causes the periodic mechanical expansion of the resonator and hence, if the optical input is modulated at the resonance frequency of the quartz crystal, then it can be brought into resonance.

The photothermal excitation mechanism of quartz has been modelled by Mallalieu et al [53], where a quartz crystal with a thin layer of nichrome deposited upon it was modelled (Figure 5.1).

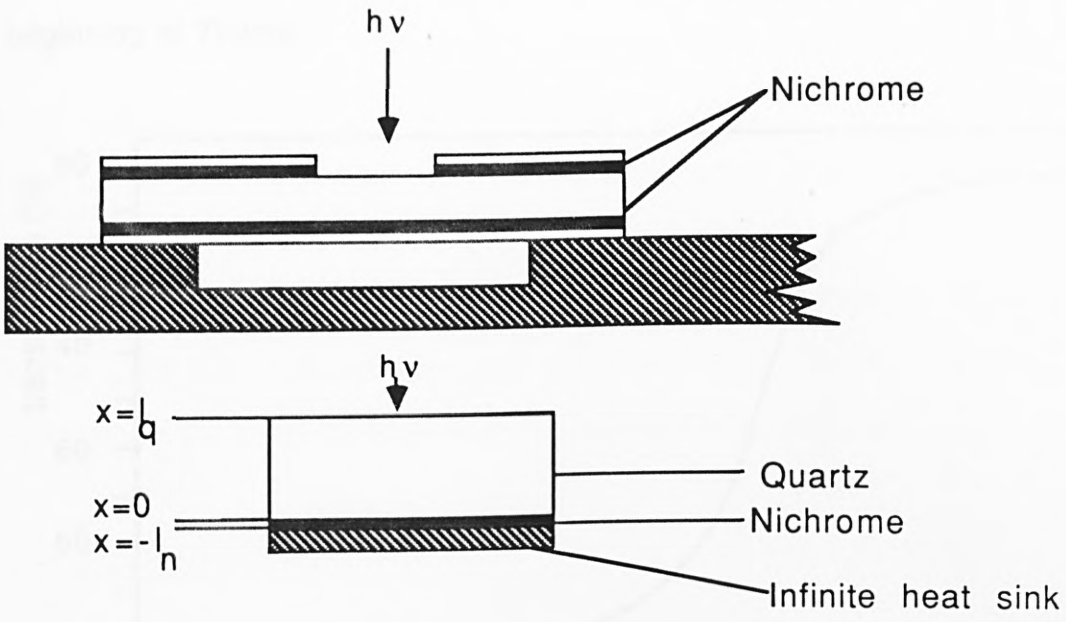

Fig 5.1 Model of Photothermal excitation system

The model was based on a rectangular beam of quartz thickness l_q, with a layer of nichrome thickness l_n in contact with an infinite heatsink. The optical energy from a light source impinges upon the nichrome through the thickness of the quartz. In modelling the resonance some assumptions were made, as listed below:-

(a) The optical to thermal energy conversion occurs in the nichrome since the optical absorption of quartz is negligible from approximately 180nm to 4μm. In contrast the absorption curve of nichrome is shown in Figure 5.2, in the region of 400nm to 900nm, showing a large absorption

beginning at 700nm.

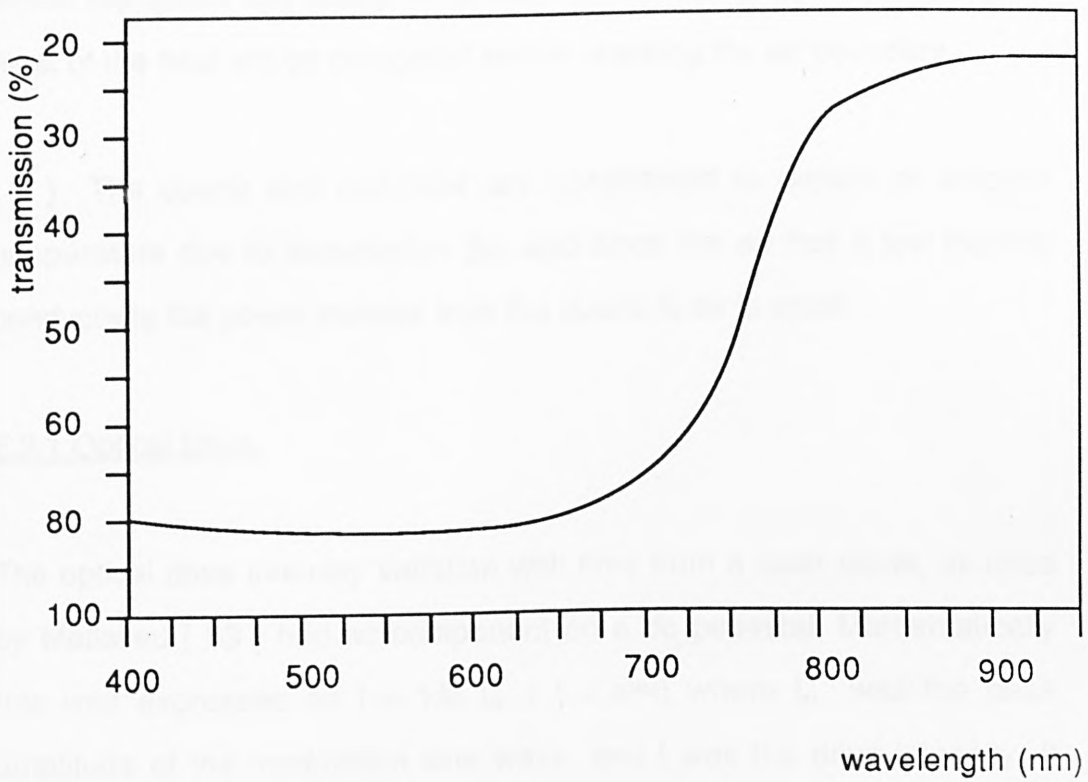

Figure 5.2 Absorption curve of Nichrome

(b) The model assumes an infinite heat sink is attached to the quartz nichrome sandwich, at an ambient temperature of Φ,

(c) The power transfer from the quartz to the surrounding air is negligible since (i) The thermal diffusion length of quartz is 10 microns given by $\mu_q\ (2\alpha/\omega)^{1/2}$, where α = thermal diffusivity = $k/\rho c$; k is thermal

conductivity; ρ = density; c = heat capacity; ω = angular frequency of the optical drive modulation. Therefore the optically induced thermal variation within the quartz will decay by a factor of 1/e every 10 microns, and so most of the heat will be dissipated before reaching the air boundary.

(ii) The quartz and nichrome are constrained to remain at ambient temperature due to assumption (b), and since the air has a low thermal conductivity the power transfer from the quartz to air is small.

5.2.1 Optical Drive

The optical drive intensity variation with time from a laser diode, as used by Mallalieu [53] had ac component on a dc pedestal. Mathematically this was expressed as $I = 1/2\ I_o\ (1 + e^{i\omega t})$ where I_o was the peak amplitude of the modulation sine wave, and I was the drive intensity. It was assumed that the optical intensity in the nichrome was decaying exponentially due absorption and this absorbed power was completely transferred to thermal energy.

The Fourier heat equation, for the flow of heat through plane layers, for the regions of quartz and nichrome then becomes [53]

$$\partial^2\phi_n/\partial x^2 = 1/\alpha_n(\partial\phi_n/\partial t) - (\beta/2k_n)I_o(1+e^{i\omega t})\exp(\beta x), \qquad -l_n \le x \le 0 \qquad (5.1)$$

$$\partial^2\phi_q/\partial x^2 = 1/\alpha_q(\partial\phi_q/\partial t) \qquad 0 \le x \le l_q \qquad (5.2)$$

Where ϕ = complex temperature; β = optical absorption coefficient of nichrome. These equations were solved and applying boundary conditions that stipulated the continuity of temperature and thermal flux across the material interfaces

$$k_q(\partial\phi_q/\partial x) = 0 \qquad x = l_q \text{ no flux into the air} \qquad (5.3)$$

$$\phi_q = \phi_n \qquad (5.4)$$

$$k_q(\partial\phi_q/\partial x) = k_n(\partial\phi_n/\partial x) \qquad x = 0 \text{ continuity of temperature and flux across nichrome quartz interface} \qquad (5.5)$$

$$\phi_q = \phi_o \qquad x = -l_n \text{ nichrome back face at temperature of heat sink} \qquad (5.6)$$

Figure 5.3 shows the distribution of temperature within the quartz and nichrome, the total thickness l_q of the the quartz = 125 microns; the thickness of the nichrome l_n = 2 microns; and I_o the light input intensity = 4000W/m^2 corresponding to average power of 4 mW.

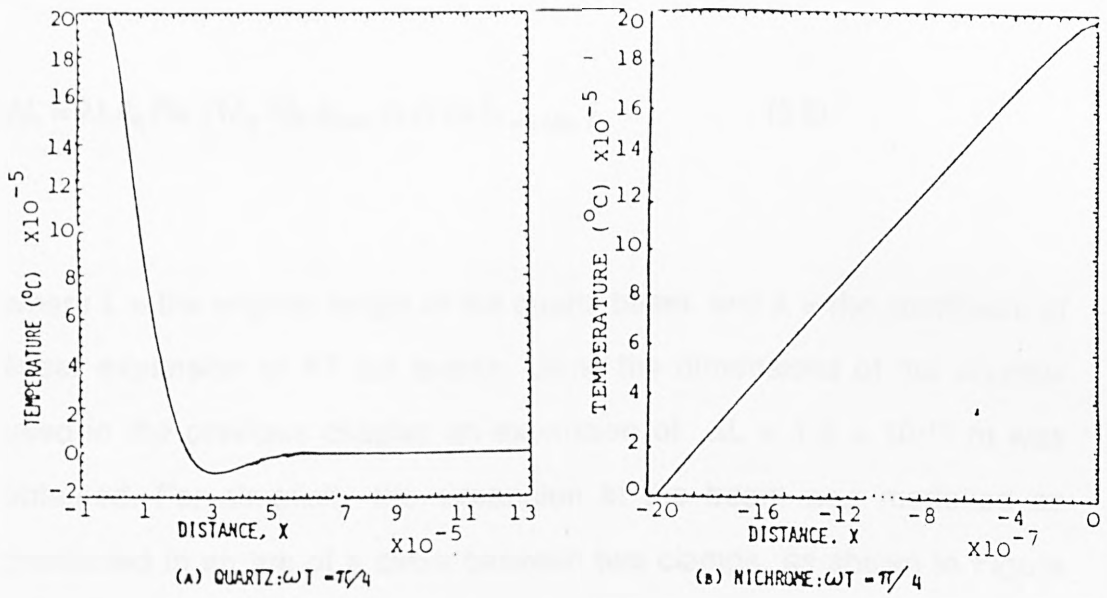

Fig 5.3 Temperature distribution as predicted by Kirman et al [50]

The spatial average of the ac component at $\omega t = \pi/4$ is given by

$$T_{qac} = \mathrm{Re}\{1/l_q \int_0^{l_q} \phi_{qac}(x,t)\,dx\,|_{t=\pi/4\omega}\} \qquad (5.7)$$

Where l_q = thickness of the quartz

The expansion of the quartz due to this temperature determines the amplitude of the beam deflection for the quartz clamped at both ends.

The linear expansion due to this temperature increase is

$$\Delta L = \lambda L/l_q \, \mathrm{Re} \{1/l_q \, {}^{lq}\!\int_0 \phi_{qac}(x,t)\, dx \,|_{t=\pi/4\omega}\} \qquad (5.8)$$

where L = the original length of the quartz beam, and λ = the coefficient of linear expansion of AT cut quartz. Using the dimensions of the crystals used in the previous chapter an expansion of $\Delta L = 1.5 \times 10^{-13}$ m was obtained. For simplicity the expansion of the beam was modelled as distributed in an arc of a circle between two clamps, as shown in Figure 5.4.

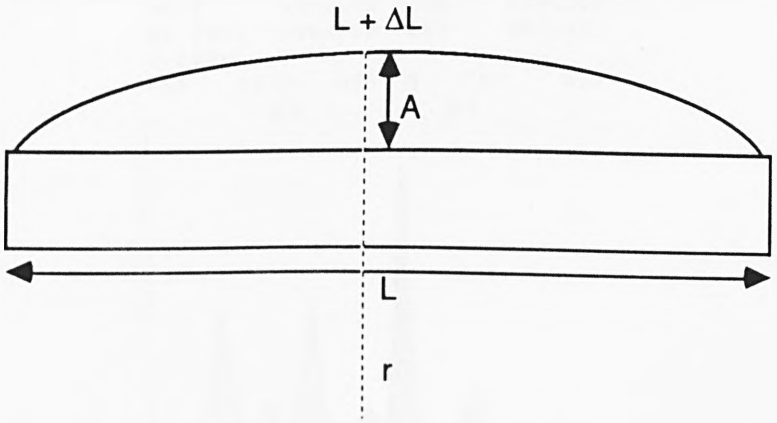

Fig 5.4 Model of flexed quartz beam

The height of the arc centre, A, is given by

$$A = (3L\Delta L / 8)^{1/2}$$

For the drive energy of 4mW and an estimated Q of 2000 [56] the amplitude at resonance of a quartz beam obtained by Mallalieu et al [53] was approximately 50 microns.

5.3 Experimental Setup

An experimental arrangement was devised to test the optical excitation of quartz into resonance, where a layer of nichrome (the relative composition of which is shown in Figure 5.5) 2 microns thick was deposited upon one side of a quartz tuning fork (of the type used in the hybrid work), and a small electrode was deposited upon the other side of the crystal on the central tyne Figure 5.6, as used by Dieulesaint [55].

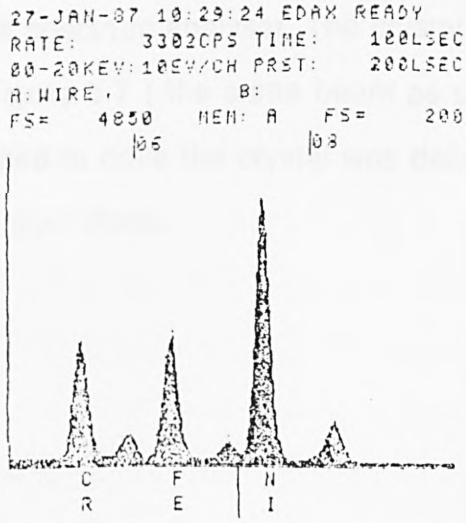

Fig 5.5 Relative composition of nichrome

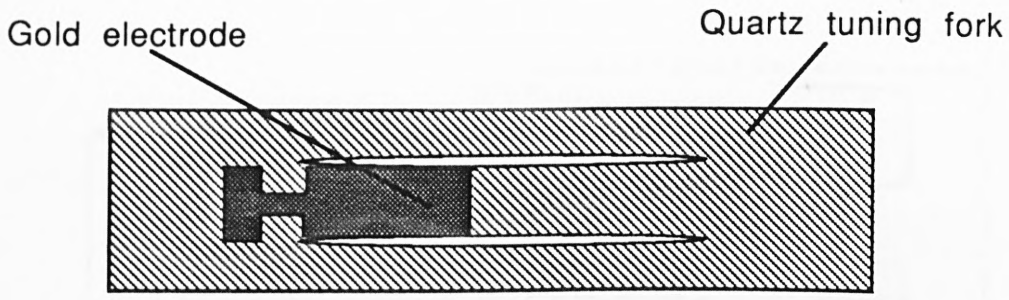

Fig 5.6 Quartz crystal with electrode.

This electrode acted as a resonance detecting system in the first instance i.e. when the crystal was optically driven into resonance in the flexural mode, the bending of the beam induced an electrical charge upon the gold electrode due to the piezoelectric effect; this charge can be detected and displayed on a spectrum analyser. The crystal was then clamped to a cantilever beam Figure 5.7 (the same beam as used in chapter 4). The optical power needed to drive the crystal was delivered via a 600 micron fibre attached to a laser diode.

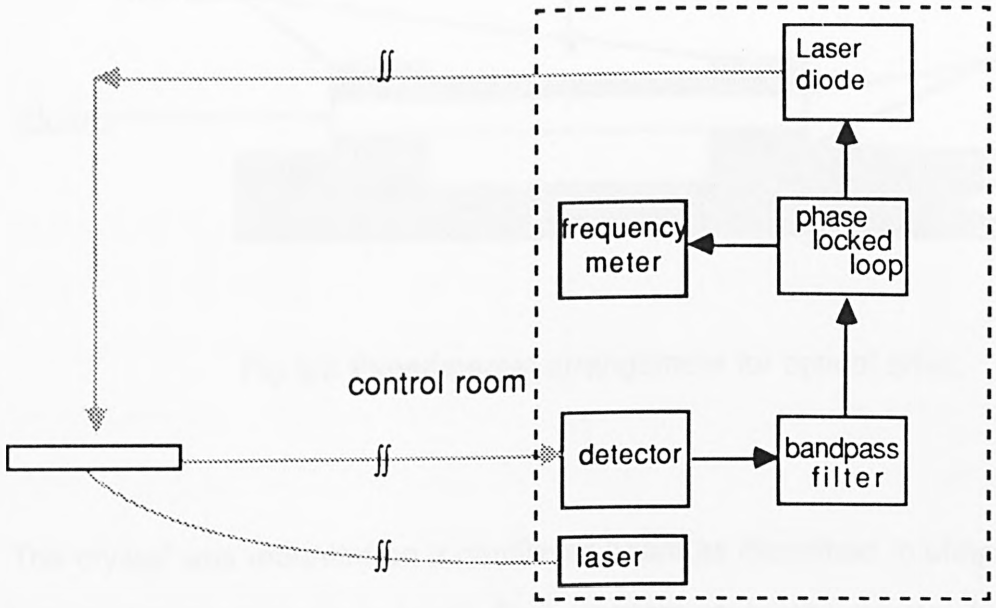

Fig 5.7 Schematic of circuit and detection system used

The arrangement used (figure 5.8) had a few differences from the experiment performed by Mallalieu et al [53], and the model discussed above. These being that the nichrome layer was placed on top of the crystal and the heat sinking achieved via the metal clamps, whereas in the Mallalieu experiment the nichrome layer was placed at the bottom of the crystal in a similar arrangement to that shown on figure 5.1; also Mallalieu did not use a small electrode to detect via the resonance, the resonance in this case was detected the reflection modulation of a c.w. light source.

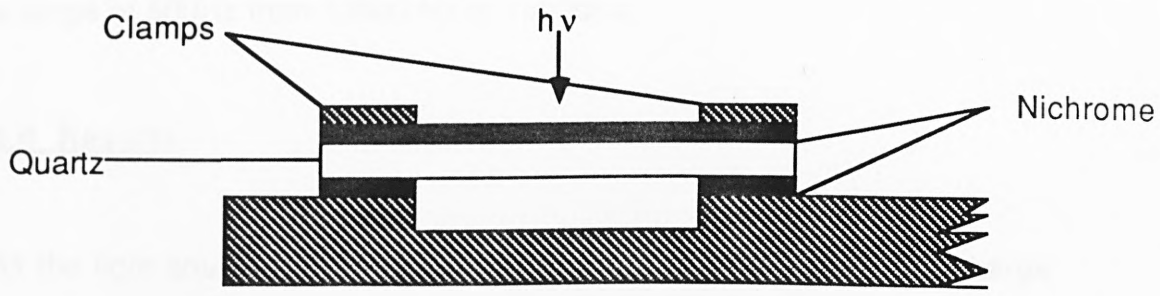

Fig 5.8 Experimental arrangement for optical drive.

The crystal was mounted on a cantilever beam as described in chapter 4, but in this case there was no fibre coming up to the crystal for the evanescent wave detection system. This was removed in order to achieve and test the optical drive of the crystal, initially.

The central tyne was illuminated by light from a laser diode at 750nm with an r.m.s. power output of 20mW. The output light intensity from this diode was launched into a 600μm fibre using a GRIN rod lens arrangement, this gave a power density of 7mW r.m.s. in the fibre. The other end of the fibre was held at distance of 4mm from the quartz crystal and the light emanating from the fibre caused periodic heating and cooling of the thin nichrome layer, which in turn caused periodic heating and cooling of the crystal, hence the crystal was brought into resonance. The laser diode was modulated by the output of a spectrum analyser, which was swept over a range of frequencies so that the output from the laser diode could

be swept over a range frequencies in order to determine the exact resonance frequency of the crystal. The output of the laser was swept over a range of 500Hz from 13500 Hz to 14000Hz.

5.4 Results

As the light source was swept over the range of frequencies the charge induced on the electrode, due to the periodic expansion and contraction of the crystal, was fed back into the spectrum analyser and displayed on the screen (the output is shown in Figure 5.9). As can be seen as the crystal approaches resonance the voltage induced on the electrode increases reaching a maximum at resonance, hence the resonance frequency was determined (13.7 kHz), this proved that the quartz crystal could be successfully driven into resonance by this optical means. The output power of the laser diode was adjusted to determine the effect of the decrease in the driving power to drive the crystal. The amplitudes of the resonance frequencies obtained are shown in Figure 5.10, the large peak corresponds to an optical drive power of 7mW, while the lower peak corresponds to a drive power of 3mW. It can be clearly seen that as the optical power is decreased the induced electrical signal on the electrode decreases corresponding to a decreased amplitude of vibration of the central tyne of the quartz tuning fork. There is also a small shift in the resonance frequency as the power is increased, the reason for this is yet not known, further work is necessary on this and other effects.

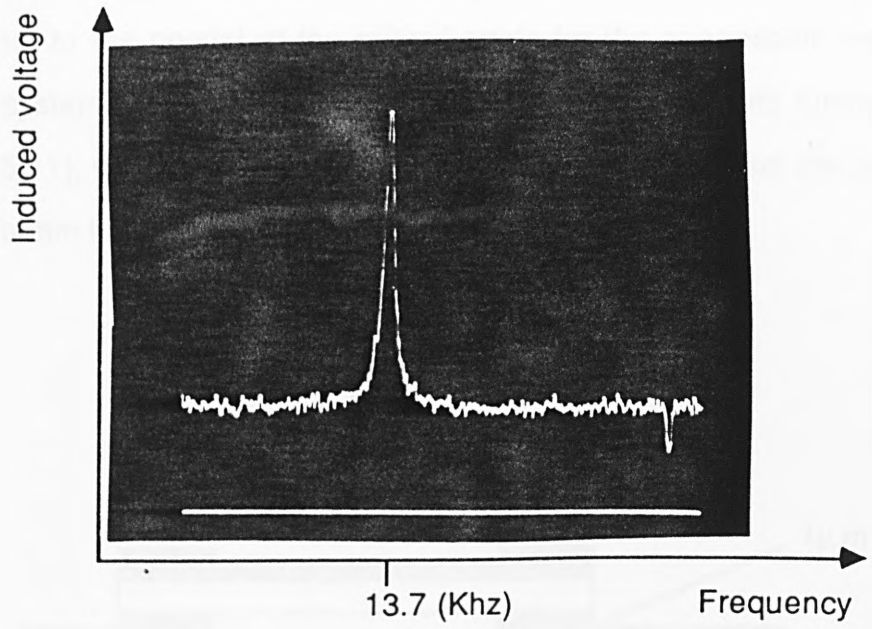

Fig 5.9 Photograph of resonance peak obtained

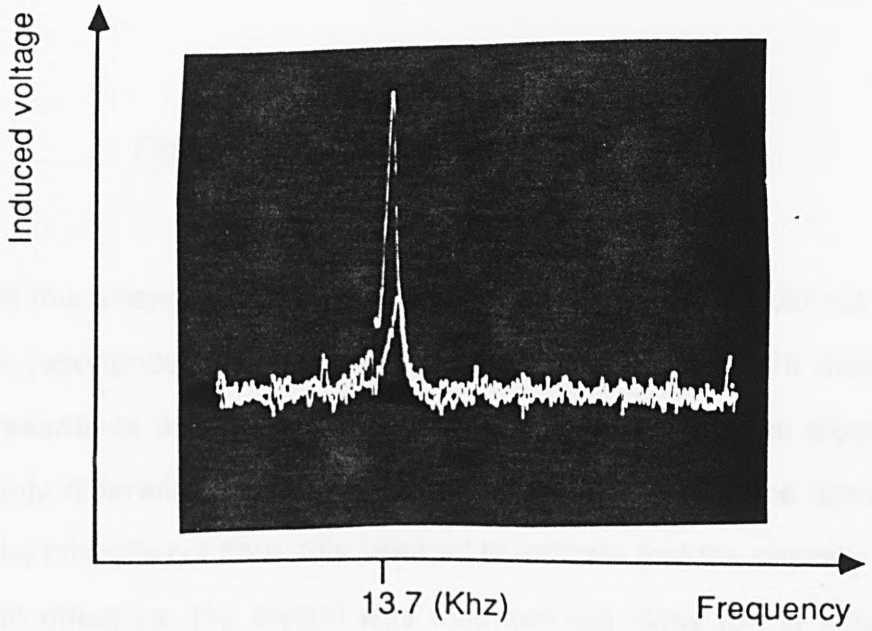

Fig 5.10 Photograph of the change in resonance amplitude with changing drive power.

The crystal was then mounted upon a second beam with the fibre coming up to the crystal at the critical angle for the evanescent wave detection system to optically detect the resonance of the quartz tuning fork (Figure 5.11), with a thin film spacer 1μm thick placed between the crystal and the beam to allow room for the crystal to move.

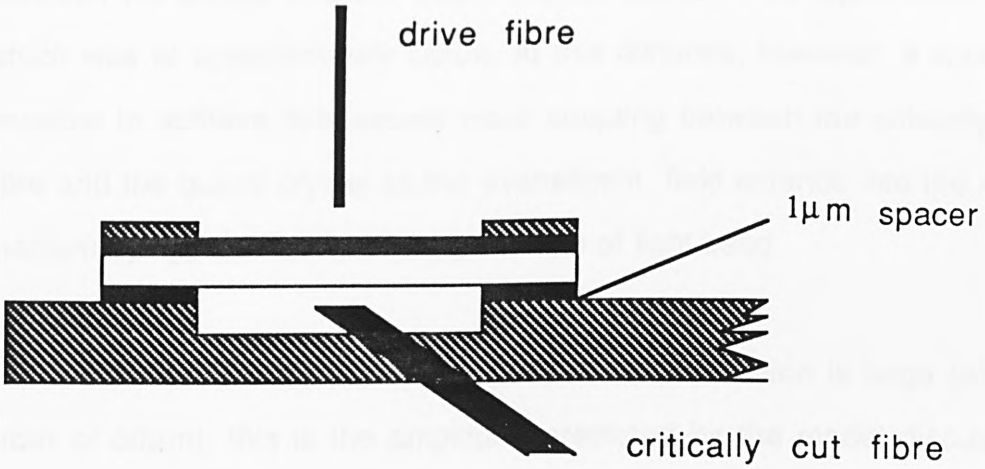

Fig 5.11 Evanescent wave detection system

In this arrangement it was discovered that the crystal did not resonate i.e. A resonance peak was not observed on the spectrum analyser, as the resonance at this point was still monitored through the electrode. As the only difference between this arrangement and the one used earlier was the critically cut fibre, this seemed to indicate that the critically cut fibre had an effect i.e. the crystal was mounted too close to the fibre and hence either the crystal was touching the critically cut fibre at resonance or there was a damping effect due to this fibre. However, the damping of the crystal

vibration would be unlikely, since no such effect was observed with the hybrid device.

To determine the effect of the critically cut fibre upon the crystal at resonance, the gap between the fibre and the crystal was gradually increased by placing a series of mylar spacers of 12μm thickness between the crystal and the beam until resonance was again observed, which was at approximately 60μm. At this distance, however, it was not possible to achieve evanescent wave coupling between the critically cut fibre and the quartz crystal as the evanescent field extends into the rarer medium by approximately one wavelength of light used.

The results could indicate that the amplitude of vibration is large (of the order of 50μm), this is the amplitude predicted by the model discussed above. But similar work done by Marconi suggests that the amplitude vibration is of the order of 2μm [56]; clearly there is a discrepancy between the two systems which can only be resolved by further tests and a more accurate determination of the amplitude of vibration. The amplitude of vibration determined by Marconi was via a simple interferometer arrangement the results of which were not totally accurate but gave an indication of the orders of movement. However, recent work by Grattan et al [57]; using a more accurate mathematical model (using finite element analysis) has shown that the amplitude of vibration is of the order of a micron confirming experimental results at Marconi [56], this is discussed in the next section.

5.5 Conclusions and Future Work.

In this chapter it has been shown that a quartz crystal can be successfully brought into resonance optically by the use of the photothermal effect, where conversion of optical energy to mechanical energy occurs in a thin layer of nichrome deposited on the crystal. This effect can easily lend itself for use in a force/pressure sensor, similar to the one demonstrated in chapter 4, if the resonance frequency could be detected optically in particular via the evanescent coupling used in the hybrid device. However, optical detection of the resonance frequency through evanescent wave coupling between the critically cut fibre and the quartz due to the effect of the fibre upon the crystal could not be used here. The proximity of the fibre to the crystal had the effect of stopping resonance, but resonance was observed at larger distances from the fibre.

It is clear that the effect of the critically cut fibre upon the resonance of the crystal has to be further investigated. The results seem to indicate that the resonance of the crystal was being hindered by the critically cut fibre. This was due to the fact that the two clamping points and the critically cut fibre were not at the same level. The three surfaces should have been at the same level optically flat, but it was found that this was no longer the case, as the beam used was the same as the one used in chapter 4, aging of the epoxy seemed to have caused the fibre to move up by several microns. This in its self is a problem that needs to be addressed, suitable adhesives need to found so that any aging effects can be kept to a minimum, or other methods must be investigated for mounting a critically

cut fibre in a stable manner very close to the vibrating crystal.

For this device to work successfully the amplitude vibration of the quartz crystal needs to be determined more accurately, possibly by interferometric techniques, so that the gap between the critically cut fibre and the crystal can be set more precisely, allowing the crystal, as it oscillates, to move into the evanescent field at maximum amplitude.

The construction of the cantilever beam also needs to be redesigned to eliminate the aging effects of the epoxy resin holding the fibres, machining the cantilever beam and the holder for the critically cut fibre out of one piece of material, whether it be stainless steel or a more closely thermally matched material to quartz. This by contrast to the present case where the fibre is mounted in a steel tube which is then fixed into a hole drilled into the beam at the critical angle.

This system has the potential of being a very powerful pressure/force transducer, which would be an all optical transducer that is digital in nature. It could be made even more powerful by the suitable investigation and use of other materials for the absorbing layer since nichrome absorbs roughly 20% of the input light at 750nm, or alternatively the use of longer wavelengths can be made where the absorption is greater. In this way very little optical power would be required to operate the system, hence, it can be a very cheap and accurate pressure measuring system with all the advantages associated with optical sensors.

Chapter 6

Summary

6.1 Summary

The work described in this thesis has demonstrated that it is possible to produce usable fibre optic pressure/ force sensors using the evanescent wave coupling (or the FTIR effect) between two optical elements. In the first chapter it was shown that there exist many methods by which pressure and other measurands can be detected optically; it was also shown that despite the existence of these methods there is a need for optical pressure sensors which exhibit high degrees of accuracy and repeatability. This work was undertaken to address this deficiency and pressure sensors which exhibited high accuracies were produced.

These sensors were essentially of the intensity modulation type, where the modulation was achieved via the evanescent wave produced at the end of a critically cut fibre in close proximity to a second optical element. An analogue sensor was produced in the first instance, which exhibited high degrees of accuracy, repeatability and close agreement with theory. There were however, some problems associated with the sensor, that made it difficult to use in a more hostile environment than the laboratory. By far the most significant problems associated with this device were thermal in nature due mainly to the differential thermal expansions of the materials used, i.e. differential expansion between the glass fibre and the stainless steel body. As was pointed out in chapter 3 section 3.6 these problems could be overcome by the use of more closely matched materials or the sensor could be used reliably in environments that display minimal temperature changes.

Although this sensor could have been improved further, it was decided to develop a fundamentally more stable sensor which was inherently an intensity modulation type sensor that displayed some digital qualities, such that the intensity of light coupled into a quartz crystal via the evanescent wave was modulated by its oscillation when it was set into resonance. The crystal was driven into oscillation by the photovoltaic conversion of light from an LED via a photodiode detector and a small transformer. This made it a hybrid type sensor as the quartz was driven electrically into resonance.

The crystal was mounted onto a cantilever beam containing a critically cut fibre. As the crystal vibrated it moved into and out of the evanescent field emanating from the end of the fibre, light was coupled into the quartz as it moved close to the fibre, the frequency of resonance of the crystal was optically monitored by observing the intensity of light coupled into the crystal. When a force was applied to the cantilever beam, the strain produced on the surface acted upon the crystal causing a shift in its resonance frequency proportional to the applied force. By monitoring the shift in the frequency the applied force or pressure could easily be determined. The system showed good response with good reliability and low hysteresis, with a resolution of +/- 5g of the weight applied to the cantilever beam.

This system also exhibited a few thermal problems, such as the shift in resonance frequency of the crystal due to the differential thermal

expansion between the quartz and the cantilever beam. This problem can be overcome again by the use of thermally matched materials or by having a second crystal mounted on a cantilever beam which is in compression when the first crystal is in tension, so by the use of frequency difference methods the temperature effects can be eliminated.

This system however, was not completely satisfactory as the aim of the project was to produce an all optical pressure sensor, so it was necessary to find a method of driving the quartz into resonance directly by shining light upon it. This was achieved by the use of the photothermal effect, where light absorbed by a thin film absorbed on to the surface of the quartz was converted into heat by the absorption mechanism causing an expansion of the crystal, which depended upon the intensity of the irradiation. The irradiating light was channelled through a fibre to the crystal from a laser diode, which was modulated at the resonance frequency of the crystal. Therefore as the crystal heated up and cooled down it expanded and contracted hence causing oscillation at its resonance frequency and being driven optically. This crystal was also mounted upon a cantilever beam as in the hybrid system, but, however, it proved difficult to monitor the frequency of the oscillation optically through the FTIR effect. The difficulties arose due to the design and construction of the cantilever beam, where the aging effects of the epoxy used to hold the critically cut fibre caused the misalignment of the polished surfaces, leading to problems in obtaining the correct gap between the crystal and the critically cut fibre. These problems can be overcome by accurately determining the amplitude of vibration and hence achieving the correct gap between the crystal and the fibre, also by a better design of the

cantilever beam where these effects can be reduced or eliminated.

Appendix A

Theory of Evanecant Wave Coupling Between Two Optical Elements

A.1 Introduction

In chapter 2 the theoretical equations leading to F.T.I.R. (or Evanescent wave coupling) were disscused, these equations are described in more detail. In order to gain an understanding of F.T.I.R. it is necessary to understand the interaction of a plane light wave with an interface between two dielectric media. In this section the nature of the interaction will be investigated starting with a plane wave interacting with a boundary and leading to the phenomenom of Total Internal Reflection (T.I.R.) and Frustrated Total Internal Reflection (F.T.I.R.), as described by Hechet [58] and Brekhovskikh [59].

A.2 Waves at an Interface.

Consider an incident plane light wave which is monochromatic, having the form

$$\mathbf{E}_i = \mathbf{E}_{oi} \exp[i(\mathbf{k}_i . \mathbf{r} - \omega_i t)] \quad \text{.....A.1}$$

or in a simpler form.

$$\mathbf{E}_i = \mathbf{E}_{oi} \cos(\mathbf{k}_i . \mathbf{r} - \omega_i t) \quad \text{.....A.2}$$

Assuming that the wave is linearly polarised i.e. $\mathbf{E}_{oi}$ is a constant in time, the reflected and transmitted wave can be written in the form

$$\mathbf{E}_r = \mathbf{E}_{or} \cos(\mathbf{k}_r . \mathbf{r} - \omega_r t + \varepsilon_r) \quad \text{.....A.3}$$

$$\mathbf{E}_t = \mathbf{E}_{ot} \cos(\mathbf{k}_t \cdot \mathbf{r} - \omega_t t + \varepsilon_t) \quad \text{.....A.4}$$

Where ε_r & ε_t are the phase constants relative to $\mathbf{E}_i$: these are introduced because the position of the origin is not unique. The total tangential component of the the electric field intensity **E** must be continuous across the boundary. Therefore if $\mathbf{U}_n$ is the unit vector normal to the interface then

$$\mathbf{U}_n \times \mathbf{E}_i + \mathbf{U}_n \times \mathbf{E}_r = \mathbf{U}_n \times \mathbf{E}_t \quad \text{.....A.5}$$

Figure A.1 shows the waves in the vicinity of the interface between two dielectric media of indices n_i & n_t .

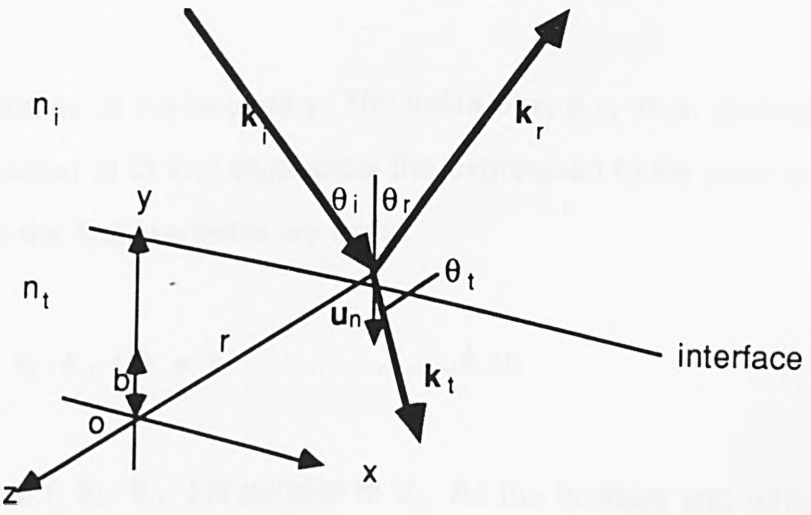

Fig A.1 Shows E-M waves at an interface between two dieiectric media .

$$\Rightarrow \mathbf{U}_n \times \mathbf{E}_{oi} \cos(\mathbf{k}_i \cdot \mathbf{r} - \omega_i t) + \mathbf{U}_n \times \mathbf{E}_{or} \cos(\mathbf{k}_r \cdot \mathbf{r} - \omega_r t + \varepsilon_r)$$

$$= \mathbf{U}_n \times \mathbf{E}_{ot} \cos(\mathbf{k}_t \cdot \mathbf{r} - \omega_t t + \varepsilon_t) \quad \text{.....A.6}$$

This must be true of any point and of any line along the boundary, therefore at the boundary

$$(\mathbf{k}_i \cdot \mathbf{r} - \omega_i t) = (\mathbf{k}_r \cdot \mathbf{r} - \omega_r t + \varepsilon_r) = (\mathbf{k}_t \cdot \mathbf{r} - \omega_t t + \varepsilon_t) \quad \text{.....A.7}$$

The cosines in A.6 cancel leaving an expression independent of t & r. Since this is true for values of time, the coeffients of t must be equal.

$$\omega_i = \omega_r = \omega_t \quad \text{.....A.8}$$

futhermore

$$(\mathbf{k}_i \cdot \mathbf{r}) = (\mathbf{k}_r \cdot \mathbf{r} + \varepsilon_r) = (\mathbf{k}_t \cdot \mathbf{r} + \varepsilon_t) \quad \text{... A.9}$$

where **r** terminates at the boundary. The value of ε_r & ε_t must correspond to a given position of O and thus allow the expression to be valid at any location. From the first two terms we have:

$$(\mathbf{k}_i - \mathbf{k}_r) \cdot \mathbf{r} = \varepsilon_r \quad \text{.....A.10}$$

This impies that $(\mathbf{k}_i - \mathbf{k}_r)$ is parallel to $\mathbf{U}_n$. As the incident and reflected waves are in the same medium, $\mathbf{k}_i = \mathbf{k}_r$. And since $(\mathbf{k}_i - \mathbf{k}_r)$ has no component in the plane of the interface i.e. $\mathbf{U}_n \times (\mathbf{k}_i - \mathbf{k}_r) = 0$,

therefore

$$\mathbf{k}_i \sin\theta_i = \mathbf{k}_r \sin\theta_r \quad \text{.....A.11}$$

This implies the law of reflection

$$\theta_i = \theta_r$$

since ($\mathbf{k}_i - \mathbf{k}_r$) is parallel to $\mathbf{U}_n$ all three vectors or in the same plane.

From eqn. A.9

$$(\mathbf{k}_i - \mathbf{k}_t) . \mathbf{r} = \varepsilon_t \qquad \text{.....A12}$$

Therefore ($\mathbf{k}_i - \mathbf{k}_t$) is also normal to $\mathbf{U}_n$. Hence $\mathbf{k}_i$, $\mathbf{k}_r$, $\mathbf{k}_t$ and $\mathbf{U}_n$ are all coplanar. The tangential component of $\mathbf{k}_i$ & $\mathbf{k}_t$ must be equal.

$$\mathbf{k}_i \sin\theta_i = \mathbf{k}_t \sin\theta_t \qquad \text{.....A.13}$$

since $\omega_i = \omega_t$ mulitplying both sides by c / ω_i gives

$$n_i \sin\theta_i = n_t \sin\theta_t \qquad \text{.....A.14}$$

which is Snell's law. If the origin had been chosen to be the boundary then from eqn. A.10 & A. 12 it is evident that ε_r & ε_t would be zero.

A3 Derivation of Fresnel Equations

In section A.2, the relationship between the phases of $\mathbf{E}_i(\mathbf{r},t)$. $\mathbf{E}_r(\mathbf{r},t)$ and $\mathbf{E}_t(\mathbf{r},t)$ at the boundary was discussed. The interdependence of the amplitudes of $\mathbf{E}_{oi}$, $\mathbf{E}_{or}$, $\mathbf{E}_{ot}$ is now evaluated. For a plane monochromatic wave incident upon the a planar surface separating two isotropic media, the **E** and **B** fields shall be resolved into parallel & perpendicular components to the plane of incidence. These constituents shall be treated

separately.

A3.1 **E** Perpendicular to the Plane of Incidence

Assuming that **E** is perpendicular to the plane of incidence and **B** is parallel to it (Fig A2). Recalling E = vB so that

$$\mathbf{K} \times \mathbf{E} = \mathbf{vB} \qquad \text{(A15)}$$

$$\mathbf{K} \cdot \mathbf{E} = 0 \qquad \text{(A16)}$$

i.e. **E**, **B** and unit propagation vector **K** form a right handed system.

Making use of the continuity of the tangential components of the **E** field, we have the boundary at any time and any point

$$E_{oi} + E_{or} = E_{ot} \qquad \text{(A17)}$$

where the cosines cancel.

The normal component of **B** is continuous as is the tangential component of $\mu^{-1}\mathbf{B}$. The effect of the two media appears via their permeabilities μ_i and μ_t .

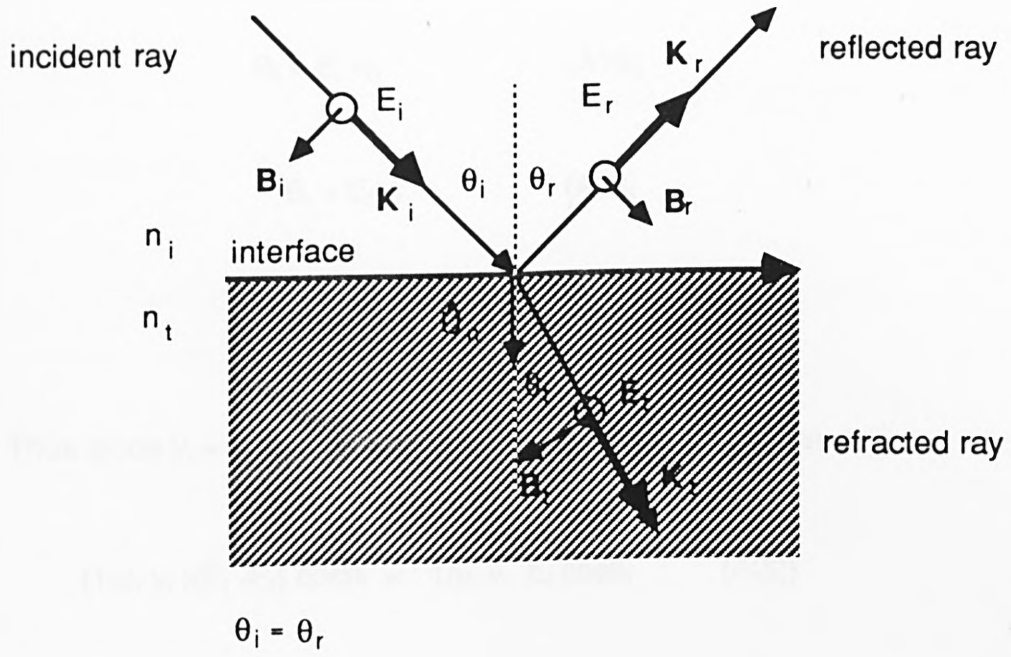

Fig A.2 An incoming wave whose E- field is normal to the plane of incidence

The continuity of the tangential component of $\mathbf{B}/\mu$ requires that

$$-\mathbf{B}_i/\mu_i \cos\theta_i + \mathbf{B}_r/\mu_r \cos\theta_r = -\mathbf{B}_t/\mu_t \cos\theta_t \qquad \text{(A18)}$$

where the left and the right hand sides are the total magnitudes of $\mathbf{B}/\mu$ parallel to the interface in the incident and transmitting media respectively. The positive direction is that of increasing x so that the components of $\mathbf{B}_i$ and $\mathbf{B}_t$ appear with minus signs. From equation A1 we have

$$B_i = E_i / v_i \qquad \text{(A19)}$$

$$B_r = E_r / v_r \qquad \text{(A20)}$$

$$B_t = E_t / v_t \qquad \text{(A21)}$$

Thus since $v_i = v_r$ and $\theta_i = \theta_r$ equation A18 can be written as

$$(1/\mu_i v_i)(E_i - E_r)\cos\theta_i = 1/\mu_i v_i \; E_i \cos\theta_t \qquad \text{(A22)}$$

making use of equation A.2, A.3 and A.4 and remembering that Cosines therein equal one at y=0 we have

$$n_i/\mu_i \, (E_{oi} - E_{or})\cos\theta_i = n_t/\mu_t \, E_{ot} \cos\theta_t \qquad \text{(A23)}$$

combining this with equation A17

$$(E_{or}/E_{oi}) = [(n_i/\mu_i)(\cos\theta_i) - (n_t/\mu_t)(\cos\theta_t)] / [(n_i/\mu_i)(\cos\theta_i) + (n_t/\mu_t)(\cos\theta_t)] \qquad \text{(A24)}$$

and

$$(E_{or}/E_{oi}) = 2\,(n_i/\mu_i)(\cos\theta_i) / [(n_i/\mu_i)(\cos\theta_i) + (n_t/\mu_t)(\cos\theta_t)] \qquad \text{(A25)}$$

These two expressions, which are completely general statements applying to any linear, isotropic, homogeneous media, are two of what are called the Fresnel equations. For dielectrics for which $\mu_i \approx \mu_t \approx \mu_0$ these equations are simply

$$r_\perp \equiv (E_{or}/E_{oi})=(n_i \cos\theta_i - n_t \cos\theta_t)/(n_i\cos\theta_i + n_t\cos\theta_t) \qquad (A26)$$

and

$$t_\perp \equiv (E_{or}/E_{oi})=(2n_i \cos\theta_i)/(n_i\cos\theta_i + n_t\cos\theta_t) \qquad (A27)$$

$r_\perp$ is the amplitude reflection coefficient

$t_\perp$ is the amplitude transmission coefficient

A3.2 **E** Parallel to the plane of incidence

A similar pair of equations can be derived when the incoming **E** field lies in the plane of incidence as shown in Fig A3. The continuity of the tangential components of **E** in either side of the boundary leads

$$E_{oi}\cos\theta_i - E_{or}\cos\theta_r = E_{ot}\cos\theta_t \qquad (A28)$$

In very much the same way as before the continuity of tangential components of B/μ yields

$$(1/\mu_i v_i)\, E_{oi} + (1/\mu_r v_r)\, E_{or} = (1/\mu_t v_t)\, E_{ot} \qquad \text{(A29)}$$

using $\mu_i = \mu_r$ and $\theta_i = \theta_r$ the equation can be combined to give two more Fresnel equations:

$$r_{||} \equiv (E_{or}/E_{oi}) = [(n_t/\mu_t)\cos\theta_i - (n_i/\mu_i)\cos\theta_t]/[(n_t/\mu_t)\cos\theta_i + (n_i/\mu_i)\cos\theta_t] \qquad \text{(A30)}$$

and

$$t_{||} \equiv (E_{ot}/E_{oi}) = [2(n_t/\mu_t)\cos\theta_i]/[(n_t/\mu_t)\cos\theta_i + (n_i/\mu_i)\cos\theta_t] \qquad \text{(A31)}$$

When both media forming the interface are dielectrics the amplitudes become

$$r_{||} \equiv (E_{or}/E_{oi}) = (n_t\cos\theta_i - n_i\cos\theta_t)/(n_t\cos\theta_i + n_i\cos\theta_t) \qquad \text{(A32)}$$

and

$$t_{||} \equiv (E_{or}/E_{oi}) = (2n_i\cos\theta_i)/(n_i\cos\theta_t + n_t\cos\theta_i) \qquad \text{(A33)}$$

These four equations A.30 ,A.31 , A.32 & A.33 are completely general statements which can apply to any linear, isotropic, homogoneous media and are known as the Fresnel equations.

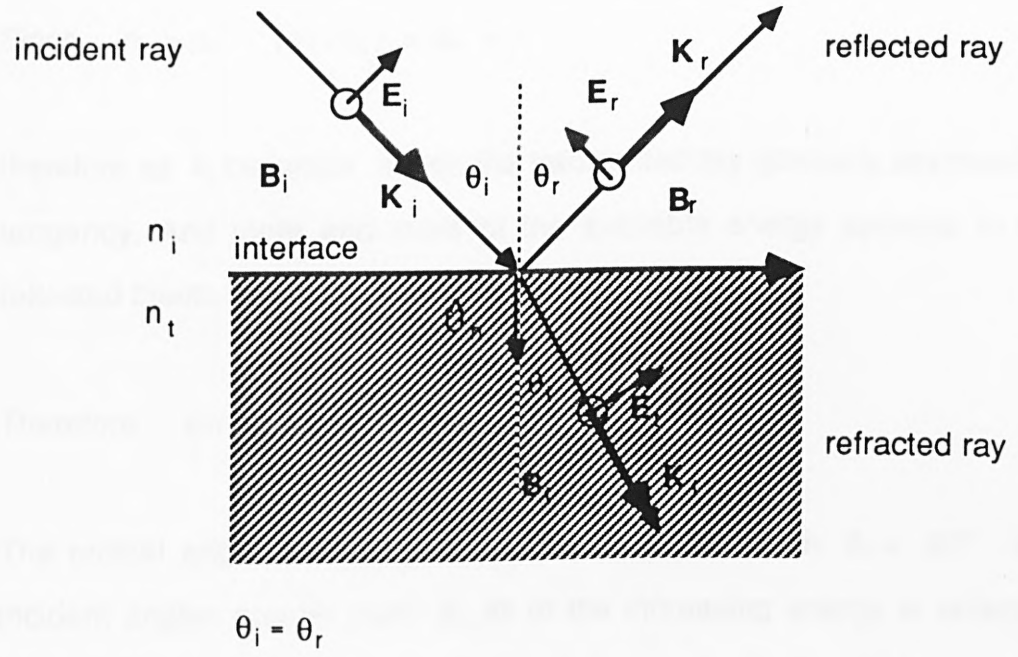

Fig A.3 An incoming wave whose E- field is in the plane of incidence

2.4 Total Internal Reflection

When the incidence medium has a refractive index which is greater than that of the transmittance medium (i.e. $n_i > n_t$) the angle of incidence is always less than the angle of transmittance. In this case for a certain angle of incidence, θ_c the so called "critical angle" we have total internal reflection. From Snell's law we have

$$\sin \theta_i = (n_t / n_i) \sin \theta_t$$

Since $n_i > n_t$ $(n_t / n_i) = n_{ti} < 1$

therefore as θ_i becomes larger, the transmitted ray gradually approaches tangency. And more and more of the available energy appears in the reflected beam. When $\theta_t = 90^o$, $\sin \theta_t = 1$.

Therefore $\sin \theta_c = n_{ti}$

The critical angle is that special value of θ_i for which $\theta_t = 90^o$. For incident angles greater than θ_c all of the increasing energy is reflected back into the incident medium giving total internal reflection. This is shown in Figure A4.

If it is assumed that there is no transmitted wave when the angle of incidence increases beyond the critical angle, the boundary conditions are not satisfied using only the incident & reflected waves.

The equations A30 & A31 for the reflection coefficient can be rewritten in the form

$$r_\perp = [\cos \theta_i - (n_{ti}^2 - \sin^2 \theta_i)^{1/2}]/ [\cos \theta_i + (n_{ti}^2 - \sin^2 \theta_i)^{1/2}] \quad \text{.....A.34}$$

$$r_{||} = [n_{ti}^2 \cos \theta_i - (n_{ti}^2 - \sin^2 \theta_i)]/ [n_{ti}^2 \cos \theta_i + (n_{ti}^2 - \sin^2 \theta_i)] \quad \text{.....A.35}$$

It can be seen that since $\sin \theta_c = n_{ti}$ when $\theta_i > \theta_c$,

$\sin \theta_i > n_{ti}$ therefore both $r_\perp$ & $r_{||}$ become complex quantities. But $r_\perp r_\perp{}^* = r_{||} r_{||}{}^* = 1$ and R = 1 which means that $I_r = I_i$ and $I_t = 0$. Although we have a transmitted wave it cannot on average carry any energy across the boundary. An indication of the transmitted wave can be seen from the following equations

The transmitted electric field is given by

$$\mathbf{E} = \mathbf{E}_{ot} \exp i (\mathbf{k}_t \cdot \mathbf{r} - \omega t)$$

$$\mathbf{k} \cdot \mathbf{r} = k_{tx} x + k_{ty} y$$

there is no Z component of **k**.

but $k_{tx} = k_t \sin \theta_i$ from Figure (A5)

and $k_{ty} = k_t \cos \theta_t$

using Snell's law

$$k_t \cos \theta_t = +/- k_t [1 - (\sin^2 \theta_i / n_{ti}^2)]^{1/2} \quad .....A.36$$

when $\sin \theta_i > n_{ti}$

$$k_{ty} = +/- i k_t [(\sin^2 \theta_i / n_{ti}^2) - 1]^{1/2} = + i \alpha \quad ....A.37$$

while $k_{tx} = (k_t \sin \theta_i) / n_{ti}$

therefore

$$E_t = E_{ot} \; e^{+/-\alpha y} \; e^{i[\,(ktx \sin\theta i)/nti \; - \omega t\,]} \qquad \ldots A.38$$

If the positive exponential which is physically unattainable is neglected, a wave whose amplitude decreases exponentially as it penetrates the less dense medium is left. This wave travels along the x-direction and is called the evanscent wave.

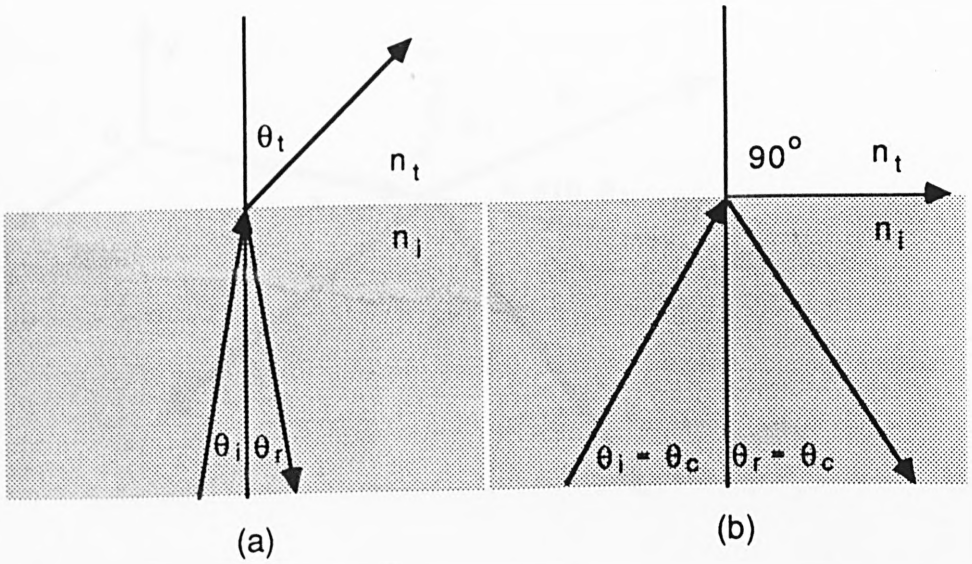

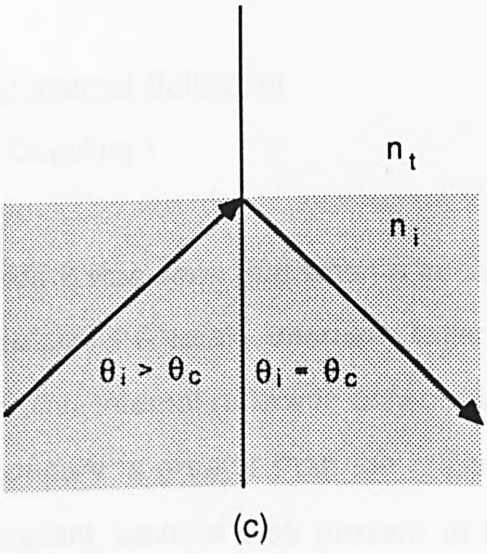

Fig A.4 Schematic of total internal reflection ($n_i > n_t$)

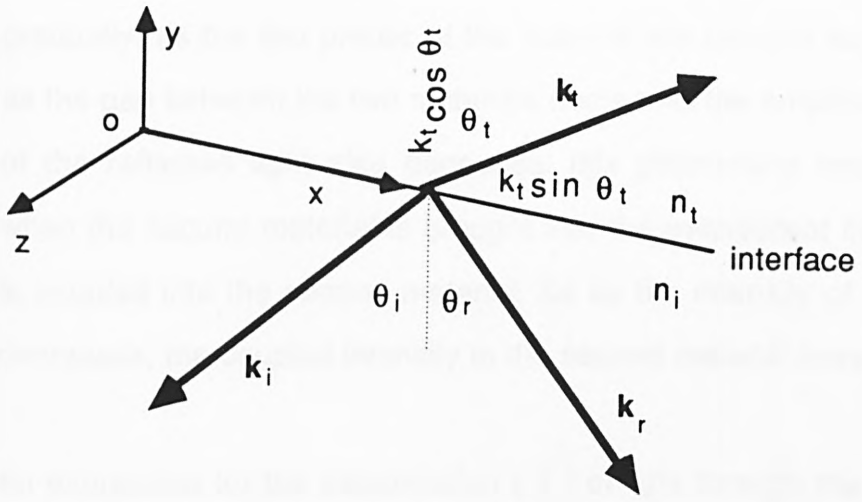

Fig A.5 Propagation of vectors for internal reflection

A.5 Frusatrated Total Internal Reflection

(Evanescent Wave Coupling)

In the previous section it was seen that when a beam of light propagates within a "dense" medium, it is totally internally reflected at the boundary with a rarer medium. This internal reflection only occurs when the angle of incidence to the boundary is greater than the critical angle. It was also seen that an evanescent wave is also present at the boundary and it decreases exponentially as it penetrates into the rarer medium.

The total internal reflection at the boundary can be eliminated by placing a piece of material with similar optical properties as the dense medium (i.e similar or equal refractive indices) placed flush in contact with the original dense medium. In this case there is effectively no boundary. This condition of total internal reflection to no reflection can be achieved

gradually, as the two pieces of the material are brought together. That is as the gap between the two materials decreases the amplitude or intensity of the reflected light also deceases. this phenonena occurs because, when the second material is brought into the evanescent field some light is coupled into the second material. So as the intensity of reflected light decreases, the coupled intensity in the second material increases.

An expression for the transmission (T) of light through the gap between the two materials is now derived.

Consider the expression for the reflection coefficient for a simple boundary (eqn A.30)

$$r_{\perp} = (n_i \cos\theta_i - n_t \cos\theta_t) / (n_i \cos\theta_i + n_t \cos\theta_t)$$

this can be rewritten in the form

$$r_{\perp} = (z_t - z_i)/(z_t + z_i) \quad . \qquad \text{A.39}$$

where $z_t = z_t^o / \cos\theta_t$ A.40

$z_i = z_i^o / \cos\theta_i$ A.41

and $z_t^o = (\mu_t / \varepsilon_t)^{1/2} = 1/n_t$

$z_i^o = (\mu_i / \varepsilon_i)^{1/2} = 1/n_i$

If we now consider the case when two layers of the dense media which

are seperated by a less dense medium of thickness d (Figure A6)

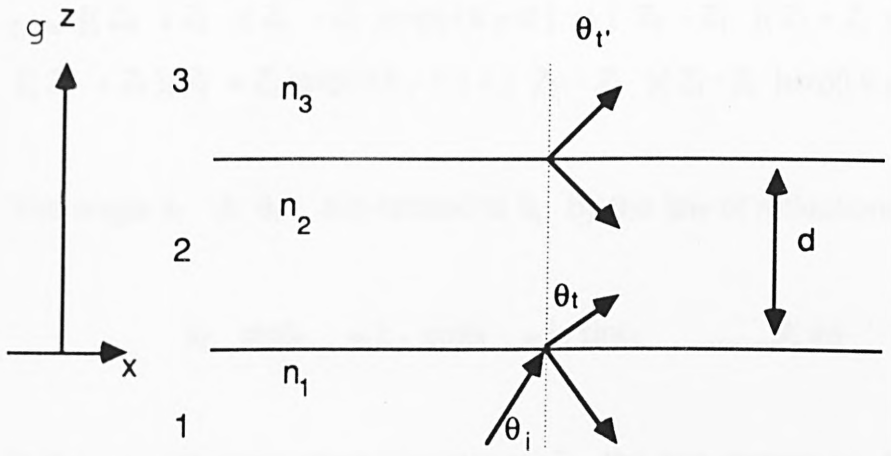

Fig A.6 Schematic of two layers of dense media seperated by a less dense medium of thicness d

In order to find the reflection coefficient from boundary 23 we need the impedence of the boundary 12. The reflection co-efficient $r_\perp$ from Equation A.39 is now given by

$$r_\perp = (Z_{in} - Z_i) / (Z_{in} + Z_i) \quad \text{.....A.42}$$

where Z_{in} is given by

$$Z_{in} = (Z_{t'} - iZ_t \tan k_{t''} d) / (Z_t - iZ_{t'} \tan k_{t''} d) \quad \text{.....A.43}$$

now substituting (A.43) into (A. 42)

we have

$$r_{\perp} = [(Z_{t'} + Z_t)(Z_t - Z_i)\exp(-i k_{t''} d) + (Z_{t'} - Z_t)(Z_t + Z_i)\exp(i k_{t''} d)]/$$
$$[(Z_{t'} + Z_t)(Z_t + Z_i)\exp(-i k_{t''} d) + (Z_{t'} - Z_t)(Z_t - Z_i)\exp(i k_{t''} d)].....A.44$$

The angle θ_t & $\theta_{t'}$ are related to θ_i by the law of reflections.

$$k_{t'} \sin\theta_{t'} = k_t \sin\theta_t = k_i \sin\theta_i \quad .....A.45$$

In the special case when impedence Z_{in} the two denser media are equal i.e. $Z_{t'} = Z_i$ equation (A.44) can be written in the form

$$r_{\perp} = (Z_t^2 - Z_{t'}^2) / (Z_{t'}^2 + Z_t^2 + 2i Z_{t'} Z_t \cot k_{t''} d)..A.46$$

if the Z = 0 i.e. d = 0 we have

$$r_{\perp} = (Z_{t'} - Z_i)/(Z_{t'} + Z_i)$$

If, however, d --> ∞ then the angles of incidence exceeding the critical angle total internal reflection would take place. In case of a finite layer total internal reflection will not take place and partial penetration throughout the layer will occur.

From equation (A.45) we have

$$\sin\theta_t = (k_i / k_t) \sin\theta_i \quad .....A.47$$

for $\theta_i > \arcsin(k_i/k_t)$ $\sin\theta_t > 1$

therefore θ_t must be complex

$$\cos\theta_t = +/- i[(k_t/k_i)^2 \sin^2\theta_i - 1]^{1/2} \quad \text{.....A.48}$$

therfore

$$k_{t''} = k_t \cos\theta_t$$

substituting $\cos\theta_t$ in (A. 40)

we have

$$Z_t = iZ_t^o [(k_t/k_i) \sin^2\theta_i - 1]^{-1/2} = i\delta \quad \text{...A.49}$$

Z_t is therefore purely imaginary.

let $\beta = |k_{t''} d| = k_t d [(k_i/k_r)^2 \sin^2\theta_i - 1]^{1/2}$ ..A.50

but $k_i/k_t = n_i/n_t$ let $n_t \approx 1$ & $k_{t''} = 2\pi/\lambda$

$$\beta = |k_{t''} d| = (2\pi d/\lambda)[n_i^2 \sin^2\theta_i - 1]^{1/2} \quad \text{.....A.51}$$

if Z_i & $Z_{t'}$ are identical we have from equation (A.46)

$$r_\perp = (Z_i^2 + \delta^2)(\delta^2 - Z_i^2 - 2i Z_i \delta \coth\beta)^{-1} \quad \text{....A.52}$$

this reflection amplitude, is given by

$$| r_{\perp} | = (Z_i^2 + \delta^2)^2 [(Z_i^2 - \delta^2) + 4Z_i^2 \delta^2 \coth^2 \beta]^{-1} \quad ..A.53$$

The transmission in the third medium is given by:

$$T_{\perp} = 1 - (Z^2 + \delta^2)^2 [(Z^2 - \delta^2) + 4Z^2 \delta^2 \coth^2 \beta]^{-1} \quad .....A.54$$

$$Z = 1/n \cos\theta \quad .....A.55$$

For $T_{||}$

$$Z = \cos\theta / n \quad .....A.56$$

$$\delta = (n^2 \sin^2 \theta - 1)^{1/2} \quad .....A.57$$

Appendix B

Transmission averaging program

APPENDIX B

Fortran program used to model the coupling of light between two optical elements via the evanescent field (FTIR).

```
10  DOUBLE PRECISION DELTAP, DELTAL,ZP,ZL,LAMBDA,BETA,A
20  DO 1 I =45,65
30  DO 2 L =10,100,10
40  4 FORMAT(V)
50  X = L*1.0E-9
60  WRITE (6,4)X
70  DN = 1.458
80  DELTAP = FDP(A,DN)
90  WRITE (6,4)DELTAP
100 DELTAL = FDL(A,DN)
110 WRITE (6,4)DELTAL
120 ZP =FZP (A,DN)
130 WRITE (6,4)ZP
140 ZL = FZL(A,DN)
150 WRITE (6,4)ZL
160 LAMBDA = 0.6328*10E-6
170 BETA = FB(X,LAMBDA,DN,A)
180 WRITE (6,4)BETA
190 TP =FT(DELTAP,ZP,BETA)
200 WRITE (6,4)TP
210 TL = FT(DELTAL,ZL,BETA)
220 WRITE (6,4)TL
```

```
230 TA = (TP+TL)/2.0
240 PRINT, "T AVERAGE,  ANGLE,   GAP"
250 3 FORMAT(E11. 5,5X,I3,5X,E11. 5)
260 WRITE (6,3)TA,I,X
270 2 CONTINUE
280 1 CONTINUE
290 STOP

300 END
310 FUNCTION FDP(A,DN)
320 DOUBLE PRECISION FDP,A,DN
330 FDP =-1/SQRT(DN*DN*SIN(A)*SIN(A)-1)
340 RETURN
350 END
360 FUNCTION FDL (A,DN)
370 DOUBLE PRECISION FDL,A,DN
380 FDL = SQRT(DN*DN*SIN(A)*SIN(A)-1)
390 RETURN
400 END
410 FUNCTION FZP (A,DN)
420 DOUBLE PRECISION FZP,A,DN
430 FZP =1/(DN*COS(A))
440 RETURN
450 END
460 FUNCTION FZL (A,DN)
470 DOUBLE PRECISION FZL,A,DN
```

```
480 FZL =COS(A)/DN
490 RETURN
500 END
510 FUNCTION FB(X,LAMBDA,DN,A)
520 DOUBLE PRECISION FB, X,LAMBDA,DN,A
530 FB=(4*3.141592*X/LAMBDA)* SQRT(DN*DN*SIN(A)*SIN(A)-1)
540 RETURN
550 END
560 FUNCTION FT(D,Z,B)
570 A1=(Z*Z+D*D)* (Z*Z+D*D)
580 A2= (Z*Z-D*D)* (Z*Z-D*D)
590 A3=4* Z*Z+D*D/(TANH(B/2)*TANH(B/2)
600 FT=1-ABS(A1/(A2+A3))
610 RETURN
620 END
```

APPENDIX C

Piezoelectric Effect

C1 Introduction

The piezoelectricity of quartz and other materials is due the fact that a pressure which deforms the crystal lattice causes a separation of the centers of gravity of the positive and negative charges thus generating a dipole moment (product of the value of the charges by their separation) in each molecule. The way this separation can cause a coupling to an electric field is shown on fig(C1), which shows a crystal with metal electrodes normal to the direction of the charge separation. If we short circuit these electrodes and apply a stress which causes the centers of gravity of the charges to separate, free negative charges in the wire will be drawn towards the electrode in the direction of positive charge separation, and free positive charges in the wire will be drawn to the electrode in the direction of the negative charge displacement until the crystal appears to be electrically neutral by any test conducted outside the crystal. When the stress is released the charges in the wire will flow back to their normal position. If, during the process we monitor the flow of the charges with an oscilloscope, we will see a pulse of current in one direction when the stress is applied and a pulse in the opposite direction when the stress is released. this is known as the direct piezoelectric effect.

If an alternating voltage is applied to the crystal, an alternating stress is produced in the crystal and the electrical energy is changed to mechanical energy this is known as the converse effect.

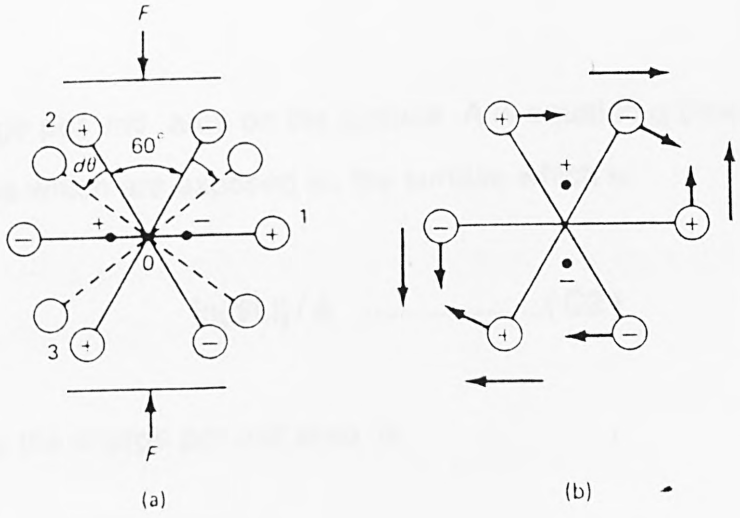

Fig C1 The effect of (a) extensional and (b) shear strains

C.2 The Direct Piezoelectric Effect.

If we consider a rectangular piece of piezoelectric material, with surface area A and thickness L, and it contains n dipoles, each having a dipole moment $\rho = qd$ where q is the change & d is the separation of the charges.

The dipole moment per unit area is given by

$$\rho = nqd/AL \quad \text{.....(C1)}$$

The charge per unit area on the surface A is equal to q times the number of charges which are exposed on the surface which is

$$[n(d/L)] / A \quad \text{.....(C2)}$$

Therefore the charge per unit area is

$$\sigma = nqd/AL \text{.....(C3)}$$

Which is the same as ρ

Within limits the polarization can be considered to be proportional to the strain and can be written

$$P = ex \quad \text{.....(C4)}$$

Where P is the polarization and x is the strain.

C4. The Converse Effect

The piezoelectric crystal placed in an electric field may experience one or more kinds of mechanical strain. The strain can be considered to be proportional to the applied field and we may write

$$x = dE \quad \text{.....(C5)}$$

Where x is the strain and E is the electric field. The constant d is known as the piezoelectric strain co- efficient.

C5 The Generalized piezoelectric Equations

When a field is applied in the x-direction it produces an extensional strain in the x direction. The same electric field might (and often does) produce external strain in the Y and Z directions. Moreover, The same electric field may produce shear strains about one or more of the axes. All possible linear relations between the three components of the electric field and the six components of strains are included in the following set of equations.

$$X_x = d_{11}\ E_x + d_{21}\ E_y + d_{13}\ E_z$$

$$Y_y = d_1\ E_x + d_{22}\ E_y + d_{23}\ E_z$$

$$Z_z = d_{13}\ E_x + d_{23}\ E_y + d_{33}\ E_z \qquad \text{C.6.a}$$

$$Y_z = d_{14}\ E_x + d_{24}\ E_y + d_{34}\ E_z$$

$$Z_x = d_{15}\ E_x + d_{25}\ E_y + d_{35}\ E_z$$

$$X_y = d_{16}\ E_x + d_{26}\ E_y + d_{36}\ E_z$$

Where X_x.....X_y are the extensional and shear strains and E_x, E_y and E_z are the components of the electric field. The d_{ij} are the piezoelectric strain co-efficient. Equation C6 may be written in matrix form.

$$x = dE \quad \text{.....(C6b)}$$

The three components of polarization may be written in terms of the six components of strain in the following way

$$P_x = e_{11}\ X_x + e_{12}\ Y_y + e_{13}\ Z_z + e_{14}\ Y_z + e_{15}\ Z_x + e_{16}\ X_y$$

$$P_y = e_{21}\ X_x + e_{22}\ Y_y + e_{23}\ Z_z + e_{24}\ Y_z + e_{25}\ Z_x + e_{26}\ X_y \qquad \text{(C7a)}$$

$$P_z = e_{31}\ X_x + e_{32}\ Y_y + e_{33}\ Z_z + e_{34}\ Y_z + e_{35}\ Z_x + e_{36}\ X_y$$

And in matrix notation

$$P = ex \quad \text{.....(C.7.b)}$$

Equation C6 & C7 are related to the polarization and the field to strain. It is sometimes necessary to have the equations relating the polarization and field to stress. We have

$$x = dE \quad \text{from equation C.6.b}$$

$$P = ex \quad \text{from equation C17.a}$$

$$-x = SX$$

$$-x = cx$$

Where S is the compliance co-efficient and C is the stiffness co-efficient

Eliminating x before the second and third equations gives

$$-P = eSX \quad \text{.....(C.8)}$$

Eliminating x between first and forth eequations giving

$$-x = cdE \quad \text{.....(C.9)}$$

Equations C.8 & C.9 are the required equations, but we can show that es = d & cd = e, so we can write

$$-P = dx \quad \& \quad -x = eE$$

The proof is a little complex depending on arguments from thermodynamics. We imagine a piezoelectric crystal to be placed in an electric field and at the same time subjected to a mechanical stress. The temperature is held constant. The electric field E produces polarization P and the stress X produce a strain x. Both represent energy stored in the crystal called internal energy U. We now imagine the field to be changed by the infinitesimal amount dx. The change in the internal energy is

$$dU = PdE - xdx \quad \text{.....(C.10)}$$

$$(\partial U / \partial E)_x = P \qquad \text{and} \qquad (\partial U/\partial X)_E = -x$$

$$(\partial^2 U) / (\partial E \partial X) = \partial P/\partial X$$

and

$$(\partial^2 U)/(\partial X \partial E) = -\partial x/\partial E$$

If the process is reversible, i.e. if energy is conserved, this equation C.10 is an exact differential and the order of differentiation is immaterial; therefore

$$\partial P/\partial X = - \partial x/\partial E$$

but from C.8

$$\partial P/\partial X = -es$$

and from C.6.b

$$\partial x/\partial E = d$$

so that we have

$$d = es$$

by writing dU = pdE - Xdx and using the same procedure, one can show that e = cd. We can now write the piezoelectric stress equation as follows

$$\begin{aligned}
-X_x &= e_{11} E_x + e_{21} E_y + e_{31} E_z \\
-Y_y &= e_{12} E_x + e_{22} E_y + e_{32} E_z \\
-Z_z &= e_{13} E_x + e_{23} E_y + e_{33} E_z \\
-Y_z &= e_{14} E_x + e_{24} E_y + e_{34} E_z \qquad \text{(C.11)} \\
-Z_x &= e_{15} E_x + e_{25} E_y + e_{35} E_z \\
-X_y &= e_{16} E_x + e_{26} E_y + e_{36} E_z
\end{aligned}$$

and

$$-P_x = d_{11}\ X_x + d_{12}\ Y_y + d_{13}\ Z_z + d_{14}\ Y_z + d_{15}\ Z_x + d_{16}\ X_y$$

$$-P_y = d_{21}\ X_x + d_{22}\ Y_y + d_{23}\ Z_z + d_{24}\ Y_z + d_{25}\ Z_x + d_{26}\ X_y \qquad \text{(C.12)}$$

$$-P_z = d_{31}\ X_x + d_{32}\ Y_y + d_{33}\ Z_z + d_{34}\ Y_z + d_{35}\ Z_z + d_{36}\ X_y$$

To summarize, we have (in matrix notation)

$$x = dE \quad \text{.....C.13}$$

$$-P = dx \quad \text{.....C.14}$$

$$-x = eE \quad \text{.....C.15}$$

$$P = eX \quad \text{.....C.16}$$

where C.13 is shorthand for

$$\begin{matrix} X_x \\ Y_y \\ Z_z \\ Y_z \\ Z_x \\ X_y \end{matrix} = \begin{matrix} d_{11} & d_{21} & d_{31} \\ d_{12} & d_{22} & d_{32} \\ d_{13} & d_{23} & d_{33} \\ d_{14} & d_{24} & d_{34} \\ d_{15} & d_{25} & d_{35} \\ d_{16} & d_{26} & d_{36} \end{matrix} \begin{matrix} E_x \\ E_y \\ E_z \end{matrix} \qquad \text{(C.13a)}$$

and equation C.14

$$\begin{matrix} & & & & & & & X_x \\ & & & & & & & Y_y \\ P_x & d_{11} & d_{12} & d_{13} & d_{14} & d_{15} & d_{16} & Z_z \\ -P_y = & d_{21} & d_{22} & d_{23} & d_{24} & d_{25} & d_{26} & Y_z \\ P_z & d_{31} & d_{32} & d_{33} & d_{34} & d_{35} & d_{36} & Z_x \\ & & & & & & & X_y \end{matrix} \qquad \text{C.14.a}$$

Note that the rows and columns are interchanged in the d matrices of C.13.a & C.14.a. This is necessary in order to be able to perform the required multiplications. Not being square matrices , neither d nor e matrix can be reciprocal matrix, so it is not possible to "solve" for variables as in the case of this square matrix.

C6 The piezoelectric Matrix for Quartz

Although the piezoelectric matrix contains 18 terms in the general case,

symmetry conditions usually require many of the terms to be zero and establish relations between others. To determine the relationships between the terms in the piezoelectric strain matrix for quartz it is sufficient to perform a rotation of 120° about the two axes followed by a rotation of 180° about the X axis.

The strain matrix is rotated by use of the approximate matrix [C.2] to

obtain

$$x' = \alpha_3 x$$

where α_3 is the 6 x 6 matrix for rotation about the Z axis.

The electric field, being a vector is rotated by the 3 x 3 matrix

$$C = \begin{matrix} C & S & 0 \\ -S & C & 0 \\ 0 & 0 & 1 \end{matrix}$$

where $C = \cos \phi$

$S = \sin \phi$

ϕ= angle of rotation about Z axis

we then have

$$E' = cE \text{ or } E = C^{-1} E'$$

substituting in the piezoelectric strain matrix from equation C.13, we have

$x' = \alpha_3 x = \alpha_3 dE = \alpha_3 dC^{-1} E' = d'E'$ where $d' = \alpha_3 dC^{-1}$

repeating the same process for rotation of 180° about the X axis

$$x'' = \alpha_1 x'$$

$$E'' = aE' \text{ and } E' = a^{-1} E''$$

$$x' = d'E$$

from which

$X'' = \alpha_1 x' = \alpha_1 d'E' = \alpha_1 d'a^{-1} E'' = \alpha_1 \alpha_3 dC^{-1} a^{-1} E''$

or

$x'' = d''E''$ where $d'' = \alpha_1 \alpha_3 dC^{-1} a^{-1}$

Now the double rotation which is compatible with the symmetry of quartz must leave the piezoelectric matrix unchanged. Therefore, each term of d'' must be equal to the corresponding term of the matrix d. This leads to 18 simultaneous equations, the solution of which requires that is of the d_{ij} be zero and that only two of the remaining co- efficient be independent.

In this way the d matrix for quartz is found to be

$$d = \begin{matrix} d_{11} & 0 & 0 \\ -d_{11} & 0 & 0 \\ 0 & 0 & 0 \\ d_{14} & 0 & 0 \\ 0 & -d_{14} & 0 \\ 0 & d_{11} & 0 \end{matrix} \qquad \text{C.17}$$

The d matrix for quartz thus contains five non-zero terms but only two of terms are independent. The five non- zero terms tell us the nature of the

strains which can be produced by the three components of the electric field. The X-component of the electric field produces three types of strain, an extensional strain in the Y direction, and a shear strain about the X axis i.e. in the YZ plane. The Y component of the field produces a shear strain about the Y axis and a shear stress about the Z axis. The latter is and in the Y cut family of piezoids which include the AT & BT cuts. The former is the basis of the strain utilized in the CT - & DT cuts. The 2 components of the field produces no piezoelectric strain.

The e matrix can be calculated from the d matrix by using the equation $e = cd$.

We have

$$\begin{matrix} C_{11} & C_{12} & C_{13} & C_{14} & 0 & 0 \\ C_{12} & C_{11} & C_{13} & -C_{14} & 0 & 0 \\ C_{13} & C_{13} & C_{33} & 0 & 0 & 0 \\ C_{14} & -C_{14} & 0 & C_{44} & 0 & 0 \\ 0 & 0 & 0 & 0 & C_{44} & C_{14} \\ 0 & 0 & 0 & 0 & C_{12} & (C_{11}-C_{12})/2 \end{matrix} \qquad \begin{matrix} d_{11} & 0 & 0 & e_{11} & 0 & 0 \\ -d_{11} & 0 & 0 & -e_{11} & 0 & 0 \\ 0 & 0 & 0 & 0 & 0 & 0 \\ d_{14} & 0 & 0 & e_{14} & 0 & 0 \\ 0 & -d_{11} & 0 & 0 & -e_{14} & 0 \\ 0 & -2d_{11} & 0 & 0 & -e_{11} & 0 \end{matrix}$$

It follows that

$$e_{11} = (C_{11} - C_{12})d_{11} + C_{14}\, d_{14} \text{ and } e_{14} = 2C_{14}d_{11} + C_{44}\, d_{14}$$

Hence if we measure d_{11} & d_{14} and know this elastic constant C_{11} ,

C_{12},C_{14} & C_{44} , we can calculate all the terms of the e matrix.

Characteristics of AT & BT cut resonators depend on the value of e'_{26} which is obtained by rotating the e matrix about the X axis by the angle θ . The value is found to be

$$e'_{26} = (e_{14} SC - e_{11} C)C$$

where C is $\cos\theta$ & S = $\sin\theta$.

The piezoelectric co-efficients of alpha quartz are

$d_{11} = + 2.27 \times 10^{-12}$ m/V $e_{11} = +0.173$ c/m^2

$d_{14} = - 0.67$ $e_{14} = + 0.040$

Appendix D

Circuit diagram of the electronic system of hybrid sensor

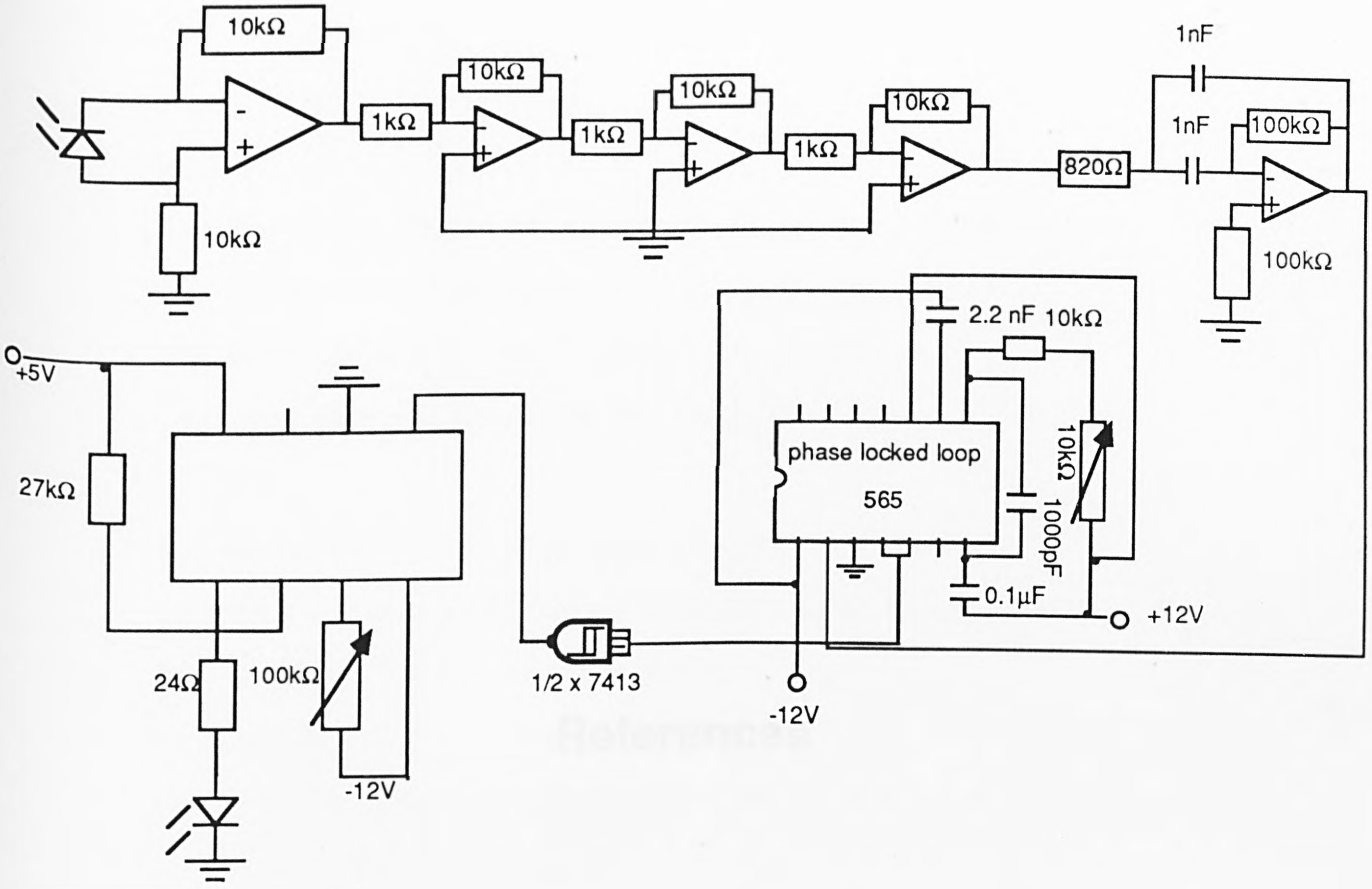
10kΩ
1kΩ
10kΩ
1kΩ
10kΩ
1kΩ
10kΩ
820Ω
1nF
1nF
100kΩ
100kΩ
10kΩ
2.2 nF
10kΩ
phase locked loop
565
10kΩ
1000pF
0.1µF
+12V
+5V
27kΩ
24Ω
100kΩ
-12V
1/2 x 7413
-12V

References

References

[1] Giallorenzi, Thomas G. et al. IEEE. Transactions on microwave Theories and Techniques. MTT-30, 1982. 472 - 511.

[2] Jones, Barry E. J Phys E. Sci Instrum. 18 1985.

[3] Calshaw. Brian The Radio and Electronic Engineer 52 1982 283-290.

[4] Medlock, R.S. Journal of Optical Sensors 1 1986 43-68.

[5] Pitt, G. D. et al. IEEE Review IEE Proc Vol 132 Pt.J, No4. 1985

[6] Rashliegh S.C. Opt Lett 6 1981

[7] Dandridge A. Electron Lett 17 1981.

[8] Berg, Ria. Lefreure, H.C. Shaw, H.J. IEEE J. Lightwave Tech LT-2 1984 91-107

[9] Rogers A.J. Optics and Laser Technology 1977 273 -283

[10] Bucaro J.A., Dardy H.D. Carome E. J. Acoust soc America 62 1977

[11] Jones R.E. Willson J.P. Pitt G.D., Pratt R.H. Foulds K.W.H. Batchelor D.N. Proc 2nd OFS, Stuttgard, 353, (VDE- Verlay Gmbh, Berlin) 1984

[12] Bucaro J.A. Cole J.M. Proc Eascon 1979, IEEE Publi 79 CH 1476-1 AES 572-580

[13] Fields, J.N., Cole , J.H., Appl opt 14 1980 3265-3267

[14] Harmer, A.L. US Patent No 4163397 (1977)

[15] Harmer, A.L. Proc of 3rd Int Conf on optical fibre sensors San Diego 1985 (OSA/IEEE Digest of technical Papers)

[16] Layton, M.R. and Bucaro, J.A. Appl Opt 18 1979

[17] Kingsley S.A. Davies D.E.N. Calshaw B and Howard, Proc. Fibre Opt. Commun. Sept 1978

[18] Lyle J.H. Pitt C.W. Electron Lett. 17 1981

[19] Keck D.B. Fundamentals of Optical Fibre Communications M.K. Barnoski

[20] Yao S.K., Asawa C.K., LipsComb G.F., App1 Opt 21 1982

[21] Lagokos N. Trott W.J. Bucaro A.J. "Micro bending Fibre Optic Sensor Design Optimisation", Proc CLEO 1981.

[22] Asawa C.K. Yao S.K. Stearns R.C., Mota N.L. and Davies J.W. Electron Lett 18 1982

[23] Code R.O., & Hamm C.W., App1 Opt , 18 1979

[24] Fromm. I, Ungerberger H, Proc Int. Opt. Comput. Conf. London England Sept 1978 pp40-42

[25] Nokes M.K., Hill B.C., Barelli A.E., Rev.Sci. Instrum. 49 1978

[26] Delta controls Ltd (U.K.) Type L60 Optical microswitch, Deltrol Works, Island Farm Avenue, East Moseley Surrey.

[27] Spillman Jr, W.B., and McMahon D.H., App1 Opt 21 1982

[28] Kyuma K., Tai S., Nunoshita M, Takroka T, Ida Y., IEEE J. Quantum Electron., QE-18 1982.

[29] Gottlieb. M and Brandt B.B., App1 Opt 20 1981

[30] Grattan, K.T.V. and Palmer, A.W. SPIE Proceedings 492 535-42, 1985.

[31] Tanaka T, Benedek G.B., App1 Opt 14 1975

[32] Sheem S.K., Cole J.H.., Opt Lett 4 1979

[33] Beasley J.D., J. Acoust. Soc. Amer 68 1980

[34] Beasley J.D., "Evanescent fibre optic pressure sensor apparatus",

U.S. patent 4 360 247, Nov 1982.

[35] Carome E.F., Koo K.P., Opt Lett 5 1980

[36] Spillman W.B., McMahon D.H., App1 Opt 19 1980, P 113-117

[37] Phillips R.L., Opt Lett 5 1980 P 318-320

[38] B.I.C.C. private communication

[39] Kirst R, Sohler W, Fibre Optic Spectrum Analyser; J. Lightwave. Tech LT1 (1983) 105-110

[40] Green E.I., Holmberg E., Gremillion F.C., and Allard F.C. ; Proc 3rd Int. Conf. on Optical Fibre Sensors 13-14 Feb 1985 San Diego (OSA/IEEE Digest of Technical Papers)

[41] Pratt R.H., Jones R.E., Extance P ., Pitt G.D., and Foulds K.W.H. Proc of 2nd Int. Conf. on Optical Fibre Sensors 5-7 Sept 1984 Stuttgart (Vde Verlay Gmbh, 1984)

[42] Hamer A.L. Symp. On Optical Sensors and Optical Techniques in instrumrntation 12 Nov 1981, London list of Measurement & Control

[43] Shi-Kay Yao and Asawa C.K. Ieee Journal on Slected Areas in Communication Vol SAC1 No3 1983.

[44] Hull J.R., "Proposed frustrated-total-internal-reflection acoustic sensing method," Appl. Opt., vol. 20 1981

[45] BICC Fibres, England, Private communication.

[46] Morley A., "Strength of Materials" London, U.K. Longmans 1955

[47] Zienkievig O.C., "The Finte Element Method" London, U.K. McGraw-Hill 1977

[48] Jones B.E., Optical Sensors and Optical Techniques in Instrumentation Int. Measurement Control Symp. London, England. Nov 1981

[49] Paros J.M., Parascientific Inc. Proc. Air Data Symp., Naval Air

Systems Command, June 1976

[50] Kirman P.G., Transducers Tempcon Conf., London, England. 1983

[51] Serra N.R., "Technical report on the quartz resonator digital accelerometer" AGARD Conf. Proc. (Oxford, England) 1967

[52] McGlade S.M., Jones G.R., " AN Optically Powered Vibrating Quartz Force Sensor" G.E.C. J. Res., Vol 2 1984.

[53] Mallalieu K., Youngquist R., Davies D.E.N., Jones G.R., " An Analysis of the Photothermal Drive of a Quartz Force Sensor" Proc. Fibre Optics 85, 1985. SPIE vol 522.

[54] Jones B.E., Philp G.S., "A Vibrating Wire Sensor with Optical Fibre Links for Force Measurement", Proc. Conf. Sensors and their Applications. London, England Inst. Phys. 1983.

[55] Dieulesaint E., Royer D., Rakouth H., "Optical Excitation of Quartz Resonators" Electron. Letts. vol 18 1982

[56] Pinnock R., (Marconi Research Centre), Chelmsford, Private Communication.

[57] Grattan K.T.V., Palmer A.W., Samman N.D., Abdullah F., "A Mathematical Analysis of Optically Powered Quartz Resonant Structures in Sensor Applications" J. Lightwave tech. 1988 (to be published).

[58] Hecht E., Zajac A., "Optics" Addison-Wesley, London, U.K. 1979.

[59] Brekhovskikh L.M., "Waves in Layered Media" New York Academic Press 1960.

[60] Bottom V.E. "Introduction to Quartz Crystal Unit Design" Van Nostrand London 1982.

[61] Cady W.G " Piezoelectricity" McGraw Hill (1946)

This article has been removed for copyright reasons